NTNU

Norwegian University of
Science and Technology

Density functional theory investigations of octahedral connectivity in [001] and [111] directional perovskite superlattices

Eirin Mærk Wehn

Nanotechnology
Submission date: February 2018
Supervisor: Thomas Tybell, IES
Co-supervisor: Magnus Moreau, IES

Norwegian University of Science and Technology
Department of Electronic Systems

Problem description

This master thesis deals with density functional theory (DFT) studies to investigate the possibility to rely on oxygen octahedral connectivity across interfaces in superlattices to control the octahedral rotations in adjacent layers. As a model system, superlattices of antiferromagnetic $LaFeO_3$ and non-magnetic $SrTiO_3$ are to be used. In particular, it will be investigated how crystalline orientation and film layer thickness affect octahedral connectivity. Moreover, the possibility to rely on high symmetry phonon calculations of superlattices to investigate coupling shall be investigated.

Preface

This master thesis was written as the final part of my Master of Science in nanotechnology and nanoelectronics at the Norwegian University of Science and Technology (NTNU). The work has been performed at the Department of Electronic Systems at the Faculty of Information Technology and Electrical Engineering, during the autumn semester of 2017, extending to February 2018.

I would like to thank my supervisor Prof. Thomas Tybell and co-supervisor Magnus Moreau for their valuable guidance and feedback throughout the whole master work. I would also like to thank my family for the support throughout my studies.

Abstract

To be able to exploit the magnetic properties of antiferromagnetic transition metal oxide perovskites in spintronic devices, as magnetic random access memory (MRAM) devices, a better understanding of how these magnetic properties may be controlled is crucial. Due to the strong coupling between structure and magnetic properties in such materials, a promising route to control and tune these properties is by means of structural control. An important structural parameter in perovskites is the BO_6 octahedron, and structural distortions corresponding to distortions of these octahedra have been the main focus in this master thesis.

The octahedral distortions in superlattices of antiferromagnetic $LaFeO_3$ (LFO) and non-magnetic $SrTiO_3$ (STO) has been investigated using density functional theory (DFT). Superlattices with various film layer thicknesses – ranging from one octahedral unit to six octahedral units – and orientation – where both [001] and [111] oriented superlattices have been investigated, – were tested to look at how these factors affected the octahedral distortions in the superlattices. This was done by performing two different calculation methods – phonon mode calculations and structural calculations. In this way, it was also investigation whether the phonon mode calculation method actually could be used to investigate how different factors influenced the structure of the superlattices, or whether the conventional structure calculation method should be used to investigate such effects.

The results indicated that the octahedral distortions – corresponding to octahedral rotations, – in the superlattices were affected by both the film layer thicknesses and the superlattice orientation. The film layer thicknesses were found to mainly affect the rotation magnitudes in the different film layers, while the orientation could affect the overall tilt pattern in the film layers. The results were generally consistent for the two different kinds of calculation methods, indicating that phonon mode calculations can be used to investigate how structures in superlattices are affected by different factors. Hence, it was found that octahedral control in superlattices of LFO and STO can be obtained. This control might make it possible to tune the magnetic properties of LFO film layers in such superlattices.

Sammendrag

For å kunne utnytte de magnetiske egenskapene til antiferromagnetiske overgangsmetalloksidperovskitter i spintroniske enheter, som for eksempel enheter med magnetisk "random access memory" (MRAM), er det viktig å få en bedre forståelse for hvordan disse magnetiske egenskapene kan styres. På grunn av den sterke koblingen mellom struktur og magnetiske egenskaper i slike materialer er strukturell kontroll en lovende vei å gå for å kontrollere og finjustere disse egenskapene. En viktig strukturell parameter i perovskitter er BO_6-oktaederet, og strukturelle forvregninger tilsvarende forvrengninger av disse oktaederne har vært hovedfokus i denne masteroppgaven.

Forvregninger i oktaedre i supergittere med anitiferromagnetiske $LaFeO_3$ (LFO) og ikke-magnetiske $SrTiO_3$ (STO) har blitt undersøkt ved bruk av tetthetsfunksjonalteori (*eng.* density functional theory (DFT)). Supergittere med forskjellige filmlagtykkelser – fra tykkelser på én oktaederenhet til seks oktaederenheter – og orientering – hvor både [001]- og [111]-orienterte supergittere ble undersøkt, – ble testet for å se på hvordan disse faktorene påvirket forvregningene i oktaederne i supergitterene. Dette ble gjennomført ved å utføre to forskjellige beregningsmetoder – fononmodeberegninger og strukturberegninger. På denne måten ble det også undersøkt om fononmodeberegningsmetoden faktisk kunne brukes til å undersøke hvordan ulike faktorer påvirket strukturen til supergitterne, eller om den konvensjonelle strukturberegningsmetoden burde brukes til å undersøke slike effekter.

Resultatene indikerte at forvregningene av okteaderne – som svarte til oktaederrotasjoner – i supergitterne ble påvirket av både filmlagtykkelse og orineteringen av supergitterne. Filmlagtykkelsen så ut til å hovedsaklig påvirke rotasjonsmengde, mens orientasjonen kunne påvirke det totale vippemønsteret i filmlagene. Resultatene fra de to foskjellige beregningsmetodene var generelt konsistente, noe som indikerer at fononmodeberegninger kan brukes for å undersøke hvordan strukturer i supergittere påvirkes av forskjellige faktorer. Det ble dermed funnet at kontroll av oktaederne i supergittere med LFO og STO kan oppnås. Denne kontrollen kan gjøre det mulig å finjustere de magnetiske egenskapene til filmlagene med LFO i slike supergitter.

Contents

Chapter 1

Introduction

The development in the electronics industry has gone incredibly fast, from the first integrated circuit – containing only a few transistors – developed in 1958 by Jack S. Kilby [1] to the chips produced by Intel today, containing billions of transistors. The number of transistors per unit area in such chips doubled approximately every second year, following Moore's law, from around 1970 until a few years back, by continuously decreasing the transistor size. There is a physical limit, however, of how small such transistors can be, and another limit of how small the transistors can be before the production of them stops to be cost effective. To continue the development in this industry one therefore has to look at alternative routs to the downsizing of transistors. In some areas in the electronics industry a route to further development can be to gradually replace electronics by spintronics.

One example where such a replacement may take place is in memory devices for data storage. In conventional memory devices the memory is charge-based and the state of each memory cell (0 or 1) – called a bit – is determined by the charge stored in the cell. In magnetic random access memory (MRAM) this "charge logic" is replaced by "spin logic", where the orientation of magnetic moments in a ferromagnet decides if the bit is a 0 or a 1 [2]. There are several advantages of using magnetism insead of charge in data storage. For example will a spin-based memory device be robust against charge perturbations which can cause data loss in charge-based devices. In addition, MRAM also has some other potentially great advantages, as infinite endurance and faster random access than what is possible in conventional RAM [2].

A disadvantage of using ferromagnetism to store data, however, is the vulnerability to magnetic perturbations. Just as ionizing radiation can cause data loss in charge-based memory devices, external magnetic perturbations can reorient the magnetic moments in MRAM, and hence cause data loss. Another kind of magnetic materials – antiferromagnetic materials – possess no net magnetization and are therefore robust to such external magnetic perturbations, as well as ionizing radiation. In antiferromagnets the magnetic moments alternate antiparallel to each other along a specific direction. The logical 0s and 1s can thereby be

represented by alternating magnetic moments along different directions.

The zero net magnetization also make data stored on MRAM, based on antiferromagnetism, invisible to external magnetic probes [3]. All in all the zero magnetization makes it difficult to both read and write the data – both intentionally and unintentionally. To use antiferromagnetism to store data it is therefore crucial to find a way in which to control the antiferromagnetism for reading and writing data.

A better understanding of how antiferromagnetism can be controlled is therefore crucial if such materials are to be used in spintronic devices. In antiferromagnetic materials where the magnetic properties are strongly coupled to the structure, structural control can be a promising way to be able to tune the magnetism in a controlled way. A group of materials which exhibit such strong couplings is magnetic transition metal oxide perovskites, where several possess an easy magnetization axis – a Néel vector – lying along a specific crystallographic axis. This easy axis have been showed to change for several systems where a change in structure also has appeared [4, 5, 6, 7, 8]. This implies that the direction of the Néel vector can be controlled with structural control.

In addition to control of magnetic moments, structural control in interface layers between perovskites and in perovskite superlattices have induced several novel properties, one example being improper ferroelectricity [9].

Perovskites possess a structural parameter which have been showed to be significant for the material properties. This structural parameter is the BO_6 octahedra. In a perovskite material these octahedra are connected, and can rotate in different ways. This opens the very interesting question if these octahedral rotations can be used to control antiferromagnetism in antiferromagnetic perovskites. To be able to do this, however, one has to understand how these octahedral rotations can be controlled.

The aim of this master thesis is to shed light on this control of antiferromagnetism via octahedral rotations. This is done by the use of density functional theory calculations by looking at how octahedral rotations couple across perovskite/perovskite interfaces in superlattices with different film layer thicknesses.

To study this, superlattices of $LaFeO_3$ (LFO) and $SrTiO_3$ (STO) – LFO_m/STO_n – are used as a model system. LFO is a G type antiferromagnetic insulator with a high Néel temperature of 738 K [10], it has an orthorhombic structure [11], and a Néel vector along the orthorhombic **a** axis. STO is s non-magnetic insulator but undergo a structural phase transition at a temperature of about 105 K, where it is tetragonal at temperatures lower than 105 K and cubic at temperatures higher than 105 K.

The octahedral coupling is studied in LFO_m/STO_n superlattices with different film layer thicknesses, n and m, to look at how the film layer thickness and the ratio of the film layer thicknesses affect the octahedral coupling. Another parameter studied is the orientation of the superlattices, in which both superlattices with out-of-plane direction [001] and [111] is studied. This is investigated by looking

at the phonon modes in highly symmetric superlattices and compare these results with results from conventional structure calculations. Hence, it is also investigated whether the phonon mode method is applicable in calculations of such structures to find how the different film layers affect each other.

In this master thesis a taste of what is found regarding control of the octahedral rotations within this research field will be given in chapter 2. Chapter 3 includes a description on how DFT calculations are performed and what factors that are important for a DFT calculation to run smoothly. A description of the DFT calculations run in this thesis will be given in chapter 4 followed by the results and a discussion of these results in chapter 5. In the final chapter, chapter 6, a conclusion of these results will be drawn.

Chapter 2

Control of octahedral rotations

This chapter first describes the perovskite structure and its properties (section 2.1). In section 2.2 some common octahedral distortions in oxide perovskites are covered. Then the chapter continues with looking at how these distortions – focusing mainly at octahedral rotations and tilts – are affected by different control parameters, such as stain (section 2.3.1) and interfacial couplings (section 2.4) in single layer films, and periodicity in coherent superlattices (section 2.5). The chapter ends with a summary of these different effects (section 2.6). Even though this thesis distinguishes between different types of octahedral distortions, several of these distortions are generally present simultaneously in perovskites, as will be apparent by the examples given in this chapter. Several examples concerning perovskite compounds with space group symmetry $Pnma/Pbnm$ will be given. $Pnma$ and $Pbnm$ have the same symmetry but differs in how the axis are defined ("**abc**" for $Pnma$ and "**cab**" for $Pbnm$). Whether the space group is oriented as $Pnma$ or $Pbnm$ will therefore be stated for the examples where this orientation is important.

2.1 The transition metal oxide perovskite structure

Perovskites is a family of compounds with the general formula ABX_3, where (normally) A is a large cation, B a medium-sized cation, and X is an anion [12, Ch. 1]. The general perovskite structure is shown in figure 2.1a. The B cations form BX_6 octahedra with their six nearest neighbour X anions (figure 2.1b), while the A cation is coordinated to twelve X anions which forms a cuboctahedral cage (figure 2.1c) in the vacancies of the BX_6 octahedra.

In transition metal oxide (TMO) perovskites the X anion is O^{2-} and the B cation in the center of the BO_6 octahedra is a transition metal. The A cation in the cuboctahedral cage normally form fixed valence, closed-shell electron configurations [13], and therefore normally only contribute to the structural properties

of these materials.

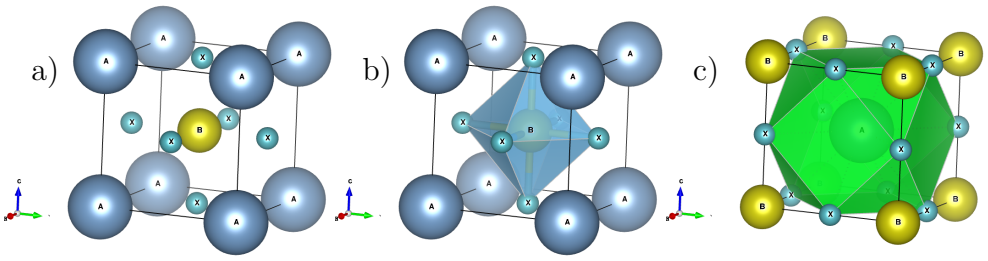

Figure 2.1: The perovskite structure. a) shows the general perovskite structure, b) shows the BX_6 octahedra, and c) shows the cuboctahedral A-cation site. The unit cell in c) is shifted by (½,½,½) relative to the unit cells in a) and b). Figures made in VESTA [14].

The ideal perovskite structure is cubic and corresponds to the space group $Pm\bar{3}m$ [12, 15]. Most perovskites do not have this ideal structure, however, but possess different structural distortions, corresponding to space groups with lower symmetry than the ideal structure. For example, the perovskite structure makes it possible for the BO_6 octahedron to rotate about three different axes, corresponding to the x-, y-, and z-axis in figure 2.2. The magnitude of the rotation can be different about different axes, and are given by α, β, and γ for rotations about the x-, y-, and z-axis, respectively.

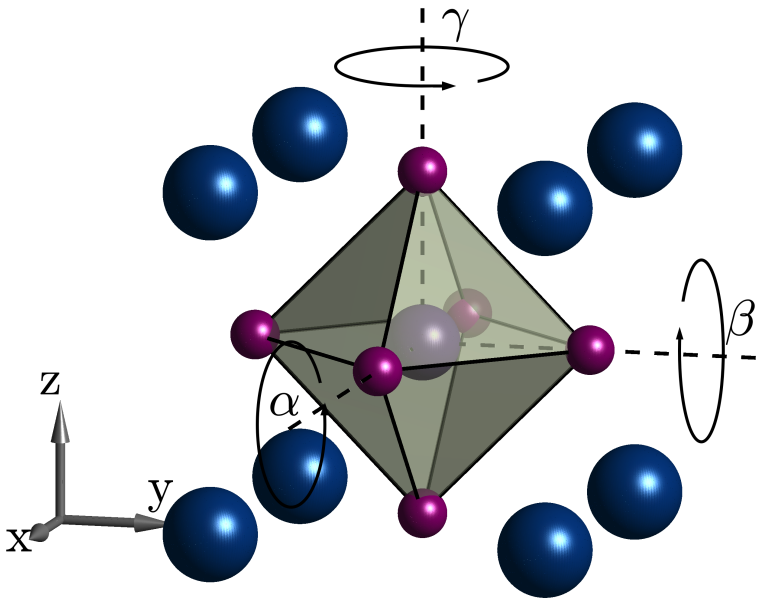

Figure 2.2: The BO_6 octahedra can rotate about three different axes. The rotation magnitudes are given by α, β, and γ.

2.2 The corner-connected octahedral network in perovskite oxides

In the perovskite structure each oxygen anion is shared by two neighbouring BO_6 octahedra, resulting in a corner connected octahedral network (2.3a). This octahedral network is flexible, and can deform in different ways. Figure 2.3b shows three examples of different types of octahedral distortions in this network, one where the different octahedra in the network have different sizes – that is, the B-O bond length of one octahedra is different from that of another octahedra, – and one where the shape differs from the ideal shape caused by e.g. an extension of the B-O bond length along one axis and a decrease in B-O bond length along the two other axes. The third example in figure 2.3b is not caused by a change in B-O bond length but rather a change in the *connectivity* [13]. The connectivity describes how the octahedra rotate and tilt relative to the ideal structure, and is the most common distortion of the octahedral network [15]. Because the octahedra are connected by shared oxygen anions, a distortion of rigid octahedron also affect the distortion of its neighbouring octahedra. While rotation distortions are defined as described in the previous section and illustrated in figure 2.2, the tilt angels are defined as the B-O-B bond angles between adjacent octahedra. The magnitude of the B-O-B bond angles are given by θ_x, θ_y, and θ_z, where the B and O ions lies along the x-, y-, and z-axis, respectively, illustrated by θ_z in figure 2.3c.

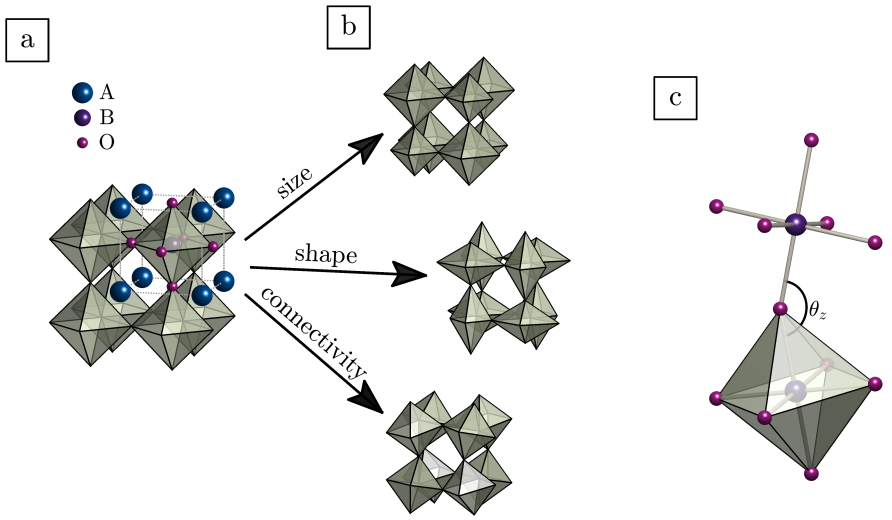

Figure 2.3: Octahedral distortions of the corner-connected octahedral network in perovskites. a) shows an undistorted octahedral network of eight octahedra. One unitcell with the A, B, and O ions is illustrated for one octahedron in the network. b) shows three types of octahedral distortions of his network, distortions by different sizes, shapes, and connectivity. c) shows the B-O-B bond angle (tilt) along the z-axis, θ_z.

The octahedral network can rotate in different ways along different directions to form different tilt patterns. These tilt patterns are described by the use of Glazer notation [16, 17], $a^{\#}b^{\#}c^{\#}$, where a, b, and c indicate the rotation magnitude about each pseudocubic axis (same letter means same rotation magnitude). The "#" states if the octahedra about the respective axis rotate out-of-phase ("-"), in-phase ("+"), or do not rotate ("0"). The most common tilt pattern in perovskite oxides whit only one type of A cation (i.e. not $A_{1-x}A'_xBO_3$ perovskites) is the $a^-a^-c^+$ tilt pattern with orthorhombic $Pnma$ symmetry [18]. The second most common tilt pattern in such perovskites is the $a^-a^-a^-$ tilt pattern with rhombohedral $R\bar{3}c$ symmetry [13, 18].

An example in which the first octahedral distortion shown in figure 2.3b occur is in rare-earth nickelates ($R\mathrm{NiO_3}$), particularly those with small rare-earth cations (i.e. Y and Lu) [19]. The second type of deformation by a change in B-O bond length – changes in shape – is typically caused by first-order Jahn-Teller distortions [13, 15]. Such a distortion happens when a an electronic degeneracy disappears with this structural distortion.

Another kind of distortions found in some perovskites is distortions of the B cations relative to the oxygen anions, called ferroelectric distortions [15]. Two examples of TMO perovskites where such distortions occur are $\mathrm{BaTiO_3}$ and $\mathrm{PbTiO_3}$ [20].

What kind of distortion(s) from the ideal structure most favorable for a specific perovskite compound depend on a variety of factors, both external (e.g. temperature and pressure) and internal (e.g. composition) [12, Ch. 1]. For example, a factor well studied is the Goldschmidt tolerance factor which gives the mismatch between the A and B cation sizes and is given by

$$t = \frac{r_A + r_X}{\sqrt{2}(r_B + r_X)}, \tag{2.1}$$

where r_A, r_B, and r_X are the radii of the A cation, B cation, and X anion, respectively [12, Ch. 1]. The cubic structure is probable for a perovskite structure if $t = 1$. If $t < 1$, however, a lowering of the cubic symmetry by means of octahedral rotations usually occurs [21], and if $t > 1$ ferroic properties may arise as the B cation moves away from the center of the BO_6 octahedra, resulting in a decrease in some of the B-O bond lengths. Other crystal structures are preferred when t differs to much from unity.

2.2.1 How octahedra rotations relate to material properties

As an overview of different possible distortions in the octahedral network now is established, this section will cover how the most common distortions (rotations and tilts) relate to material properties.

The electronic properties of these materials are strongly determined by the electron interactions [22], and in TMOs these interactions mainly occur between the transition metal d electrons and oxygen $2p$ electrons. TMOs are particularly interesting due to the competing energy scales corresponding to different kinds of interactions (e.g. Coulomb repulsion, orbital bandwidths and Hund's exchange) – while one of these energy scales typically dominates in "conventional" materials (e.g. metals and semiconductors) [15]. This competition between different energy scales cause strong couplings between lattice, electrons, and spin. Because of these competing energy scales many transition metal oxide perovskites can switch to other phases when exposed to small external perturbations favouring these low energy phases.

Because of the strong couplings, a small change in lattice structure can lead to a distinct change in material properties, and different kinds of changes in the lattice structure (e.g. B-O-B bond angle or B-O bond length) can affect different material properties. For example if the B-O-B bond angles are changed this will affect the magnetic superexchange interactions in antiferromagnetic perovskites – affecting the magnetic properties – whilst a change in B-O bond length will affect the crystal field splitting.

Erat *et al.* have looked at how B-O-B bond angles affect the electric conductivity in the complex perovskite $La_{1-x}Sr_xFe_{0.75}Ni_{0.25}O_{3-\delta}$ (LSFNO) compound with $x = 0.0, 0.25, 0.5, 0.75, 1.0$ [23]. The electric conductivity in perovskites depend on charge transfer and the double exchange interactions, both dependent on the overlapping of B d and oxygen $2p$ orbitals – that is, the B-O-B bond angle and B-O bond length. In addition double exchange interactions depend on several other parameters, as for example oxygen vacancies and distribution of different-valence B cations.

The charge transfer increases as the overlap between the B d and oxygen $2p$ orbitals increases. From figure 2.4 one can see that the Fe/Ni-O bond length decreased with increasing Sr content. In addition the B-O-B bond angle increased with increasing Sr content (figure 2.5). Both decreased B-O bond length and increased B-O-B bond angle result in an increase of overlapping between these orbitals (where 180° results in most overlapping). This implied that the charge transfer in LSFNO increased with increasing x.

In figure 2.5 one can see that (despite the increase in charge transfer) the electric conductivity decreased when x went from 0.5 to 0.75. Erat *et al.* concluded from this result that the decrease in double exchange was higher than the increase in charge transfer between these samples. To understand this decrease in double exchange one also has to look at the distribution of different-valence B cations and the concentration of oxygen vacancies, and how these factors changes for different Sr contents.

As x became larger, more La^{3+} cations were replaced by Sr^{2+} cations, resulting in an increase in the number of electron holes and thereby more oxidation of the Fe cations, from Fe^{3+} to Fe^{4+}. When $x = 0.5$ the concentration of Fe^{3+} was equal

to Fe^{4+}, and hence this sample showed the highest electrical conductivity.

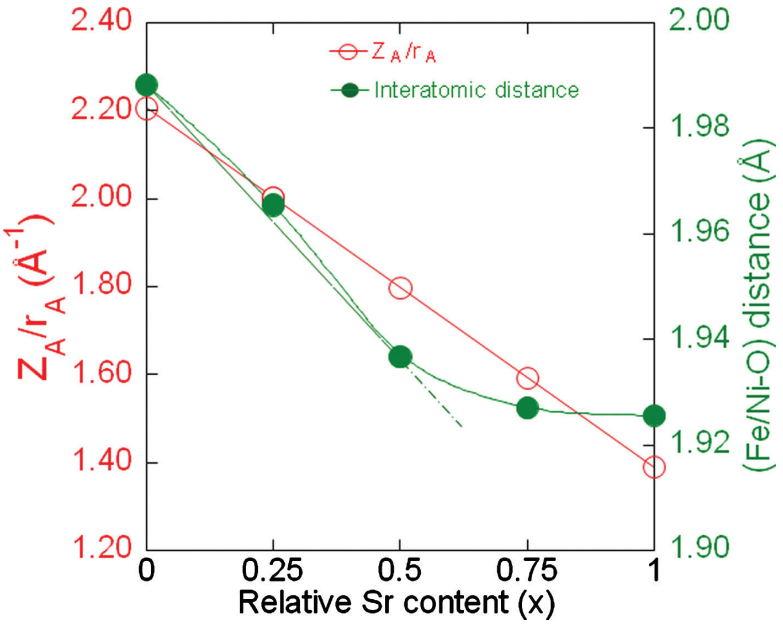

Figure 2.4: A-site Coulomb potential and Fe/Ni–O bond length of $La_{1-x}Sr_xFe_{0.75}Ni_{0.25}O_{3-\delta}$. Z_A and r_A are the charge and the weighted average of valences and ionic radius of the A cations, respectively. Figure from [23].

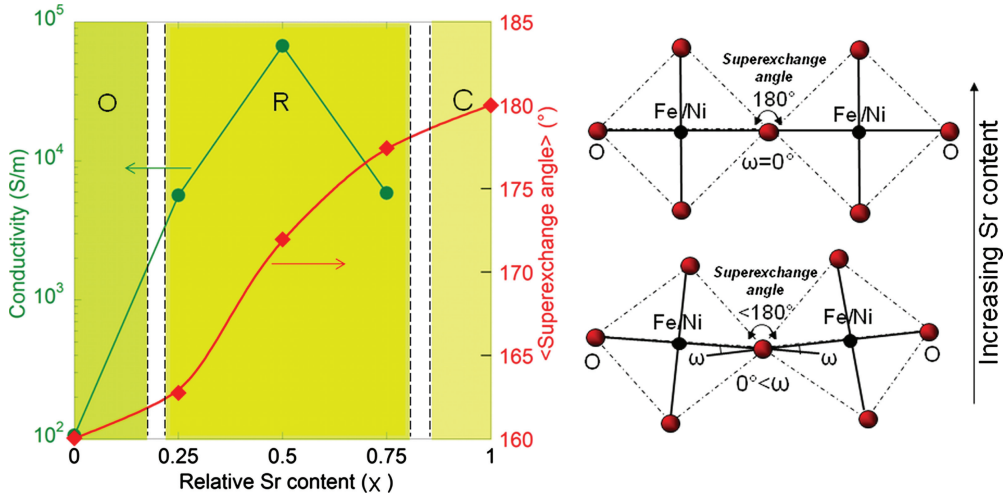

Figure 2.5: Electrical conductivity at 300 K and superexchange angle (B-O-B bond) angle depending on Sr content (x) (left) and a schematic illustrating the average B-O-B bond angle and how it changes with increasing Sr content (right). O, R, and C in the left figure denote orthorhombic, rhombohedral, and cubic phases, respectively. Figure from [23].

The oxygen vacancy concentration, δ, increased with increasing x. Increased oxygen vacancy concentration is unfavorable for the electrical conductivity because of the resulting disruption in the B-O-B hopping (double exchange) and also because of charge transfer contributions.

When $x = 0.75$ the sample allowed a distribution of 5% Fe^{3+} ions and 95% Fe^{4+} ions. This, together with the increased oxygen vacancy concentration, made fewer electrons able to hop between the Fe^{3+}-O^{2-}-Fe^{4+} ions – that is, a decrease in double exchange interaction. The overall electric conductivity went down, which means that the decrease in double exchange was higher than the increase in charge transfer.

Erat *et al.* also compared LSFNO, with $x = 0$ (LFNO), with LFO, to get an insight in how B-O bond length affect physical properties [23]. These two compounds have similar crystallographic orthorhombic symmetry and electronic configuration, but the substitution of Fe by Ni resulted in shorter B-O bond lengths and thus increased overlapping of the B $3d$ and O $2p$ orbitals. This made LFNO a semiconductor while LFO is an insulator at 300 K.

2.3 Controlling the octahedra rotations in perovskites

Because of the effect different structural distortions – like octahedral rotations – have on the material properties of perovskite oxide thin films, it is favorable to find a way to control these rotations, so that they can be tuned in different, controlled ways. In ref. [13] Rondinelli *et al.* investigate three different chemistry-independent ways in which to achieve this, where the octahedral control parameters are epitaxial strain, interfacial couplings at perovskite/perovskite heterointerfaces (section 2.4), and perovskite/perovskite ratio in coherent superlattice formation (section 2.5).

2.3.1 Epitaxial strain

By coherently growing a perovskite oxide thin film on a substrate which have different in-plane lattice parameters than that of the bulk film material, the film material will be strained due to the constraint that the film and substrate must have the same in-plane lattice parameters [15]. The bi-axial strain imposed on the film is given by

$$\epsilon = \frac{(a - a_0)}{a_0}, \tag{2.2}$$

where a is the in-plane lattice parameter of the substrate material imposed on the film, and a_0 is the bulk lattice parameter of the film material.

The thin film material is likely to compensate this different in-plane lattice parameter by changing the tilt pattern or the magnitude of the rotations and

tilts of its octahedral network. In this way different strains can lead to different rotations and tilts in the film, and thereby different film properties, not found in the bulk material. This strain-octahedral rotation coupling mechanism was found theoretically by the use of density functional theory (DFT) (see chapter 3) in bi-axially strained $SrRuO_3$ – with $a^-a^-c^+$ tilt pattern and $Pbnm$ symmetry – by Zayak *et al.* [24].

They found that the rotations about the out-of-plane direction in a [001] oriented ferromagnetic (FM) film decreased with increasing stain, where the maximum compressive and tensile strain were set to about -4% and 4%, respectively. The tilting showed the opposite behaviour – increasing in magnitude when going from a high compressive (negative) strain to a high tensile (positive) strain. Note that in this article "rotations" was defined as rotations about the pseudocubic z-axis, γ, while "tilting" was defined as $(180° - \theta_z)/2$, and is thereby related to the magnitudes of the rotations about the in-plane pseudocubic axes (the α and β rotations). Hence, using the terminology of this thesis, γ (α and β) decreased (increased) with increasing tensile strain. In addition to changes in magnitude of the rotation angles, changes in shape was observed.

The calculations where preformed for both a ferromagnetic and a non-magnetic (NM) system. The NM system showed similar strain-octahedral rotation coupling as the FM system for compressive strains ($\epsilon < 0$). For tensile strains ($\epsilon > 0$), however, the NM phase compensated the increase in stain by a bigger decrease in the Ru-O bond length in the out-of-plane direction, resulting in an octahedral shape distortion [25]. Because of this compensation the γ (α and β) rotation angles did not decrease (increase) further with increased tensile strain.

The same behaviour regarding how the rotation angles in-plane (α and β) and out-of-plane (γ) changes with increasing strain is found for $LaNiO_3$ with both experiments and theoretical calculations [26]. $LaNiO_3$ has an $a^-a^-a^-$ tilt pattern and $R\bar{3}c$ symmetry. In reference [26] the α and β rotation angles were affected by an equal amount by the bi-axial strain, while γ had larger values than α and β for compressive strain and lower values for tensile strain, resulting in an $a^-a^-c^-$ tilt pattern.

As seen in the two examples above the bi-axial strain can affect the tilt pattern differently along different crystallographic directions. This is somewhat more apparent in $LaAlO_3$ where compressive and tensile bi-axial strain were theoretically found to induce different tilt patterns in the material by the use of density functional theory [27]. As $LaNiO_3$, $LaAlO_3$ also has an $a^-a^-a^-$ tilt pattern and $R\bar{3}c$ symmetry in the bulk unstrained state. Further, bi-axially strained $LaAlO_3$ were found to have the same tilt pattern as strained $LaNiO_3$ – that is $a^-a^-c^-$ – for small strains (from about -0.2%-0.1%). For higher compressive strains ($\epsilon < -0.002$) an $a^0a^0c^-$ tilt pattern was obtained while an $a^-a^-c^0$ tilt pattern was obtained for higher tensile strains ($\epsilon > 0.001$).

It is also worth mentioning another effect of compressive strain common in perovskite dielectrics. In reference [28] ferroelectric $BaTiO_3$ were grown on $GdScO_3$

and $DyScO_3$ to investigate how compressive strain could affect the ferroelectric properties of $BaTiO_3$. Thin films of $BaTiO_3$ grown on $GdScO_3$ and $DyScO_3$ encounter a bi-axial strain of about -1.0% and -1.7%, respectively. It was found that both the paraelectric-to-ferroelectric transition temperature (T_c) and the polarization increased with increased compressive strain for $BaTiO_3$.

Different rotational orderings in the film material

As mentioned in section 2.2 perovskite oxides usually do not have the ideal perovskite cubic $Pm\bar{3}m$ symmetry with an $a^0a^0a^0$ tilt pattern, while an orthorhombic $Pnma$ symmetry with an $a^-a^-c^+$ tilt pattern is quite common. When octahedral rotations are different ("-", "+", or "0") about different pseudocubic rotation axes, like for this tilt pattern, the 'ùnique" rotation phase – the in-phase rotation for this example – can either lay about an in-plane axis, or the out-of-plane axis. The first case would lead to an $a^+b^-b^-$ or $a^-b^+a^-$ tilt pattern in the film material, while the latter case would result in an $a^-a^-c^+$ tilt pattern in the film (see figure 2.6). How these rotation phases are ordered can have an impact on how the strain affect the displacements in the octahedral network in the film.

In reference [24] Zayak *et al.* investigated how the rotations in $SrRuO_3$ with space group $Pbnm$ ($a^-a^-c^+$ tilt pattern and the c-axis as the long axis) was affected for both the $[001]_o$ orientation (discussed above) and the $[110]_o$ orientation ("o" indicating an orthorhombic unit cell as reference cell). For the latter orientation they found that the rotation and tilt angles – that is out-of-plane and in-plane rotations, respectively – both decreased when going from a compressive to tensile strain, and that they are both fixed by the substrate constraint.

Also one rotational ordering can be energetically more favorable than another for different kinds of strains as shown in reference [29] for $CaTiO_3$ (space group $Pbnm$). By density functional theory it was found that the $[110]_o$ orientation (in-phase rotations about the out-of-plane direction) was energetically favorable over the $[001]_o$ orientation for compressive strains. For tensile strains more than about 1.5% the $[001]_o$ orientation was found to be the most favorable orientation.

In such perovskite thin films with symmetry-inequivalent pseudocubic (001) planes one can have structural domain formation if the energies corresponding to the different orientations are similar. This means that in parts of the thin film one will obtain the $[001]_o$ orientation for example, while in other parts the film will have the $[110]_o$ orientation, corresponding to different rotational orderings. In reference [30] it was found that $LaFeO_3$ (with space group $Pbnm$) thin films grown on a [001] oriented $SrTiO_3$ substrate (about 0.68% lattice mismatch) had no growth in the $[001]_o$ direction. An approximately 50-50% domain distribution was found, however, where the entire film had grown in the $[110]_o$ direction but 50% of the film had the $[001]_o$ direction (long c-axis) parallel to the [100] direction of the substrate, while for the remaining 50% the $[001]_o$ direction was parallel to the [010] direction of the substrate. When $LaFeO_3$ was grown on a MgO substrate

(about 7% lattice mismatch) the $[001]_o$ orientation of the film was also present. In these films there was about one third of each of these three orientations.

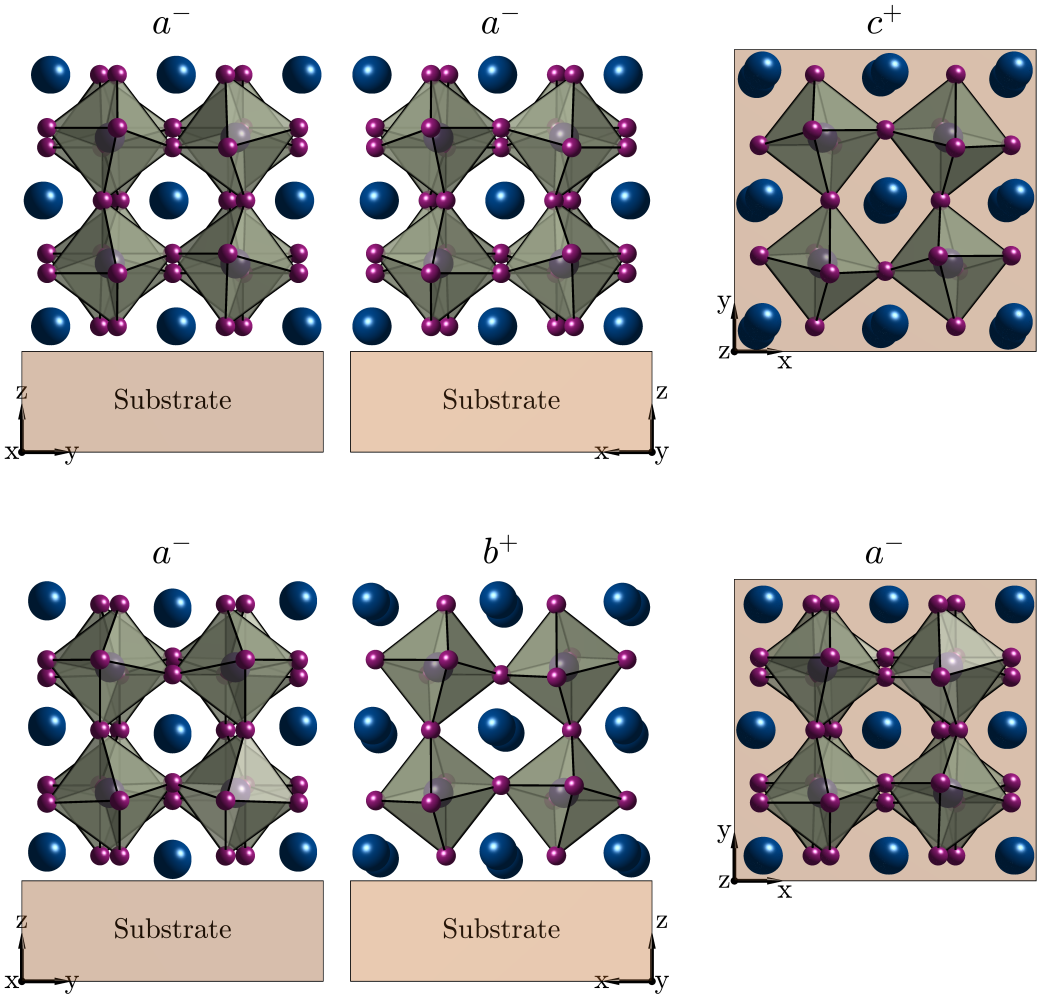

Figure 2.6: Different rotational orderings in a perovskite with *Pnma* symmetry on a substrate. From left to right the rotations about the pseudocubic x-, y, and z-axis are shown. In the upper panel, out-of-phase rotations about each in-plane direction and in-phase rotations about the out-of-plane direction leads to an $a^-a^-c^+$. In the lower panel the in-phase rotations lies about the in-plane pseudocubic y-axis, resulting in an $a^-b^+a^-$ tilt pattern.

The effect of strain for different substrate orientations

Up until now examples where perovskites have been oriented such that the out-of-plane direction was [001] have been examined to look at how different strain in the (001) plane affect the octahedral rotations in these perovskite compounds. The

out-of-plane direction depends on how the substrate is oriented and, hence, other orientations are possible – figure 2.7 showing one alternative, the [111] orientation – and the octahedral connectivity can be affected differently by strain for these orientations. This is shown theoretically by the use of DFT calculations by Moreau *et al.* in reference [31]. In this article the strain-octahedral rotation coupling was investigated for $LaAlO_3$ strained in the (001) and (111) plane. They found that compressive strain in the (001) plane favoured out-of-plane rotations, while tensile strain favoured in-plane rotations, in agreement with what was found by Hatt and Spaldin in reference [27]. $LaAlO_3$ strained in the (111) plane, however, showed the opposite behaviour, favoring in-plane rotations under compressive strain and out-of-plane rotations for tensile strains.

Another interesting result in this article was that while a 1% tensile strain in the (001) plane – favouring in-plane rotations – had a global minimum for equal magnitudes of rotation about the in-plane pseudocubic [100] and [010] directions, no such unique minimum was found for the system with 1% compressive strain in the (111) plane – also favouring in-plane rotations. Rather, a continuous minima was found for different combinations of in-plane rotations about the pseudocubic $[1\bar{1}0]$ and $[11\bar{2}]$ directions, resulting in an energy landscape compatible with a Goldstone-like mode.

In another article Moreau *et al.* investigated the strain-phonon coupling – that is, how the phonon mode frequencies in a highly symmetric perovskite changes with strain – for 20 different perovskite compounds strained in the (001) and (111) plane [32]. Here they considered the in-phase rotations, out-of-phase rotations, and polar phonon modes. They found that when strained in the (001) plane the favouring of certain phonon modes for different strains followed the already established trends, while when strained in the (111) plane a more complex trend was found, depending on both the Goldschmidt tolerance factor (t) and the electric charge of the A and B cations.

2.4 Interfacial couplings

So far the in-plane lattice parameters of the substrate material have been considered to look at how lattice parameter mismatch between a substrate and a film material (strain) affect the octahedral rotations in the film material. In this section, another effect present in systems of perovskite films epitaxially grown on perovskite substrates, will be covered – the interfacial coupling effect. In addition to strain, the symmetry and structure of the substrate can also have an impact on the film [15] – after all the BO_6 octahedral network must stay corner-connected. This can for example lead to a propagation of the substrate tilt pattern into the film [33, 34]. In addition, the octahedral network in the substrate layers in proximity to the film can be affected by the bulk tilt pattern in the film material. As a result, the interface layer between the film and substrate can differ from any layer

structure seen in either of the bulk materials. All these effects can simultaneously contribute to the properties of the substrate/film system [15], and is called the octahedral proximity effect [13].

This effect was shown in cubic $SrFeO_3$ films on tetragonal $SrTiO_3$ substrates, by the use of DFT calculations, by Rondinelli and Spaldin [34]. The tetragonal phase of $SrTiO_3$ has the $I4/mcm$ symmetry with out-of-phase rotations about one pseudocubic axis ($a^0a^0c^-$ tilt pattern), while bulk cubic $SrFeO_3$ possesses no rotations ($a^0a^0a^0$ tilt pattern). Despite that no rotations exist in bulk $SrFeO_3$ the rotations in the substrate had penetrated into the first two interfacial layers of the $SrFeO_3$ film. Rondinelli and Spaldin also showed that these rotations could not have been obtained by the biaxial strain alone.

By growing films with different tilt patterns on substrates with various tilt patterns – to obtain a variety of different symmetry-mismatch between two materials – one can investigate how these tilt patterns propagate into the substrate and film materials, and how this affects the material properties of the system. In reference [35] Hallsteinsen *et al.* observed novel properties in the interface layers of $LaFeO_3$ in a $La_{0.7}Sr_{0.3}MnO_3/LaFeO_3/SrTiO_3$ (LSMO/LFO/STO) heterostructure grown in the pseudocubic [111] direction. Bulk LFO is antiferromagnetic (possessing no net magnetic moment), nevertheless, a magnetic moment was observed in the two to four interface layers into the LFO at the LSMO/LFO interface. At the interface between LSMO and LFO the different tilt patterns – $a^-a^-a^-$ for LSMO and $a^-a^-c^+$ for LFO – produce a symmetry mismatch at this interface. Combined with DFT calculations they showed that this mismatch leads to a reduction of the in-phase rotations in LFO in two to four interface layers, consistent with the induced magnetism.

Another example where such symmetry mismatch have induced new properties in the interface layer is in $BiFeO_3$ (BFO) grown on $La_{0.7}Sr_{0.3}MnO_3$ (LSMO) in the [001] direction [36]. Here Borisevich *et al.* showed that a phase with reduced band gap was induced in a thin BFO interface layer.

In addition to looking at how the tilt patterns propagate across the interface, it is also interesting to look at how many layers, in proximity to the interface, having distortions due to the interface effects – that is the penetration length of the rotations. This is interesting because it is this region only that is controllable by the octahedral control parameter associated with the proximity effect and interfacial couplings [13]. At lengths longer than this penetration length from the interface the octahedral network in the substrate will have the same structure as that for the bulk phase of the substrate, and the octahedral network of the film will have the structure of that of the strained film phase.

2.4.1 Different substrate orientation and direction of growth

The magnetic moment induced in the LFO interface layer at the LSMO/LFO interface, found by Hallsteinsen *et al.* in an LSMO/LFO/STO [111] oriented system

(discussed above) has also been reported in a [001] oriented system [37]. However, the induced magnetic moment in this system was an order of magnitude smaller than what observed in the [111] oriented system. This implies that different orientations of the substrate – which determines the growth direction of the film layer – affect the structure at the interface by different degrees.

This effect can be explained by comparing the BO_6 octahedral connections at heterointerfaces where the out-of-plane axis lies along the pseudocubic [001] direction, with interfaces perpendicular to the [111] direction (figure 2.7). In [001] oriented systems each BO_6 octahedron in the interface layer of the film share one single oxygen anion with one $B'O_6$ octahedron in the substrate interface layer. In [111] oriented systems, however, each BO_6 octahedron shares three oxygen anions with three $B'O_6$ octahedra in the substrate interface layer.

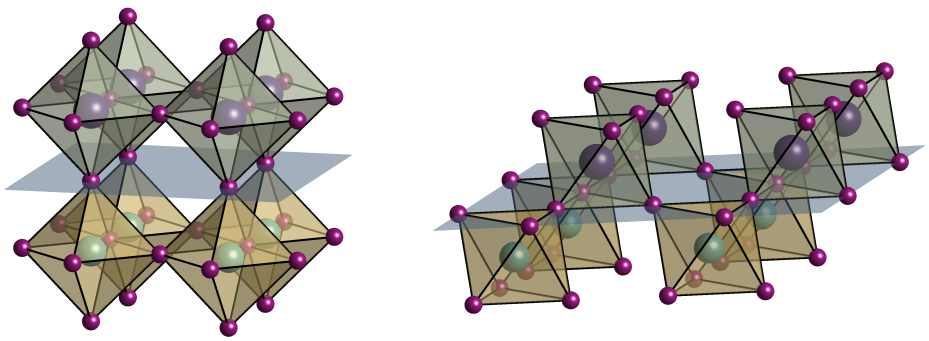

Figure 2.7: Heterointerfaces in a [001] oriented system (left) and a [111] oriented system (right).

Because only one oxygen anion is shared between the BO_6 and $B'O_6$ octahedra at [001] oriented interfaces, out-of-plane rotations do not necessarily couple as strongly as in-plane rotations in such systems. This is because out-of-plane rotations do not require displacements of the shared oxygen anions [13]. This is not the case for [111] oriented systems, however, where rotations about each of the three pseudocubic axes [100], [010], and [001] require displacements of at least two of the shared oxygen anions at the interface. This implies that the strength of the octahedral coupling at the interface is not discriminating regarding which pseudocubic axis the rotations lies about.

These effects are well illustrated in reference [38], where Moreau *et al.* looked at heterointerfaces of $La_{2/3}Sr_{1/3}MnO_3$ (LSMO) films and $SrTiO_3$ (STO) substrates. They used DFT calculations to look at how octahedral rotations can couple across the interface, and how this coupling differed for [001] and [111] oriented systems.

In addition, both the low temperature tetragonal phase and the high temperature cubic phase of STO – with tilt patter $a^0a^0c^-$ and $a^0a^0a^0$ and symmetry $I4/mcm$ and $Pm\bar{3}m$, respectively – were considered. As there are two symmetry inequivalent orientations of tetragonal STO in the [001] orientation – either out-of-phase rotations about the out-of-plane direction ($a^0a^0c^-$) or one of the in-plane directions (e.g. $a^-b^0b^0$) – the difference in penetration length for in-plane and out-of-plane rotations was also studied by looking at both of these substrate tilt patterns.

For the [001] oriented systems they found that the tensile biaxial strain imposed on the LSMO film favored a $a^-a^-c^+$ tilt pattern and $Pnma$ symmetry in LSMO. The coupling of octahedral rotations from the substrate into the film layer was almost identical for the $a^0a^0a^0$ and $a^0a^0c^-$ substrate, where the in-plane rotations increased simultaneously to its equilibrium strained bulk values over four LSMO layers. On the other hand, the magnitude of the out-of-plane rotations varied for different distances from the interface, and changed from out-of-phase rotations in the first two interface layers to in-phase rotations in the third and following layers. In the system with an $a^-b^0b^0$ tilt pattern in the substrate, however, the octahedral coupling was different. The rotations about the in-plane axis with out-of-phase rotations in the substrate reached the equilibrium strained bulk value after the first LSMO layer. The out-of-plane rotations also differed from those seen in the systems with the other tilt patterns in the substrate. This showed that in-plane rotations coupled more strongly than out-of-plane rotations.

In the [111] oriented systems the $a^-a^-a^-$ tilt pattern with $R\bar{3}c$ symmetry was found for the LSMO strained in the (111) to STO. Different couplings was found for the substrates with tilt patterns $a^0a^0a^0$ and $a^0a^0c^-$. For the case with an $a^0a^0a^0$ tilt pattern in the substrate, all rotations increased simultaneously to their equilibrium strained bulk values after the first LSMO layer, indicating that the octahedral coupling was stronger from the film to the substrate than from the substrate to the film. For the substrate with an $a^0a^0c^-$ tilt pattern, however, all rotations reached the equilibrium strained bulk values over seven LSMO layers (corresponding to the same length scale – about 14 Å – as four [001] oriented LSMO layers). The rotations about the different pseudocubic axes reach this value differently: the rotations about the axis with out-of-phase rotations in the substrate reached the equilibrium value from above, while the rotations about the other pseudocubic axes reach it from below. The same penetration length about all rotational axes indicated that the octahedral coupling in the [111] oriented systems were equally strong about each pseudocubic axis.

2.5 Coherent superlattices and multilayer heterostructures

The last octahedra control parameter discussed by Rondinelli *et al.* in reference [13] is the periodicity and periodicity ratio in coherent superlattices. In a superlattice $(AB\mathrm{O}_3)_m/(A'B'\mathrm{O}_3)_n$, where m and n is the number of pseudocubic unit cells in each film layer along the out-of-plane axis, the periodicity (m and n) and the superlattice composition, given as $C = m/(m+n)$, can be varied to obtain different material properties [13]. The periodicity can be chosen to be shorter than the penetration length – associated with the proximity effect, discussed above – to maximize the interface coupling effect in the octahedral network. In this way the superlattice composition can be varied to tune the connectivity [13]. This was shown for short-period $(\mathrm{LaNiO_3})_\mathrm{m}/(\mathrm{SrMnO_3})_2$ superlattices, where $m = 1, 2, 4$ by May *et al.* in reference [39]. Bulk $\mathrm{LaNiO_3}$ have an $a^-a^-a^-$ tilt pattern, while $\mathrm{SrMnO_3}$ have an $a^0a^0a^0$ tilt pattern. They showed that for small m values the rotations were suppressed in the $\mathrm{LaNiO_3}$ film layers, while larger values lead to rotations in the $\mathrm{SrMnO_3}$ film layers. They demonstrated that the in-plane and out-of-plane B-O-B bond angles could be tuned by 13°and 16°, respectively, with the superlattice composition C, and that this range of bond angles are much larger than that produced by biaxial strain alone.

In addition to the superlattice composition control there are several examples of where an ultrashort periodicity of both perovskites in the superlattice have induced new material properties not found in either of the bulk materials. One example is induced improper ferroelectricity in $\mathrm{PbTiO_3}/\mathrm{SrTiO_3}$ multilayers [9].

2.6 Summary

To achieve control of octahedral rotations in TMO perovskites, three different ways to manipulate the octahedral rotations in perovskite films and at perovskite/perovskite interfaces have now been investigated. In section 2.3.1 the effect bi-axial strain can have on the octahedral rotations in perovskite films was covered, while the interfacial couplings of octahedral rotations at perovskite/perovskite interfaces, and how these coupling could be used to control the octahedral rotations in layers in proximity to the interface, was explored in section 2.4. Section 2.5 looked at how this coupling effect could be utilized further, by considering how octahedral rotations in perovskite superlattices were affected when the film layer thicknesses in superlattices were varied.

When doing experiments to investigating how material properties and crystal structures change in perovskite superlattices and perovskite films, – with respect to their bulk material properties and structures, – it is difficult to decouple the effects of strain and interfacial coupling in these systems. For example, it can be difficult to tell whether a certain tilt pattern in a film material is caused by the bi-

axial strain from the substrate, the tilt pattern of the substrate or a combination between these two factors. If one could distinguish how these factors affected the system, a better understanding of how the octahedral rotations can be controlled by varying these factors, might be obtained. This is possible by the use of density functional theory (DFT), where the effects of strain can be completely decoupled from the effects of interfacial couplings.

Looking at such systems theoretically, by the use of DFT, therefore opens for the possibility to study how one can achieve octahedral control in perovskite structures, and to obtain a better understanding of how different factors affect the octahedral rotations. Hence, one can for example study how to control the direction of the Néel vector in antiferromagnetic perovskites as $LaFeO_3$. As the Néel vector in the $LaFeO_3$ structure lies along the orthorhombic **a** axis, control of the direction of this axis might lead to control of antiferromagnetism in $LaFeO_3$. How density functional theory calculations are performed will be covered in the next chapter.

Chapter 3

Density functional theory

In several of the examples given in the previous chapter, density functional theory (DFT) was used to support findings in experimental studies or for predicting structure coupling effects in different kind of systems. DFT is the main tool in this master thesis, and is a numerical method where the aim is to calculate the ground-state energy of a system by solving the Schrödinger equation. When this ground-state energy is found the structural and electronic configurations of the ground state will also be known. This chapter starts by addressing some important DFT calculation parameters in section 3.1, and then covers some important aspects in the construction of supercells and superlattices that are to be used in DFT calculations, in section 3.2. In the last section, section 3.3, two different DFT calculation methods are explained. The aim in the first method is to find the relaxed structure in a system with determined symmetry (section 3.3.1), while the aim of the second method is to find the phonon modes of highly symmetric structures, and thereafter freeze in selected phonon modes in the search of the ground state structure (section 3.3.2).

3.1 DFT model parameters

As for any numerical method, break conditions corresponding to different model parameters must be deliberately set when performing DFT calculations. By choosing break conditions that are adequately strict the numerical accuracy of the results can be increased. At the same time one wants the computational expense of the calculations to be as low as possible. This can be obtained by choosing less strict break conditions. Hence, one has to find the break conditions that gives a sufficient numerical accuracy at the same time as the computational expense is reasonable. This is done by finding the break conditions for where the results are converged. The different break condition values for where the result converges depend greatly on the physical system under consideration, and must therefor be found by performing so-called convergence tests when a new system is introduced.

When performing these convergence tests only the value of the model parameter under consideration is changed for the different calculations.

One of these break conditions is the size of the k point mesh – that is, how many k points that are to be evaluated in each direction in k space over the Brilloun zone (BZ) – to obtain a sufficiently strict k point density. Figures 3.1 and 3.2 show a convergence test performed for the k point mesh size with respect to the resulting energy and lattice parameter, respectively, for a cubic unit cell of $SrTiO_3$. This unit cell corresponds to one perovskite functional unit (f.u.). The convergence for the use of two different kinds of k point meshes – Monkhorst-Pack (MP) mesh and Gamma (G) mesh – are shown, and the energy and lattice parameter differences are with respect to the results from the calculations using a $12 \times 12 \times 12$ Monkhorst-Pack mesh.

For this system, the figures show that the energy and lattice parameters are well converged for both kinds of k point meshes for a k point mesh size of $8 \times 8 \times 8$.

Other examples of model parameters where a break condition must be set are:

the cut-off energy which sets an upper limit for the kinetic energy of the plane waves that are included in the basis set in the DFT calculations [40].

the break condition for the electronic self-consistency-loop which stops the electronic iteration problems when the energy difference between two consecutive iterates is smaller than this value [41, Ch. 3].

the break condition for the ionic relaxation loop which can be set to either stop the ionic iteration problem in the calculation when the energy difference between two consecutive steps is smaller than a set value, or, alternatively, stop the iteration problem when the force on each nuclei is smaller than a set value [40].

In DFT+U calculations, appropriate Hubbard U corrections must be set, such that the electronic and structural properties of the system correspond as well as possible with the real system.

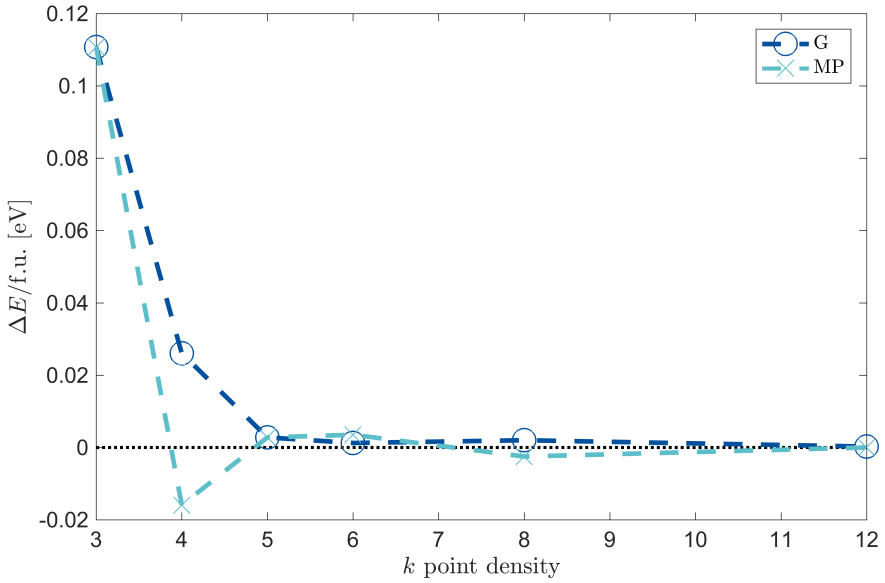

Figure 3.1: The energy difference – with respect to the calculation using a $12 \times 12 \times 12$ Monkhorst-Pack mesh – for different k point densities for a $SrTiO_3$ unit cell.

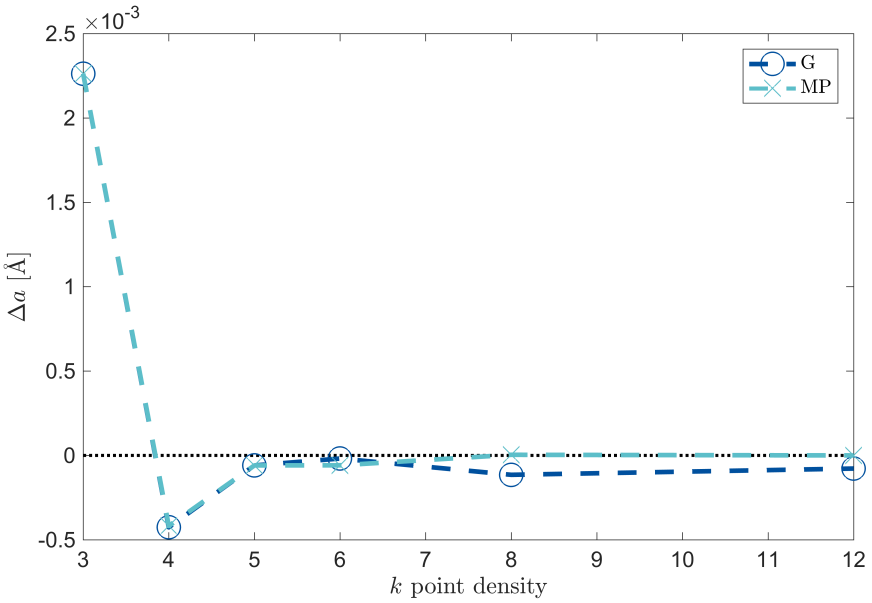

Figure 3.2: The lattice parameter difference – with respect to the calculation using a $12 \times 12 \times 12$ Monkhorst-Pack mesh – for different k point densities for a $SrTiO_3$ unit cell.

3.2 Construction of supercells and superlattices for DFT calculations

Density functional theory has the important advantage over experimental research that it can easily distinguish between different factors that influence the system, and hence look at these factors separately [15]. For example one can look at how strain affect a system alone, excluding all other factors that may influence the system – as interface effects. This is done by comparing a fully relaxed cell of the film material with a cell of the film material that has only been allowed to relax in one direction, while the lattice parameters orthogonal to this direction have been set equal to those corresponding to a substrate, to model biaxial strain.

Even though this technique is advantageous because one can investigate how strain affect the structure alone, it also omits substrate/film interface effects often crucial to the structural properties in proximity of the interface. To model these effects one has to construct superlattices containing both the substrate material and the film material(s).

Because periodic boundary conditions are used in DFT calculations the number of substrate unit cells and film material unit cells along the out-of-plane direction must be adequately high if the system is to model a single heterointerface, such that the results represent a "substrate/single film layer" system and not a "multiple film layers" (superlattice) system. Alternatively, the middle unit cell(s) of the substrate layer can be locked in their bulk positions. By choosing the latter approach to model a substrate one can use smaller superlattices and the computational expense decreases. If one wants to model a superlattice, however, the number of unit cells for each film layer should be chosen so that it is as equal as the experimental situation as possible.

When constructing a supercell or superlattice for the use in DFT calculations it is important to make sure that the dimensions about each pseudocubic axis allow for all material properties (e.g. structural and magnetic properties). These property aspects is covered in section 3.2.1. At the same time it is important that the structure is not bigger than necessary, to lower the computation expense. Another way to lower the computational expense is to make sure the superlattices have as many symmetry elements as possible, as symmetry equivalent regions in k space are calculated together. These symmetry aspects is covered in section 3.2.2.

3.2.1 Property aspects

If the structure under consideration is a perovskite structure, for example, the supercell or superlattice must be adequately large along each pseudocubic axis such that all structural properties, as rotations, are allowed [15]. For a perovskite with the $a^0a^0a^0$ tilt pattern and $Pm\bar{3}m$ symmetry, one unit cell along each lattice parameter is sufficient, while structures with non-zero rotations must have larger cells. If the $a^0a^0a^0$ structure is to be used in phonon mode calculations

(section 3.3.2), however, the structure has to have at least two unit cells along each pseudocubic lattice parameter, to allow for rotations about each pseudocubic axis.

Regarding the number of out-of-plane unit cells in supercells and superlattices one also has to be aware that an odd number of unit cells can lead to artificial frustration of the tilt system [15]. This is when the out-of-plane rotations are out-of-phase but an odd number of pseudocubic unit cells does not allow this.

If the material to be modelled possesses magnetic moments at certain ions, the supercell or superlattice must contain as many of these ions along each pseudocubic direction such that the magnetic structure can be properly modelled. If the material is a ferromagnetic perovskite, only one magnetic ion is sufficient to model the the magnetic structure, as all magnetic moments point in the same direction (figure 3.3a). For an antiferromagnetic structure (figures 3.3b-d) more magnetic ions must be included in the lattice to model the correct structure.

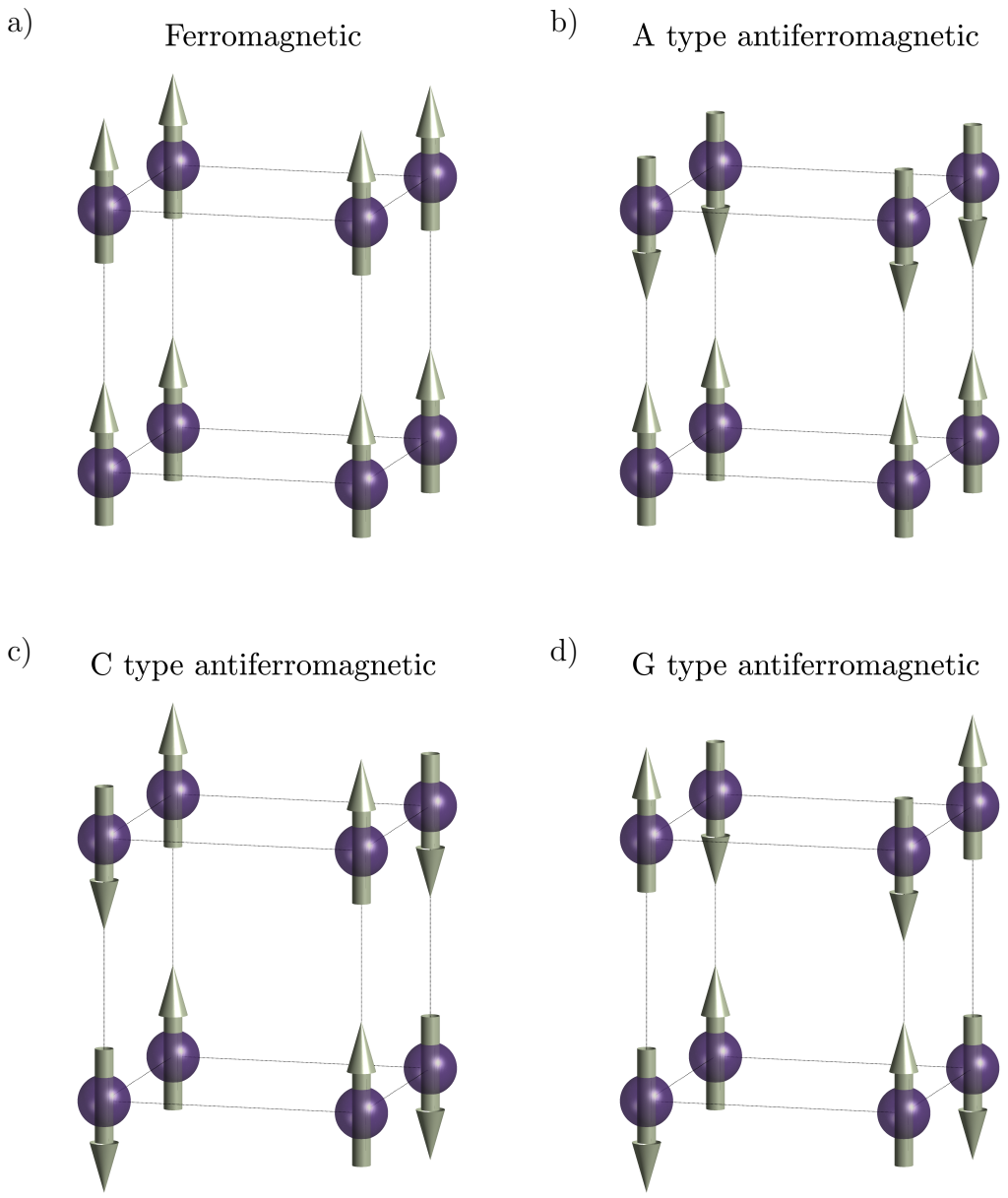

Figure 3.3: Magnetic structures in perovskites. The spheres indicate the positions of the magnetic cations and the arrows indicate if the overall spin configuration for the cation is spin-up or spin-down.

3.2.2 Symmetry aspects

When constructing superlattices of perovskite compounds one can make sure the structure has a symmetry element on the out-of-plane axis by following the steps illustrated in figure 3.4 for a (3,3) [001] oriented superlattice. First, shift the

superlattice such that one film layer occupies all middle unit cells along the out-of-plane axis. Second, make sure that both interfaces are equally terminated. Note that, for superlattices where the perovskite compounds have different A and B cations this equal termination on both interfaces leads to a $(m \pm 1/2, n \mp 1/2)$ superlattice.

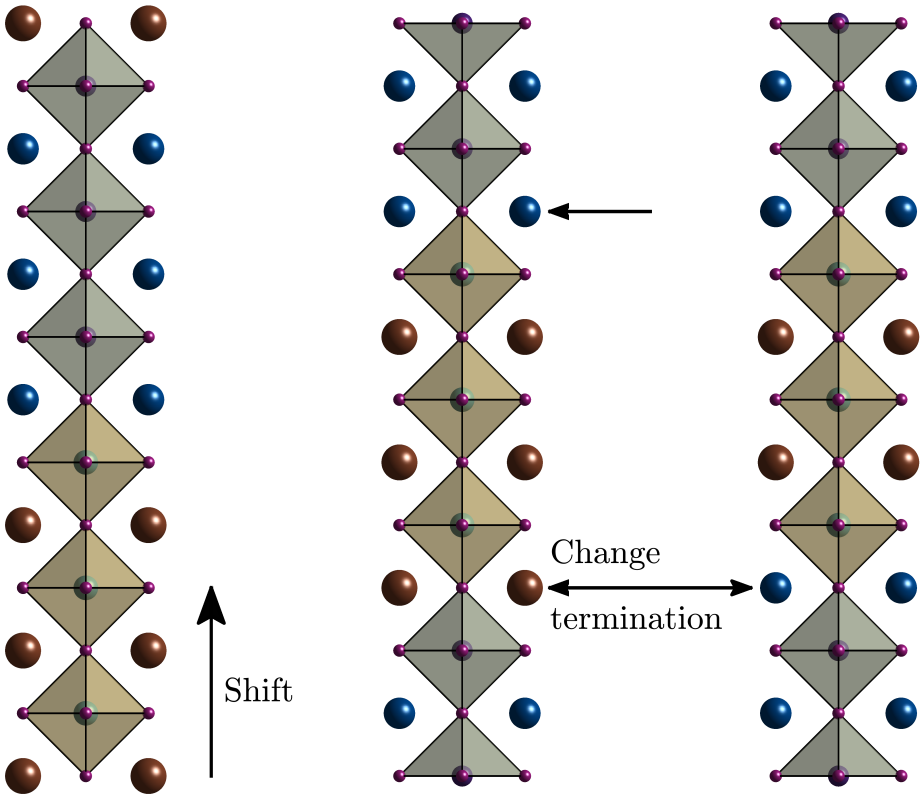

Figure 3.4: Steps to make an asymmetric superlattice along the out-of-plane direction (left and middle) symmetric along the out-of-plane direction (right).

3.3 DFT calculation methods

In the search of the ground state structure of a system there are several different approaches one can use. In this master thesis two methods were used: structural calculations (section 3.3.1) and phonon mode calculations (section 3.3.2).

3.3.1 Structural calculations

In structural calculations the symmetry of the supercell or superlattice is set in an initial trial structure. The symmetry can for example be set equal to that

found for the bulk materials for each compound in the superlattice. The out-of-plane lattice parameter and the internal ionic coordinates can then be relaxed. Alternatively, only the ionic positions can be allowed to relax. The latter method is favorable if one wants to – more or less – fix the out-of-plane unit cell lengths, and hence keep the octahedral volumes approximately fixed.

The resulting structure in the film and substrate layers can then be compared to the structure of their bulk compounds, too investigate how the heterointerface affect the structure in proximity to the interface.

3.3.2 Phonon mode calculations

In phonon mode calculations the goal is to find the phonon modes of a highly symmetric structure. For perovskite structures this corresponds to a structure with no rotations ($a^0a^0a^0$ tilt pattern). By comparing the energy of this highly symmetric structure to several approximately equal structures – with only small, close-to-zero displacements of specific ions, – one can find the curvature in energy for different kinds of periodic displacements – that is, phonon modes [42]. The square of a specific phonon mode's frequency is proportional to the curvature in energy for that mode. This means that for all real phonon mode frequencies the curvature in energy is positive and displacements corresponding to these phonon modes leads to larger energies for the system, and are therefore not energetically favorable for the structure. If a phonon mode frequency is imaginary, however, the curvature in negative, indicating that displacements corresponding to this phonon mode is energetically favorable for the system as it lowers its energy, and hence, that the highly symmetric structure is not stable. The phonon modes with imaginary frequencies can therefore give a clue of what kind of distortions from the highly symmetric structure that might be present in the ground state structure for the system.

By freezing in different combinations of phonon modes with imaginary frequencies, one gets different structures whom energies can be compared to find the structure with the lowest energy [15]. To search for the ground state structure of the system, different initial trial structures – corresponding to structures where one or several of the phonon modes with imaginary frequencies have been frozen in – are relaxed, and their resulting energy and structure can be compared to each other and that of the highly symmetric structure. Hence, one can obtain an overview of stable structures for the system.

In superlattices, containing two or more different materials, the phonon modes associated with one of the materials can propagate across the interfaces and into the other material(s), resulting in an interface layer with different structural properties than those found in the bulk film materials.

In this master thesis the focus was at three different kinds of phonon modes common in perovskite structures; in-phase rotations, out-of-phase rotations, and polar phonon modes. These phonon modes manifest themselves somewhat differ-

ent, depending on what crystallographic plane the structure is strained in – that is, the orientation of the system. Below the in-plane and out-of-plane version for each of these three phonon modes are illustrated and explained for [001] oriented systems, followed by [111] oriented systems.

Rotation phonon modes for [001] oriented systems

In [001] oriented systems, the pseudocubic rotation axes – [100], [010], and [001] – lies along the in-plane ([100] and [010]) and out-of-plane ([001]) axes of the system. For cubic systems the in-plane axes are symmetry equivalent, and the phonon modes corresponding to the same type of phonon mode about the two in-plane axes therefore have that same phonon mode frequency. The in-plane ($\parallel$) and out-of-plane ($\perp$) phonon modes for the out-of-phase and in-phase rotation modes (Rot^- and Rot^+, respectively), and the polar phonon modes (P) are illustrated in figure 3.5 for a [001] oriented system.

The orientation of the system relative to the rotation axes makes in-plane phonon modes to correspond to rotations about the pseudocubic [100] and [010] rotation axes, and out-of-plane phonon modes to correspond to rotations about the pseudocubic [001] rotation axis. This is summarized in table 3.1 together with the tilt pattern corresponding to a system where these phonon modes have been frozen in.

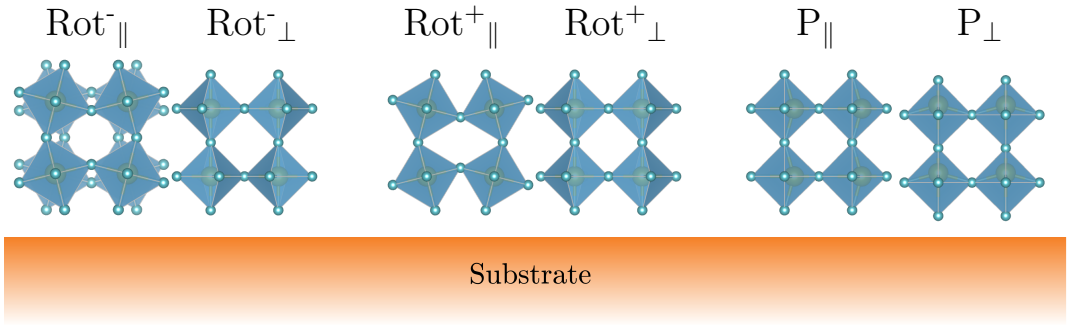

Figure 3.5: The in-plane ($\parallel$) and out-of-plane ($\perp$) phonon modes for the out-of-phase and in-phase rotation modes (Rot^- and Rot^+, respectively), and the polar phonon modes (P) for a [001] oriented system. Figure made in VESTA [14].

Table 3.1: The rotation modes and their corresponding pseudocubic rotation axis and tilt pattern, in Glazer notation, for a [001] oriented system.

Phonon mode	Rotation axis	Tilt pattern
$\mathrm{Rot}^{-}{}_{\parallel}$	[100]	$a^-b^0b^0$
	[010]	$a^0b^-a^0$
$\mathrm{Rot}^{-}{}_{\perp}$	[001]	$a^0a^0c^-$
$\mathrm{Rot}^{+}{}_{\parallel}$	[100]	$a^+b^0b^0$
	[010]	$a^0b^+a^0$
$\mathrm{Rot}^{+}{}_{\perp}$	[001]	$a^0a^0c^+$

Rotation phonon modes for [111] oriented systems

In a system where a pseudocubic unit cell has been rotated by the rotation matrix:

$$R = \begin{bmatrix} 1 & 0 & 1 \\ \bar{1} & 1 & 1 \\ 0 & \bar{1} & 1 \end{bmatrix}, \tag{3.1}$$

to obtain an [111] oriented system, the in-plane lattice parameters lies along the pseudocubic $[1\bar{1}0]$ and $[01\bar{1}]$ directions. Rotations about both the out-of-plane [111] axis and the in-plane axes therefore include rotations about several pseudocubic rotation axes (see table 3.2). As for the [001] oriented cubic systems, rotations about the in-plane lattice parameters are symmetry equivalent also for [111] oriented cubic systems. In addition, in-phase rotations about each of the three pseudocubic rotation axes are symmetry equivalent in an [111] oriented cubic system. This leads to three symmetry equivalent phonon modes – each corresponding to rotations about one pseudocubic rotation axis – with the same frequency. Hence, in [111] oriented systems it is not distinguished between in-plane and out-of-plane in-phase rotation modes ($\mathrm{Rot}^{+}{}_{\parallel}$=$\mathrm{Rot}^{+}{}_{\perp}$=$\mathrm{Rot}^{+}$).

The rotation and polar phonon modes for [111] oriented systems are illustrated in figure 3.6, and the rotation phonon modes with their corresponding rotation axes and tilt patterns are given in table 3.2.

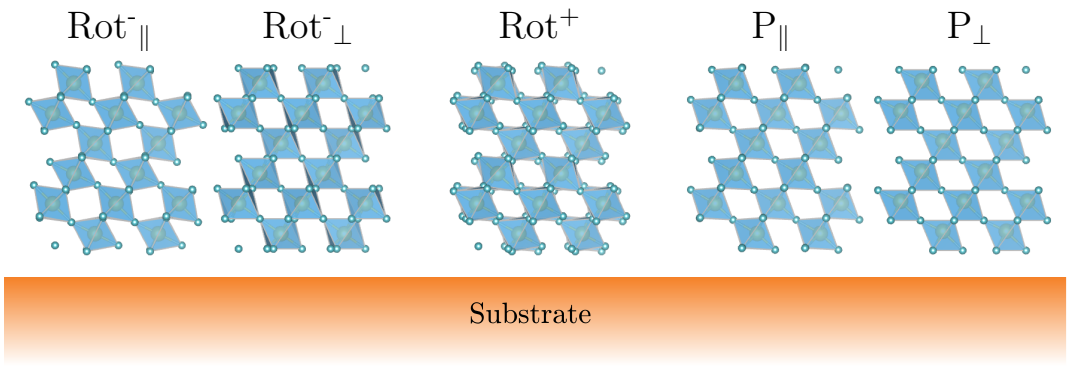

Figure 3.6: The in-plane (∥) and out-of-plane (⊥) phonon modes for the out-of-phase and in-phase rotation modes (Rot^- and Rot^+, respectively), and the polar phonon modes (P) for a [111] oriented system. Figure made in VESTA [14].

Table 3.2: The rotation modes and their corresponding pseudocubic rotation axis and tilt pattern, in Glazer notation, for an [111] oriented system.

Phonon mode	Rotation axis	Tilt pattern
$Rot^-_{\parallel}$	$[1\bar{1}0]$	$a^-a^-c^0$
	$[01\bar{1}]$	$a^0b^-b^-$
$Rot^-_{\perp}$	[111]	$a^-a^-a^-$
Rot^+	[100]	$a^+b^0b^0$
	[010]	$a^0b^+a^0$
	[001]	$a^0a^0c^+$

Chapter 4

Method

In this chapter the calculations done for this master thesis are explained. The chapter is divided into five sections. In the first section (section 4.1) the model system is explained. The second section (section 4.2) covers some general information regarding how the calculations were performed – including converged model parameter values, – while the third and fourth section focuses on the methodology for the two different kinds of calculation methods – phonon mode calculations (section 4.3) and structure calculations (section 4.4), respectively – used to carry out these calculations. In the final section, section 4.5, an overview of the systems investigated during this master thesis is given.

4.1 Model system

The aim of this master thesis was to investigate how octahedral rotations and tilts couple at heterointerfaces and in superlattices, and how different film layer thicknesses and system orientations affect this coupling. Both phonon mode calculations and structure calculations were performed to investigate these effects, and the results from the different calculation methods were compared. Hence, the possibility to rely on phonon mode calculations to investigate octahedral coupling in superlattices were also studied.

Superlattices of $LaFeO_3$ (LFO) and $SrTiO_3$ (STO) oriented in the [001] and [111] pseudocubic direction – where LFO was strained to STO in the (001) and (111) plane, respectively, – were used as the model system. The film layer thicknesses m and n were varied symmetrically ($m = n$) and asymmetrically ($m \neq n$). All interfaces, apart from those in the LFO_1/STO_1 superlattices, were TiO_2 terminated for the [001] oriented superlattices and Ti terminated for the [111] oriented superlattices. Hence, when the superlattices are expressed as LFO_m/STO_n – or (m,n) for short – m and n depict the number of FeO_6 and TiO_6 octahedra in each LFO and STO film layer along the out-of-plane direction, respectively.

The perovskite compounds were chosen based on their material properties.

LFO is a G type antiferromagnetic insulator with a Néel vector along the orthorhombic **a** axis and a Néel temperature of 738 K [10]. The bulk structure is orthorhombic and has an $a^-a^-c^+$ tilt pattern and $Pnma$ symmetry. STO is a non-magnetic insulator which undergo a structural phase transition at 105 K, where it is tetragonal with an $a^0a^0c^-$ tilt pattern and $I4/mcm$ symmetry at temperatures lower than 105 K, and cubic with an $a^0a^0a^0$ tilt pattern and $Pm\bar{3}m$ symmetry at temperatures above 105 K. In this master thesis the focus was on the cubic phase of STO. It has previously been showed that by growing LFO films on an STO substrate, the structure and the orientation of the Néel vector in LFO have been changed from that of bulk LFO [43], indicating that it is a strong coupling between the structure and the orientation of the magnetic moments in LFO.

4.2 The DFT calculations and model parameters

The DFT calculations were performed in the Vienna ab initio Simulations Package (VASP) using the PBEsol functional [44] and projector-augmented wave (PAW) potentials [45, 46]. The electronic configurations for the elements used in these calculations are given in table 4.1. For the La f states and Fe d states a PBEsol+U approach was used by applying Dudarevs method [47]. U values of 8 and 4 eV were used for the La f states and Fe d states, respectively. These values were chosen based on the results from a previous project thesis where these values were shown to give a band gap energy and pseudocubic cell volume corresponding well with experimental values for LFO. In the same project, converged DFT model parameters for the k point density (using a Monkhors-Pack mesh), cut-off energy, and break conditions for the electronic self-consistency loop and ionic relaxation loop, were found for LFO and STO. These values were reused in this project and are given in table 4.2 together with a description of the parameters [40] and their corresponding tag in VASP.

Table 4.1: The electronic configurations of the elements used in this master thesis.

Element	Electronic configuration
La	$5s^25p^65d^16s^2$
Fe	$3p^63d^44s^2$
Sr	$4s^24p^65s^2$
Ti	$3s^23p^63d^24s^2$
O	$2s^22p^4$

The in-plane lattice parameters were kept fixed in all calculations. The value of these in-plane lattice parameters corresponded to that of a fully relaxed STO

unit cell obtained in a calculation in the pre-project, using the model parameter values given in table 4.2. The pseudocubic lattice parameter obtained from this calculation was $a_{\mathrm{ps}} = 3.8958$ Å. The value of the out-of-plane lattice parameter was different depending on the calculation method, and will be explained in section 4.3 and 4.4.

Table 4.2: The converged model parameter values used in this master thesis.

VASP tag	Model parameter value	Model parameter description
ENCUT	550 eV	Cutoff energy for the plane-wave basis set. Only plane-waves with kinetic energy less than this value is included in the basis set.
EDIFF	10^{-8} eV	Break condition for the electronic self-consistency-loop. When the energy difference between two consecutive electronic steps are less than this value the electronic relaxation stops.
EDIFFG	-10^{-3} (eV/Å)	Break condition for the ionic relaxation loop. For negative values the ionic relaxation stops when all forces are less than the absolute value of EDIFFG.
k point density*	$8 \times 8 \times 8$	The number of subdivisions in the Brillouin zone. This particular k point density value correspond to a cubic STO unit cell with $a = 3.905$ Å using the original Monkhors-Pack approach to generate the k-mesh.

Some of the calculations in this master thesis involved hexagonal cells and superlattices. For these systems the original Monkhorst-Pack mesh is not applicable for symmetry reasons, therefore a "Gamma" mesh was used for these calculations. Because the convergence tests for these different kind of meshes show similar trends and both show convergence for a k point mesh size of 8 k points in each direction in k space ($8 \times 8 \times 8$) (see figures 3.1 and 3.2 in chapter 3) in such systems, the same k point density was used for both k point meshes.

*Not a VASP tag but is declared in the KPOINTS file.

4.3 Phonon mode calculations

In one of the two calculation methods used in this master thesis – the phonon mode calculations, – highly symmetric superlattices were build with the goal to find their phonon modes, and their corresponding frequencies. All calculations were performed by following four or five consecutive steps:

1. Build a highly symmetric supercell or superlattice.
2. Relax the **c** lattice parameter and the ionic positions in the structure.
3. Calculate the energy of the relaxed structure, and several structures with different kinds of displacements, to find the phonon modes of the high symmetry structure, and their corresponding frequencies. The displacements, phonon modes, and phonon mode frequencies were calculated by the phonopy software [42].
4. Visualize the phonon modes and – for the rotation modes – calculate the vector magnitudes of the displacement vectors for each layer about the out-of-plane direction in the structure. The vector magnitudes were calculated in MATLAB.
5. For some systems, phonon modes were frozen in and the resulting structure were then strained relaxed. The resulting rotations and tilts for these structures were then plotted and their corresponding energies compared.

Section 4.3.1 covers the first step for the two different orientations of supercells and superlattices, while section 4.3.2 describes the second and third step. The details of how the vector magnitudes was found is given in section 4.3.3, and section 4.3.4 covers the frozen-in phonon calculations. In tables 4.3 and 4.4 all superlattices used during step two and three, respectively, of the phonon mode calculation procedure in this master thesis are listed, together with their corresponding dimensions and orientation. The film layer thicknesses m and n for these superlattices were varied symmetrically ($m = n$), and are therefore expressed as (m,m). To lower the computational costs, some superlattices had smaller dimensions during the relaxation of the **c** lattice parameter and ionic positions (step two). The dimensions of these superlattices were increased prior to the calculations of the phonon modes (step three) to allow for both in-phase and out-of-phase rotations about each pseudocubic rotation axis. Table 4.4 also shows whether the fifth step, with the frozen in phonon modes, were performed on the supercell or superlattice, or not.

Table 4.3: Overview of the supercells and superlattices for which the second step in the phonon mode calculations were performed.

Orientation	ABO_3 or (m,m)	Dimensions [f.u.]
[001]	LFO	$2 \times 2 \times 2$
	STO	$2 \times 2 \times 2$
	(1,1)	$2 \times 2 \times 2$
	(2,2)	$2 \times 2 \times 4$
	(3,3)	$2 \times 2 \times 6$
[111]	LFO	$2\sqrt{2} \times 2\sqrt{2} \times 2\sqrt{3}$
	$(1,1)_{3,\mathrm{FM}}$*	$\sqrt{2} \times \sqrt{2} \times 2\sqrt{3}$
	$(1,1)_{6,\mathrm{AF}}$	$\sqrt{2} \times \sqrt{2} \times 4\sqrt{3}$
	(3,3)	$\sqrt{2} \times \sqrt{2} \times 2\sqrt{3}$

Table 4.4: Overview of the supercells and superlattices for which the third step in the phonon mode calculations were performed.

Orientation	ABO_3 or (m,m)	Dimensions [f.u.]	Fifth step performed (y/n)
[001]	LFO	$2 \times 2 \times 2$	n
	STO	$2 \times 2 \times 2$	n
	(1,1)	$2 \times 2 \times 2$	n
	$(1,1)_2$	$2 \times 2 \times 4$	n
	(2,2)	$2 \times 2 \times 4$	n
	(3,3)	$2 \times 2 \times 6$	y
[111]	LFO	$2\sqrt{2} \times 2\sqrt{2} \times 2\sqrt{3}$	n
	$(1,1)_{3,\mathrm{FM}}$	$2\sqrt{2} \times 2\sqrt{2} \times 2\sqrt{3}$	n
	$(1,1)_{6,\mathrm{AF}}$	$2\sqrt{2} \times 2\sqrt{2} \times 4\sqrt{3}$	n
	$(3,3)_2$	$2\sqrt{2} \times 2\sqrt{2} \times 4\sqrt{3}$	y

*The subscript number indicate how many times the (m,n) structure is repeated along the out-of-plane direction. No subscript means no repetition. The second subscript indicate whether the magnetic ordering in the superlattice is ferromagnetic (FM) or antiferromagnetic (AF).

4.3.1 Lattice construction

The first step in the phonon mode calculations was to construct the lattices. All supercells and superlattices for these calculations were build in the three-dimensional visualization program VESTA [14], with an $1 \times 1 \times 1$ cubic ABO_3 unit cell as the building block, corresponding to one functional unit (f.u.). The unit cell had the $a^0a^0a^0$ tilt pattern with the $Pm\bar{3}m$ symmetry, and lattice parameters $a = b = c = 3.895(8)$ Å – corresponding to the lattice parameter obtained for a fully relaxed cubic STO cell in the pre-project.

[001] oriented supercells and superlattices

The in-plane dimensions for all supercells and superlattices with the [001] orientation were 2×2 to allow both kind of rotation modes along each in-plane direction. The out-of-plane dimension was 2 for the LFO and STO supercells for the same reason, and 2, 4, and 6 for the (1,1), (2,2), and (3,3) superlattices, respectively. These dimensions also allowed for the G type antiferromagnetic ordering of the Fe ions (figure 3.3d in chapter 3).

The three [001] oriented superlattices are illustrated in figure 4.1. A symmetry element along the **c** lattice parameter direction was imposed by following the steps illustrated in figure 3.4 in chapter 3, for all superlattices except for the (1,1) superlattice. These steps were not followed for the (1,1) superlattice because a TiO_2 termination for all interfaces in this superlattice would have resulted in a superlattice where all Sr ions were replaced with La ions. Instead, no film layers contained a full STO nor LFO unit cell in the **c** lattice parameter direction, and the AO-BO_2-AO-BO_2 layers were ordered as LaO-FeO_2-SrO-TiO_2.

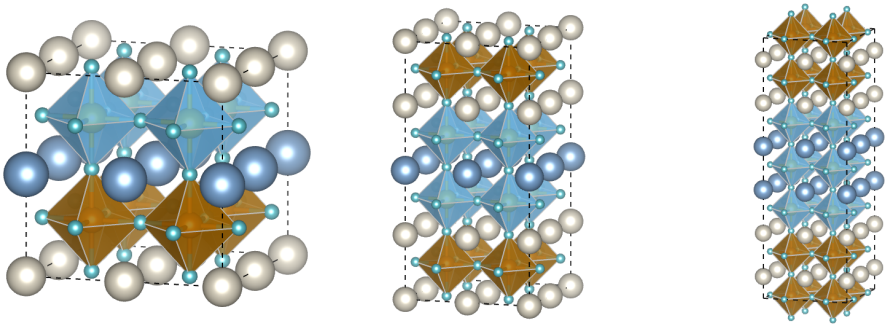

Figure 4.1: From left to right, the (1,1), (2,2), and (3,3) [001] oriented superlattices. Figures made in VESTA [14].

[111] oriented supercells and superlattices

To build the [111] oriented supercells and superlattices, the $1 \times 1 \times 1$ cubic ABO_3 unit cell was rotated with the rotation matrix given in equation 3.1 in chapter 3,

to obtain a hexagonal $\sqrt{2} \times \sqrt{2} \times \sqrt{3}$ unit cell oriented with the **c** lattice parameter parallel to the pseudocubic [111] direction. The number of ABO_3 cells along the out-of-plane direction in this hexagonal unit cell was three (see figure 4.2).

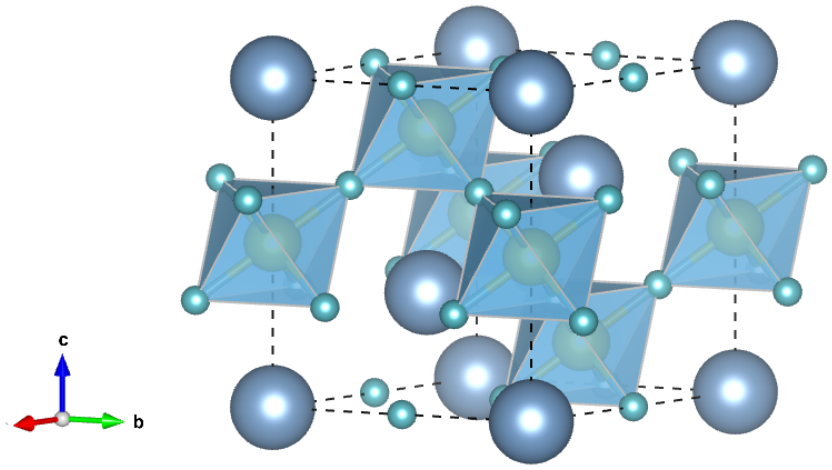

Figure 4.2: The highly symmetric ABO_3 hexagonal unit cell. Figure made in VESTA [14].

For the LFO supercell, the hexagonal unit cell was doubled along every lattice parameter to allow for both kinds of rotation modes about each pseudocubic rotation axis. This resulted in a supercell with dimensions $2\sqrt{2} \times 2\sqrt{2} \times 2\sqrt{3}$ that also allowed the for the G type antiferromagnetic ordering of the Fe ions.

The three [111] oriented superlattices are illustrated in figure 4.3. To minimize the computational cost, the [111] oriented unit cell was not doubled in the **a** and **b** lattice parameter directions for the [111] superlattices. This would still allow a G type antiferromagnetic ordering for the Fe ions – as long as the cell was increased appropriately along the **c** lattice parameter direction – which was sufficient for the relaxation calculations involved in step two of this calculation procedure.

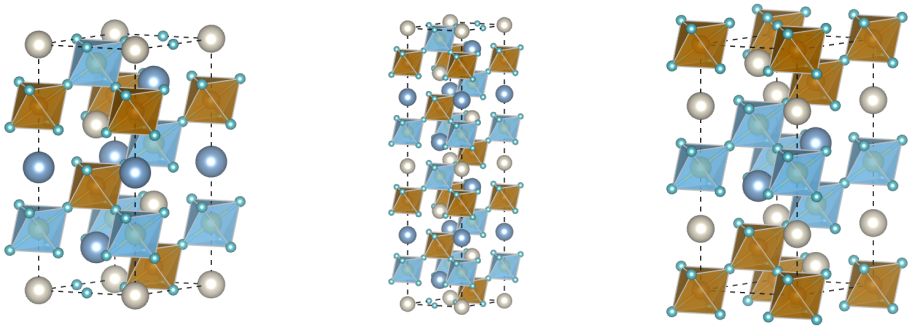

Figure 4.3: From left to right, the $(1,1)_{3,\mathrm{FM}}$, $(1,1)_{6,\mathrm{AF}}$, and (3,3) [111] oriented superlattices. Figures made in VESTA [14].

The hexagonal unit cell was doubled along the **c** lattice parameter direction for the $(1,1)_{3,\mathrm{FM}}$ superlattice. This resulted in three Fe-layers along the out-of-plane axis (see figure 4.3). As all Fe ions in the same Fe-layer have the same magnetic orientation in G type antiferromagnetic [111] oriented systems, an odd number of Fe-layers is not sufficient to make a system with zero net magnetization. Hence, this structure was used in a system with ferromagnetic (FM) ordering of the Fe ions in an (1,1) superlattice.

In order to make a (1,1) superlattice with zero net magnetization and G type antiferromagnetic ordering, the $(1,1)_{3,\mathrm{FM}}$ superlattice had to be doubled along the out-of-plane direction again, to obtain an even number of six Fe-layers (see figure 4.3). This superlattice was used in a system with antiferromagnetic (AF) ordering of the Fe ions, and is expressed as $(1,1)_{6,\mathrm{AF}}$.

For the (1,1) [111] oriented superlattices it was not possible to impose a symmetry element along the **c** lattice parameter for the same reason as for the (1,1) [001] oriented superlattice (described above). The resulting ordering of the layers were therefore LaO_3-Fe-SrO_3-Ti-LaO_3-Fe-SrO_3-Ti-LaO_3-Fe-SrO_3-Ti for the $(1,1)_{3,\mathrm{FM}}$ superlattice, and LaO_3-Fe-SrO_3-Ti-LaO_3-Fe-SrO_3-Ti-LaO_3-Fe-SrO_3-Ti-LaO_3-Fe-SrO_3-Ti-LaO_3-Fe-SrO_3-Ti-LaO_3-Fe-SrO_3-Ti for the $(1,1)_{6,\mathrm{AF}}$ superlattice.

To obtain a (3,3) superlattice the hexagonal building block was doubled along the out-of-plane direction to obtain six ABO_3 units along the out-of-plane axis. As for the (2,2) and (3,3) [001] oriented superlattices, a symmetry element along the **c** lattice parameter direction was imposed on the (3,3) superlattice by following the steps illustrated in figure 3.4 in chapter 3.

4.3.2 DFT calculations

When the construction of the highly symmetric supercells and superlattices were done, the **c** lattice parameter and the ionic positions in the structures were allowed to relax in strained relaxation calculations. When calculating the phonon modes of a highly symmetric system it is important that the ionic and electron positions have been relaxed to highly accurate positions. Therefore, the break condition for the electronic self-consistency-loop and the break condition for the ionic relaxation loop were set to even stricter values than those given in table 4.2 for these calculations, namely 10^{-9} eV and $(-)10^{-4}$ eV/Å, respectively.

Following is a description of the relaxation calculations and the calculations to find the phonon modes and phonon mode frequencies, corresponding to step two and three, respectively, in the phonon mode calculation procedure.

Relaxation calculations

Before the relaxation calculations could be started several model parameters had to be appropriately set for each supercell and superlattice. These model parameters corresponded to the atomic position accuracy for the structure, the k point

mesh size, and the magnetic ordering of the Fe ions.

The space group and atomic position accuracy in the superlattices were checked in the FINDSYM program [48]. For the superlattices where the atomic position accuracy was found to be less strict than 10^{-5} Å (default atomic position accuracy in VASP [40]) for the correct space group to be recognized by the program, the atomic position accuracy tag, SYMPREC, was set to the appropriate value such that VASP could recognize the correct space group. The space groups to be recognized for the different supercells and superlattices are given in table 4.5.

Table 4.5: Space groups of the supercells and superlattices for the different orientations for the relaxation calculations.

	Orientation	
Supercell/superlattice	[001]	[111]
STO	$Pm\bar{3}m$	-
LFO	$Pm\bar{3}m$	$Pm\bar{3}m$
(1,1)	$P4mm$	$F\bar{4}3m$
(2,2)	$P4/mmm$	-
(3,3)	$P4/mmm$	$P\bar{3}m1$

The k point density was set such that it corresponded as good as possible with the value given in table 4.2, for all supercells and superlattices. The corresponding k point mesh size together with mesh type is given in table 4.6.

Table 4.6: k point mesh size and mesh type – where MP=Monkhorst–Pack and G=Gamma – for the supercells and superlattices with different orientations for the relaxation calculations.

	Orientation and mesh type	
Supercell/superlattice	[001] and MP	[111] and G
STO	$4 \times 4 \times 4$	-
LFO	$4 \times 4 \times 4$	$3 \times 3 \times 2$
(1,1)	$4 \times 4 \times 4$	$(6 \times 6 \times 2)_{\mathrm{FM}}$ $(6 \times 6 \times 1)_{\mathrm{AF}}$
(2,2)	$4 \times 4 \times 2$	-
(3,3)	$4 \times 4 \times 1$	$6 \times 6 \times 2$

The last model parameter to be set was that of the magnetic ordering of the Fe ions. The magnetic ordering for the different supercells and superlattices were

set as shown in figures 4.4 and 4.5 for the [001] and [111] oriented systems, respectively. The magnetic moment for each ion in the systems were set with the MAGMOM tag in VASP. For the Fe ions a magnetic moment of either 5 (magnetic moment pointing up) of -5 (magnetic moment pointing down) was set, while the magnetic moments for the remaining ions were all set to 0 (no magnetic moment). Note that, as the (3,3) [111] oriented superlattice contained an odd number of three Fe-layers, this system possessed a net magnetic moment corresponding to one Fe-layer.

A full relaxation calculation was performed on the $2 \times 2 \times 2$ [001] oriented STO supercell to find the relaxed bulk structure. For all other systems strained relaxation calculations were performed, where the **a** and **b** lattice parameters were fixed to the value corresponding to a relaxed STO cell with the $Pm\bar{3}m$ symmetry. The **c** lattice parameter and the ionic positions were allowed to relax during these calculations.

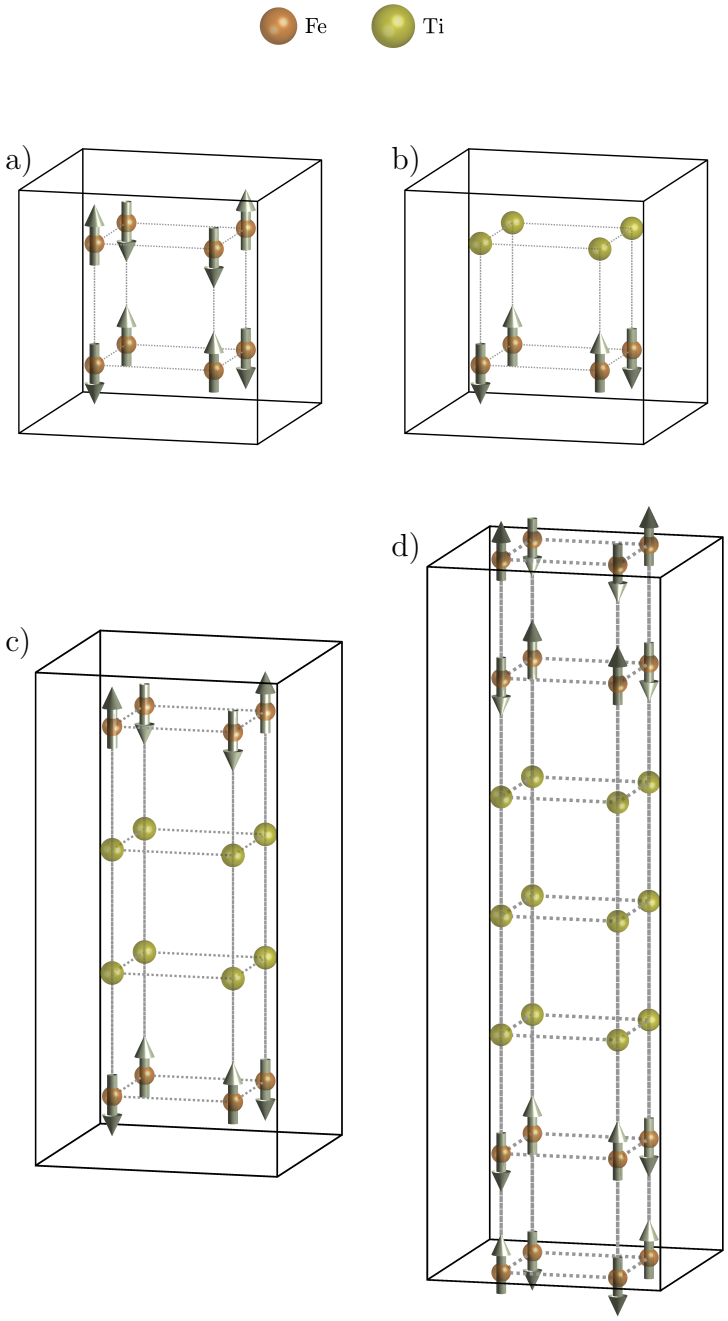

Figure 4.4: The magnetic ordering of the Fe ions for the [001] oriented LFO supercell (a), and the (1,1), (2,2), and (3,3) superlattices in b, c, and d, respectively. An up-pointing arrow indicate a magnetic moment pointing up, while a down-pointing arrow indicate a magnetic moment pointing down. The black lines represent the borders of the supercell and superlattices, and the grey dashed lines represents the network of nearest neighbour B cations. The A cations and O anions are excluded for clarity.

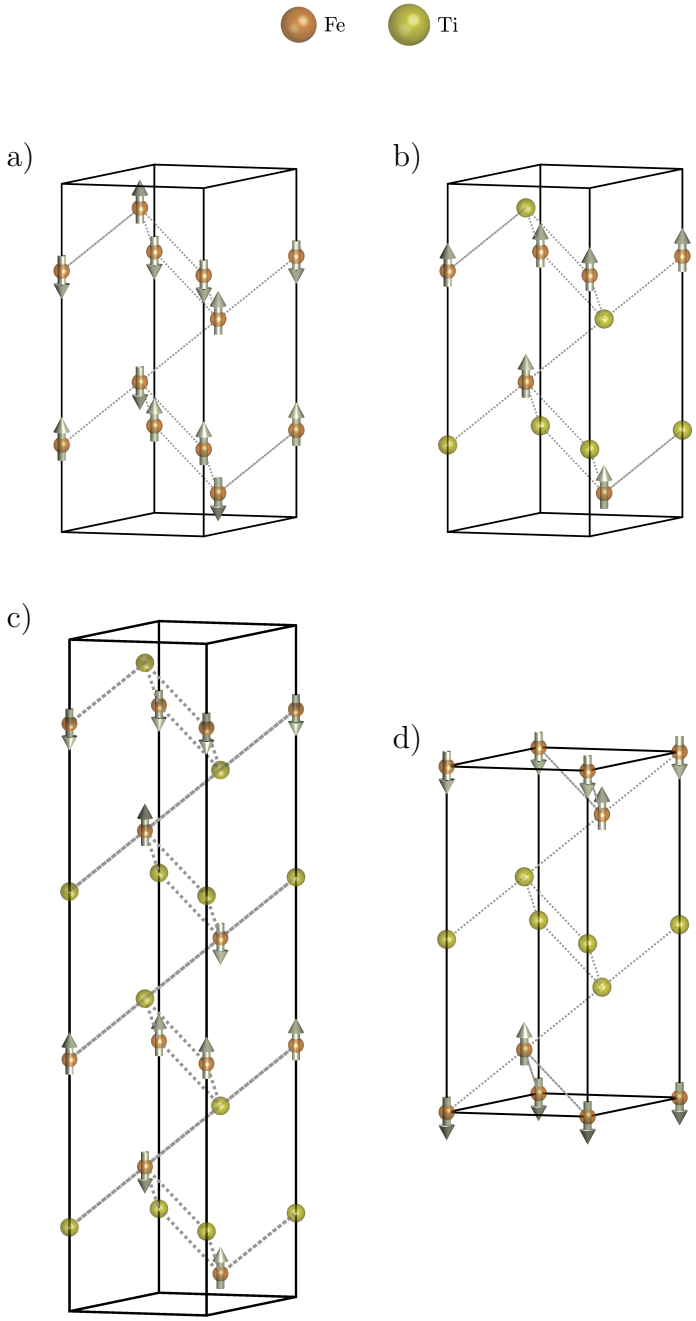

Figure 4.5: The magnetic ordering of the Fe ions for the [111] oriented LFO supercell (a), and the $(1,1)_{\mathrm{FM}}$, $(1,1)_{\mathrm{AF}}$, and (3,3) superlattices in b, c, and d, respectively. For clarity, a $\sqrt{2}\times\sqrt{2}\times 2\sqrt{3}$ LFO supercell is shown in a) instead of the $2\sqrt{2}\times 2\sqrt{2}\times 2\sqrt{3}$ supercell. An up-pointing arrow indicate a magnetic moment pointing up, while a down-pointing arrow indicate a magnetic moment pointing down. The black lines represent the borders of the supercell and superlattices, and the grey dashed lines represents the network of nearest neighbour B cations. The A cations and O anions are excluded for clarity.

Phonon modes and frequencies calculations

In order to obtain the phonon modes and frequencies for the relaxed and strained relaxed structures, the phonopy software was used. As this software finds the space group of the structure, and decides what kind of atomic displacements in the structure it will calculate based on this found space group, the atomic position accuracy in the phonopy software was also set to that corresponding to each structure. The atomic position accuracy for each relaxed structure was again checked in the FINDSYM program. The space groups to be recognized for the different relaxed supercells and superlattices are given in table 4.7.

Table 4.7: Space groups of the supercells and superlattices for the different orientations for the phonon modes and frequencies calculations.

	Orientation	
Supercell/superlattice	[001]	[111]
STO	$Pm\bar{3}m$	-
LFO	$P4/mmm$	$R\bar{3}m$
(1,1)	$P4mm$	$R3m$
(2,2)	$P4/mmm$	-
(3,3)	$P4/mmm$	$P\bar{3}m1$

As the [001] oriented structures already had dimensions that allowed for in-phase and out-of-phase rotational modes, the relaxed structures from the previous calculations were used in these calculations. In addition, the phonon modes and frequencies were found for a $(1,1)_2$ [001] oriented superlattice with dimensions $2 \times 2 \times 4$. This additional calculation for the (1,1) superlattice was performed to see if the small film layer thicknesses for this superlattice allowed adjacent same-material film layers to affect each other to such an extent that the phonon modes and phonon frequencies differed significantly between those for the $2 \times 2 \times 2$ and $2 \times 2 \times 4$ superlattice.

The $2 \times 2 \times 4$ (1,1) [001] oriented superlattice were constructed by doubling the relaxed (1,1) [001] oriented $2 \times 2 \times 2$ superlattice along the [001] direction. Hence, the magnetic ordering in the resulting additional FeO_2-layer was exactly the same as that for the other FeO_2-layer (showed in figure 4.4b).

As for the [001] oriented structures, the [111] oriented LFO $2\sqrt{2} \times 2\sqrt{2} \times 2\sqrt{3}$ supercell also had dimensions that allowed for both kinds of rotational modes. Hence, the relaxed supercell was used in the calculations to find the phonon modes and frequencies.

To obtain structures that allowed both kind of rotation modes about each pseudocubic rotation axis, the relaxed $(1,1)_{3,\mathrm{FM}}$, $(1,1)_{6,\mathrm{AF}}$, and (3,3) [111] oriented superlattices were doubled along the **a** and **b** lattice parameter directions

before the calculations to find the phonon modes and frequencies were performed on these structures. The (3,3) superlattice was also doubled along the **c** lattice parameter direction so that possible effects regarding adjacent same-material film layers affecting each other could be accounted for. The magnetic ordering in the resulting additional LFO film layer in the $(3,3)_2$ superlattice was exactly the same as that for the other LFO film layer (showed in figure 4.5d). Hence, the $(3,3)_2$ [111] oriented superlattice possessed a net magnetic moment corresponding to two Fe-layers.

As the structures were doubled along certain lattice parameter directions, the k point mesh size was changed accordingly (table 4.8).

Table 4.8: k point mesh size and mesh type – where MP=Monkhorst–Pack and G=Gamma – for the supercells and superlattices with different orientations for the phonon modes and frequencies calculations.

	Orientation and mesh type	
Supercell/superlattice	[001] and MP	[111] and G
STO	$4 \times 4 \times 4$	-
LFO	$4 \times 4 \times 4$	$3 \times 3 \times 2$
(1,1)*	$(4 \times 4 \times 4)_{(1,1)}$	$(3 \times 3 \times 2)_{(1,1)_{3,\mathrm{FM}}}$
	$(4 \times 4 \times 2)_{(1,1)_2}$	$(3 \times 3 \times 1)_{(1,1)_{6,\mathrm{AF}}}$
(2,2)	$4 \times 4 \times 2$	-
(3,3)*	$(4 \times 4 \times 1)_{(3,3)}$	$(3 \times 3 \times 1)_{(3,3)_2}$

4.3.3 Calculation of the vector magnitudes

The phonon modes for each structure were visualized to find which modes that corresponded to in-phase and out-of-phase rotation phonon modes and polar phonon modes. The frequencies of these phonon modes were noted. The displacement vectors corresponding to the rotation phonon modes were then found in an anime.ascii file, constructed by the phonopy software. As the rotation phonon modes correspond to displacements of the oxygen anions, only displacement vector magnitudes for the oxygen ions were regarded when plotting the average vector magnitude for each layer in the superlattices.

For the [001] oriented superlattices both the AO- and BO_2-layers contain oxygen ions. The average oxygen displacement vector magnitudes for the oxygen ions in each AO- and BO_2-layer were calculated in MATLAB. These calculated

*The subscripts for the (m,m) superlattices depict which superlattice this k point mesh corresponds to.

average values were plotted as layer numbers x (integer layers) for the BO_2-layers and $x.5$ (half-layers) for the AO-layers. For out-of-plane rotation phonon modes in [001] oriented systems, the oxygen ions in the AO-layers do not move. Hence, only integer layer numbers (corresponding to BO_2-layers) were plotted for these phonon modes. The oxygen displacement vector magnitudes were also found for the STO and LFO supercells for each rotation phonon mode. These values were included in the plots for the superlattices as an indication of the corresponding displacements in the bulk materials.

In the [111] oriented superlattices all oxygen anions are in the AO_3 layers, corresponding to half-layers ($x.5$). The average oxygen displacement for each AO_3 layer was calculated in MATLAB and plotted as layer numbers $x.5$.

4.3.4 Frozen-in phonon modes calculations

In search of the ground state structure, several combinations of the phonon modes were frozen in in the (3,3) [001] oriented superlattice and the $(3,3)_2$ [111] oriented superlattice. By freezing in combinations of different phonon modes, the oxygen positions were initialized such that a tilt pattern dissimilar from that of the highly symmetric structure were obtained in the film layers.

Which phonon modes to freeze in were determined based on the phonon mode frequency – where the phonon modes with the largest imaginary frequencies were assumed to correspond to the most probable oxygen distortions in the ground state structure, – and the known bulk tilt patterns of LFO and STO.

The oxygen displacement vectors had different magnitudes for the different layers in the superlattices – that is, one phonon mode could correspond to large oxygen displacements in the LFO layers, while the oxygen anions in the STO layers remained almost undistorted from the highly symmetric structure. Therefore, the initial trial structures tried out for these calculations are given by the tilt pattern of the LFO film layers and the average rotation and tilt angles in the middle LFO layer in the LFO film (the most distorted layer).

These initial trial structures were then strained relaxed, where the **a** and **b** lattice parameters were fixed while the **c** lattice parameter and the ionic positions in the structure were allowed to relax.

Initial trial structures for the (3,3) [001] oriented superlattice

Several initial trial structures were constructed for the (3,3) [001] oriented superlattice. Tilt patterns in the LFO film layers corresponding to the bulk LFO tilt pattern – that is, both the $a^-a^-c^+$ and $a^+a^-c^-$ tilt pattern, – with different distributions of in-plane and out-of-plane rotation magnitudes were tried, as well as some tilt patterns not found in bulk LFO. All initial trial structures for this superlattice are listed in table 4.9.

Table 4.9: The tilt pattern in the LFO film layers and the average rotation and tilt angle magnitudes (mag.) in the middle LFO layer in each of the initial trial structures for the (3,3) [001] superlattice.

Tilt pattern	α	β	γ	θ_x	θ_y	θ_z	Note
$a^-a^-c^+$	7.2	7.2	8.1	158.2	158.2	160.4	Different distribution of in-plane and out-of-plane rotation mag.
	5.8	5.8	11.3	154.6	154.6	164.3	
	4.4	4.4	12.9	152.9	152.9	168.2	
$\sim a^+a^-c^-$	7.1	7.2	8.5	157.5	157.6	160.6	Different distribution of in-plane and out-of-plane rotation mag.
	5.7	5.8	11.8	153.6	153.7	164.4	
	4.3	4.4	13.5	151.7	151.7	168.3	
$\sim a^+a^-c^-$	5.0	5.1	6.0	164.1	164.2	166.4	Different total rotation magnitude
	9.9	10.1	11.8	148.9	149.0	153.1	
$a^+b^-c^-$	4.3	8.7	10.2	153.2	157.8	161.5	
$a^0a^0c^-$	0	0	15.1	149.8	149.8	180	
$a^-a^-c^-$	7.2	7.2	8.5	157.6	157.6	160.4	

Initial trial structures for the $(3,3)_2$ [111] oriented superlattice

A number of different initial trial structures were also constructed for the $(3,3)_2$ [111] oriented superlattice. The tilt pattern in the LFO film layers in these structures are listed in table 4.10 together with the rotation and tilt angles in the middle of the LFO film layers.

Table 4.10: The tilt pattern in the LFO film layers and the average rotation and tilt angle magnitudes in the middle LFO layer in each of the initial trial structures for the $(3,3)_2$ [111] superlattice.

Tilt pattern	α	β	γ	θ_x	θ_y	θ_z
$a^-a^-a^-$	8.1	8.1	8.1	157.4	157.4	157.4
$\sim a^-b^-c^0$	7.6	10.9	1.6	158.3	164.5	154.0
$\sim a^0b^-a^0$	0.5	13.3	0.5	153.7	178.9	153.5
$a^-b^-c^+$	7.2	5.3	9.5	158.3	156.5	162.1

4.4 Structure calculations

In the second calculation method utilized in this master thesis – the structure calculations, – the superlattices were build in MATLAB. As opposed to the phonon mode calculations, the building blocks for the structures constructed for these calculations were not highly symmetric for both materials, but rather corresponded to that of relaxed STO cells – with $Pm\bar{3}m$ symmetry – and strain relaxed LFO cells – with $Pnma$ symmetry. Hence, the film layers in the initial trial structures had tilt patterns corresponding to that found in the bulk film materials, assuming that these tilt patterns would also be present in the film layers. After these structures were build, all ionic positions – except for those in the middle layers of STO – were allowed to relax. As the ionic positions in the middle STO layers were fixed, the STO film layer modelled a thick STO film layer even though the number of functional units in this layer was small. When the ionic positions in the remaining free layers in the superlattices had relaxed to equilibrium positions, the rotation and tilt angle magnitudes for the resulting structures were calculated in MATLAB.

Section 4.4.1 covers the construction of these superlattices, while section 4.4.2 describes the DFT calculation procure for the structure calculations. In section 4.4.3 the calculations of the rotation and tilt angles are explained.

The dimensions of the [001] and [111] oriented superlattices for which structure calculations were performed are listed in tables 4.11 and 4.12, respectively. The film layer thicknesses m and n for these superlattices were varied asymmetrically ($m \neq n$), and are expressed as (m,n). As the tilt pattern for bulk LFO is $a^-a^-c^+$, for the [001] oriented superlattices the in-phase rotations could either lie about the out-of-plane direction ([001]) – resulting in an $a^-a^-c^+$ tilt pattern – or about one of the two in-plane directions ([100] or [010]) – resulting in an $a^+b^-b^-$ or $a^-b^+a^-$, respectively, – which would be symmetry unequivalent structures. Therefore, structures with in-phase rotations about both the out-of-plane axis and the in-plane pseudocubic [010] axis were constructed. For the [111] oriented superlattices, however, the three pseudocubic rotational axes ([100], [010], and [001]) are symmetry equivalent, and only one tilt pattern was therefore imposed in the LFO layers for these superlattices.

Table 4.11: An overview of the [001] oriented systems for which structure calculations were performed in this master thesis.

(m,n)	$a^-a^-c^+$	$a^-b^+a^-$
(2,3)	$\sqrt{2} \times \sqrt{2} \times 5$	$2 \times 2 \times 5$
(6,3)	$\sqrt{2} \times \sqrt{2} \times 9$	$2 \times 2 \times 9$

Table 4.12: An overview of the [111] oriented systems for which structure calculations were performed in this master thesis.

(m,n)	$a^-a^-c^+$
(4,5)	$\sqrt{2} \times \sqrt{6} \times 3\sqrt{3}$
(10,5)	$\sqrt{2} \times \sqrt{6} \times 5\sqrt{3}$

4.4.1 Lattice construction

In the construction of the superlattices three different STO cells and three different LFO cells were used as building blocks (figure 4.6). The three different cells for each material corresponded to two different in-plane dimensions for the [001] oriented systems and one [111] oriented cell. To make the calculations as little computationally expensive as possible, the in-plane dimensions were set to the smallest possible values while still allowing for the rotations and tilts corresponding to the LFO bulk structure. For the [001] oriented systems the smallest possible in-plane dimensions when the in-phase rotations in LFO lies about the out-of-plane direction are $\sqrt{2} \times \sqrt{2}$, while in-plane dimensions of 2×2 are necessary when the in-phase rotations lies about one of the in-plane rotation axes. The smallest possible in-plane dimensions for an [111] oriented cell of a perovskite with tilt pattern $a^-a^-c^+$ (as bulk LFO) are $\sqrt{2} \times \sqrt{6}$.

The STO building bock cells were obtained from a fully relaxed STO unit cell. This STO unit cell was obtained from a calculation in the pre-project with model parameters given in table 4.2. To obtain an STO cell with in-plane dimensions $\sqrt{2} \times \sqrt{2}$ – to be used as the STO building block in the superlattices with in-phase rotations (in LFO) about the out-of-plane direction – the unit cell was rotated by the rotation matrix

$$R = \begin{bmatrix} 1 & 1 & 0 \\ \bar{1} & 1 & 0 \\ 0 & 0 & 1 \end{bmatrix}. \tag{4.1}$$

To obtain an STO cell with in-plane dimensions 2×2, the STO unit cell was doubled along the the **a** and **b** lattice parameters. The third STO building block cell – used in the [111] oriented superlattices – was obtained by rotating the STO unit cell by the rotation matrix

$$R = \begin{bmatrix} 1 & 1 & 1 \\ \bar{1} & 1 & 1 \\ 0 & \bar{2} & 1 \end{bmatrix}, \tag{4.2}$$

resulting in an STO cell with **a**, **b**, and **c** lattice parameters lying along the pseudocubic $[1\bar{1}0]$, $[11\bar{2}]$, and [111] directions, respectively.

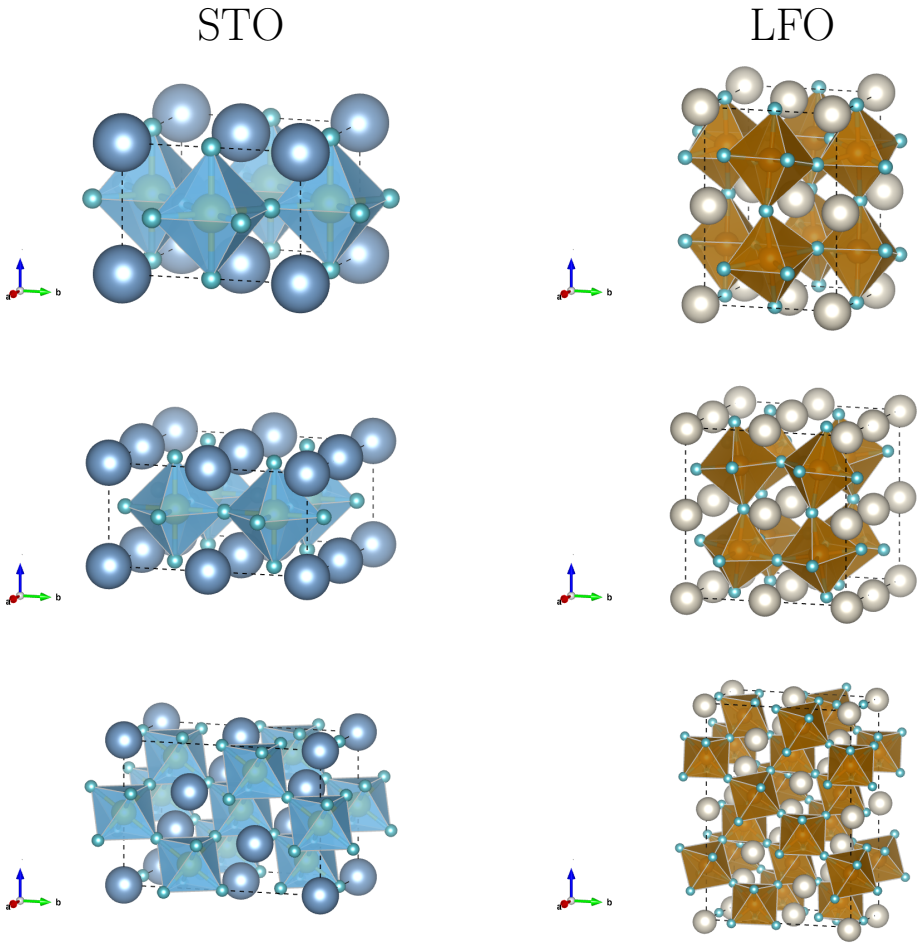

Figure 4.6: The building block cells used in the construction of the LFO_m/STO_n superlattices in the structure calculations. Building block cells for [001] oriented superlattices with in-phase rotations (in LFO) about the out of plane axis are shown in the top figures. The middle figures shows the building blocks in the [001] oriented supercells with in-phase rotations about the in-plane pseudocubic [010] axis, and the bottom figures show the building blocks for the [111] oriented superlattices. Figures made in VESTA [14].

For the LFO building block cells, the two [001] oriented LFO cells – one with in-phase rotations about the out-of-plane direction, and the second with in-phase rotations about the in-plane [010] direction – were obtained in calculations in the pre-project, where the **c** lattice parameter and the ionic positions had been allowed to relax. For the [111] oriented LFO building block cell a fully relaxed [001] oriented LFO cell with the *Pnma* symmetry, obtained in the pre-project, was rotated such that the **c** lattice parameter lay along the pseudocubic [111] direction, and the in-plane **a** and **b** lattice parameters along the pseudocubic $[1\bar{1}0]$ and $[11\bar{2}]$, respectively, resulting in in-plane dimensions $\sqrt{2} \times \sqrt{6}$. The **c**

lattice parameter and the ionic positions in this cell were allowed to relax, while keeping the **a** and **b** lattice parameter fixed to the values corresponding to the [111] oriented STO building block cell. The resulting cell structure was used as the [111] oriented LFO building block.

These six building blocks were used to build the superlattices by adding the desired number of STO and LFO building block cells on top of each other. This building was implemented in MATLAB. The STO film layer was chosen to contain three functional units along the out-of-plane axis for all [001] oriented superlattices, as this allowed for fixed positions of the ions in one STO layer, while the ions in the STO layers in proximity to the LFO film layer could be allowed to relax. In the [111] oriented superlattices a number of five functional units of STO along the out-of-plane axis was necessary to correspond to the three functional units in the [001] orientation, corresponding to 11.25 Å and 11.69Å, respectively. The ion positions in the three middle STO layers were fixed for the [111] oriented superlattice, while the ion positions in the STO layers in proximity to the LFO film were allowed to relax. The [001] oriented (2,3) superlattices and the [111] oriented (4,5) superlattice is shown in figure 4.7, where the STO layers with fixed ion positions are marked with yellow.

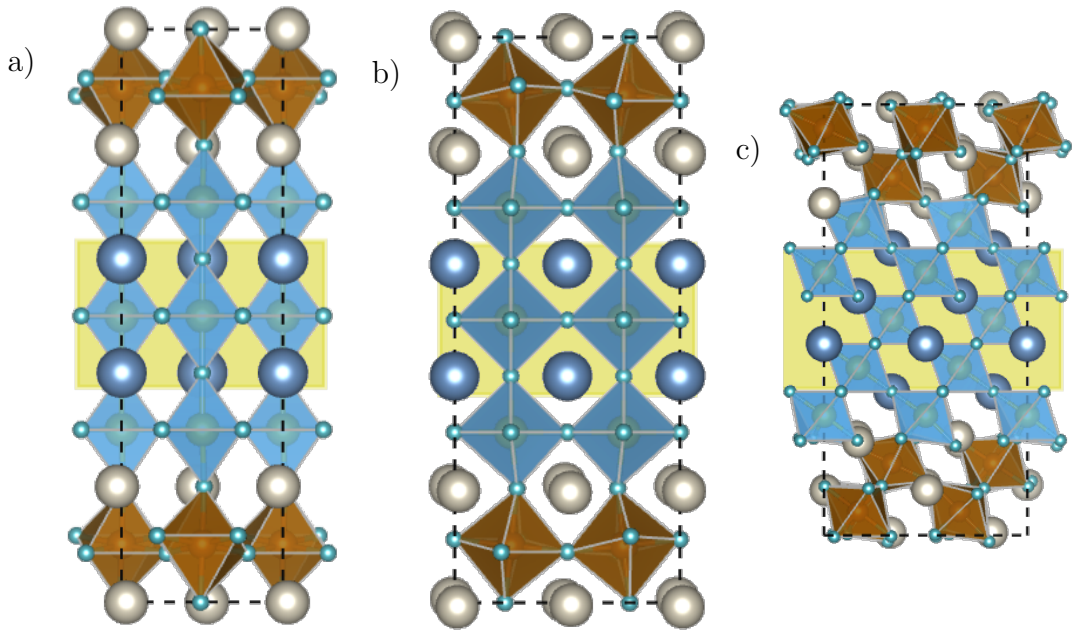

Figure 4.7: The superlattices constructed for the structure calculations of a (a) (2,3) [001] oriented superlattice with in-phase rotations in LFO about the out-of-plane direction, (b) (2,3) [001] oriented superlattice with in-phase rotations in LFO about the in-plane [010] direction, and (c) (4,5) [111] oriented superlattice. The yellow regions mark the ions that were locked to their bulk positions. Figure made in VESTA [14].

All superlattices were build such that the STO film layer was positioned in the middle of the superlattice, and the [001] ([111]) oriented superlattices were TiO_2 (Ti) terminated to impose a symmetry element along the **c** lattice parameter.

When the ionic positions in the [001] oriented (2,3) and [111] oriented (4,5) superlattices had relaxed to their equilibrium positions, the resulting structures were used in the building of the [001] oriented (6,3) and [111] oriented (10,5) superlattices, respectively. This was done because the relaxed ionic positions at the interface between LFO and STO in these superlattices were assumed to be closer to the equilibrium positions in superlattices with thicker LFO film layers than that of the positions corresponding the the bulk structures of the building blocks. Hence, the additional LFO layers in the [001] oriented (6,3) and [111] oriented (10,5) superlattices were added to the resulting structures from the structure calculations of the smaller superlattices.

4.4.2 DFT calculations

In order to obtain the rotations and tilts corresponding to the relaxed superlattices, the ionic positions in the free layers in the superlattices were relaxed while all three lattice parameters were kept fixed. By fixing the lattice parameters the structure would not relax by changing the B-O bond length, and the effect of the interface and superlattice periodicity on octahedral rotations alone could be detected. By using selective dynamics [40] in VASP the ionic positions in the middle STO layer in the [001] oriented superlattices and the three middle STO layers in the [111] oriented superlattices were fixed (figure 4.7).

The model parameter values given in table 4.2 were used in these calculations, except for that of the break condition for the ionic relaxation loop. This value was set to -5×10^{-3}. This was assumed to be an appropriate value for well converged structures of these sizes.

4.4.3 Calculation of rotation and tilt angle magnitudes

The resulting rotation (α, β, γ) and tilt (θ_x, θ_y, θ_z) magnitudes in the ionic relaxed structures were calculated in MATLAB. The tilt magnitudes were calculated by finding the B-O-B bond angles along one specific pseudocubic axis for each layer in the superlattice, and averaging these angles. Figure 4.8 illustrates this for θ_z in a [001] oriented lattice with in-plane dimensions 2×2.

The rotation magnitudes were calculated by following five steps. For the rotation angle x – where x can be either α, β, or γ, – these steps were:

1. Find the vectors pointing from the B cation to the four oxygen anions that do not lie along the rotation axis of x.

2. Project these vectors onto the plane orthogonal to the rotation axis of x.

3. Calculate the angle between the projected vectors and the vectors corresponding to no rotation – that is, the two rotation axes perpendicular to the rotation axis of x.

4. Average these four angles to find the rotation magnitude of x for this octahedra.

5. Repeat step one to four for all octahedra in the current layer. To find the rotation magnitude of x for this layer these rotation magnitudes were averaged.

Figure 4.9 illustrate step one to four for the rotation magnitude of γ.

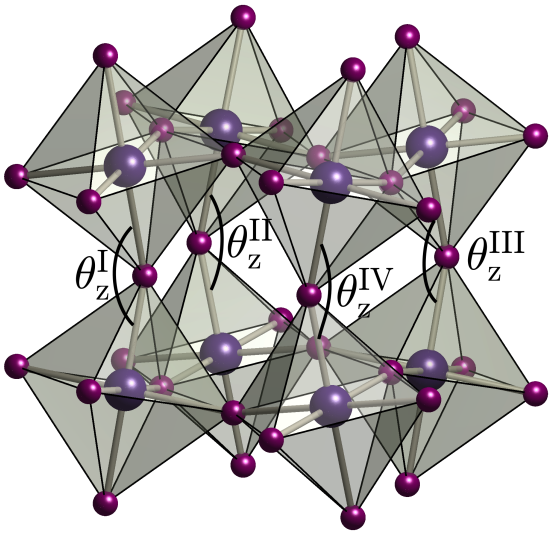

$$\theta_z = \frac{\theta_z^{I} + \theta_z^{II} + \theta_z^{III} + \theta_z^{IV}}{4}$$

Figure 4.8: The calculation of the tilt magnitudes, illustrated for the θ_z tilt angle between two layers in a [001] oriented superlattice with in-plane dimensions 2×2.

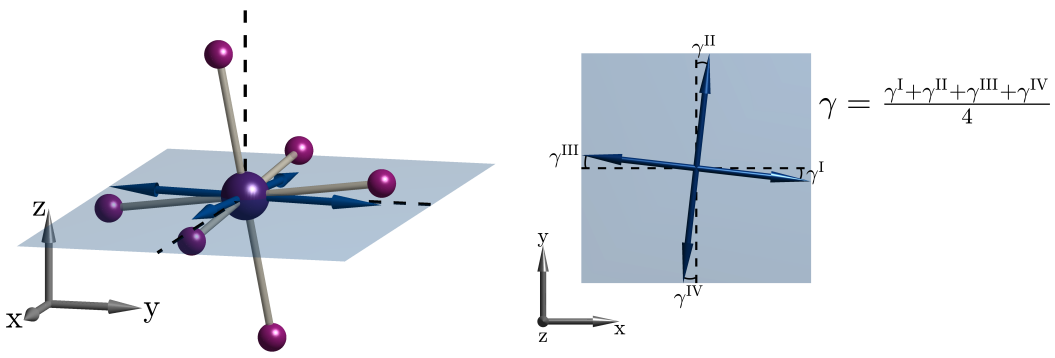

Figure 4.9: The calculation of the rotation magnitudes, illustrated for the γ rotation magnitude for one octahedron. In the left figure the BO_6 structure is shown together with the plane orthogonal to the γ rotation axis. The projected B-O vectors are shown in blue. The right figure is a top view of the same plane with the projected vectors and dotted lines indicating the pseudocubic [100] and [010] axes.

These average tilt and rotation magnitudes for each layer were plotted with their corresponding layer number in MATLAB, to illustrate the structure of the ionic relaxed structures.

4.5 Overview of approach

In table 4.13 an overview of all systems that were investigated during this master thesis in order to elucidate how octahedral rotations in superlattices are affected by different film layer thicknesses and system orientations, are given.

Table 4.13: An overview of the systems investigated in this master thesis.

	Phonon mode calculations		Structure calculations	
	[001]	[111]	[001]	[111]
(1,1)	✓	✓	-	-
(2,2)	✓	-	-	-
(3,3)	✓	✓	-	-
(2,3)	-	-	✓	-
(6,3)	-	-	✓	-
(4,5)	-	-	-	✓
(10,5)	-	-	-	✓

Chapter 5

Results and discussion

In this chapter the results from the calculations described in the previous chapter are presented together with a discussion of what these results might indicate. The first and second part of the chapter covers the results from the phonon mode calculations, where the phonon modes and phonon mode frequencies found for each structure is given in section 5.1 and the results from the frozen-in phonon mode calculations are given in section 5.2. The third part gives the results from the structure calculations (section 5.3), and in the final part a discussion attempting to look at how the results from these different kind of calculations correlate (or do not correlate) is presented (section 5.4).

5.1 Phonon modes in symmetric LFO_m/STO_m superlattices

This section first covers the results obtained from the phonon mode calculations calculating the phonon frequencies and phonon modes in the [001] oriented superlattices (section 5.1.1), followed by the results obtained from the [111] oriented superlattices (section 5.1.2). After these results are presented and discussed a comparison of the results obtained from these different orientations is given in section 5.1.3.

The phonon modes considered in this master thesis were in-phase rotation modes, out-of-phase rotation modes, and polar modes, written as Rot^{+}, Rot^{-}, and P, respectively. In addition it was distinguished between displacements about the out-of-plane axis and in-plane axes, written as subscripts to the corresponding phonon mode as $\perp$ and $\parallel$, respectively. Generally, the displacements corresponding to the different phonon modes were larger in one of the two film materials than the other. Hence, for some of the superlattices it was found two phonon modes corresponding to the same type of displacements, but in one of the modes the majority of the displacements were found in the film layer with the first material, while in the other phonon mode the majority of the displacements were in the film

layer with the second material. For example, two out-of-phase rotation modes about the out-of-plane axis ($Rot^{-}_{\perp}$) could be found in the same superlattice, one where the majority of the displacements were within the LFO film layer ($Rot^{-}_{\perp}$ LFO), and one where most of the displacements were within the STO layer ($Rot^{-}_{\perp}$ STO).

5.1.1 [001] oriented superlattices

The phonon mode frequencies found for the [001] oriented LFO and STO supercells and the $(1,1)_2$, (2,2), and (3,3) superlattices are shown in figure 5.1. The results obtained from the $(1,1)_2$ superlattice were chosen to represent the finding for this periodicity instead of the (1,1) superlattice. This decision was made based on the fact that the $(1,1)_2$ superlattice also allowed adjacent same-material film layers to possibly effect each other such that the phonon displacements in one layer was different from the next layer of the same material. Hence, this superlattice contained more – and therefore, presumably, more correct – information. That being said, it was not found a considerate difference in the phonon mode frequencies found for the (1,1) and $(1,1)_2$ superlattices.

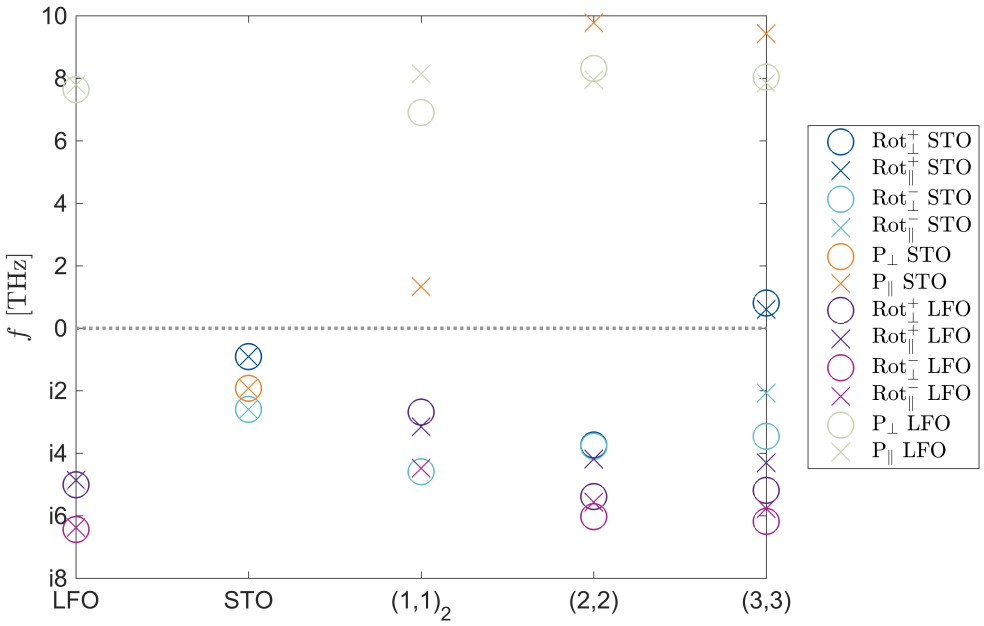

Figure 5.1: Phonon mode frequencies (f) for LFO, STO, and the $(1,1)_2$-, (2,2)-, and (3,3)-superlattices.

Looking at the phonon mode frequencies found for the rotation modes in the LFO supercell one can see that the largest imaginary phonon mode frequencies – and

hence the most favorable displacements in the structure – were that of the out-of-phase rotation phonon modes (Rot^- LFO). This coincide well with the known tilt pattern in bulk LFO, namely $a^-a^-c^+$, with out-of-phase rotations about two pseudocubic rotation axes. The in-phase rotation modes in this supercell was also imaginary but with a slightly smaller imaginary frequency. Nevertheless, in bulk LFO one of these phonon modes are frozen in, favoring in-phase rotations about one pseudocubic rotation axis, rather than out-of-phase rotations about all three rotation axes.

The out-of-plane rotation modes ($\mathrm{Rot}^-{}_\perp$ and $\mathrm{Rot}^+{}_\perp$) in the LFO supercell was found to have larger imaginary frequencies than their corresponding in-plane rotation modes. For the Rot^- phonon modes the difference in frequency between in-plane and out-of-plane rotation modes were found to be $\sim$ 57 GHz, while a difference of $\sim$ 144 GHz was found for the Rot^+ modes. This difference between in-plane and out-of-plane Rot^- modes indicate that when LFO is strained to STO in the (001) plane, the rotations about the out-of-plane axis is more likely to be out-of-phase than in-phase. This coincide well with experimental results of LFO films grown on STO substrates [30], where the rotational mismatch in the LFO film were oriented such that the in-phase rotations lay about one of the in-plane axes, and hence, the rotations about the out-of-plane direction was out-of-phase.

The polar phonon modes in the LFO supercell had large real frequencies. This was as expected as the bulk structure of LFO do not possess such displacements.

For the STO supercell all rotation modes and polar modes were found to have imaginary frequencies, indicating that the $Pm\bar{3}m$ symmetry is not stable in STO. When calculating the energies and finding the crystal structures by performing DFT calculations, the results are that for a system at 0 K. At 0 K the tetragonal phase of STO is stable with an $a^0a^0c^-$ tilt pattern. This explains the imaginary frequency of the Rot^- modes, corresponding to the phonon mode with the largest imaginary frequency value for this supercell.

The imaginary frequencies for the polar phonon modes are explained by the fact that STO is an incipient ferroelectric [49], meaning that a ferroelectric transition in the material is suppressed by quantum fluctuations.

For the STO supercell there was no difference in frequency between the in-plane and out-of-plane displacements for the same type of phonon mode, indicating symmetry equivalent displacements about all pseudocubic axes. This was as expected as this supercell was cubic and fully relaxed rather than strain relaxed.

When comparing the phonon mode frequencies found for the (m,m) superlattices with those found for the pure LFO and STO systems, one can see that the largest imaginary phonon mode frequencies corresponds to LFO phonon modes (the majority of the displacements corresponding to the phonon modes are within the LFO layers). This implies that it is more favorable for the superlattices to prioritize displacements that is favorable for the LFO layers. One can with this say that the LFO layers dominate the STO layers regarding determination of ground state structure. This effect becomes more apparent as the layer thicknesses (m)

increase.

The results for the superlattices will now be covered, one phonon mode at a time. The main focus will be on the rotation phonon modes, as these were the phonon modes with the imaginary phonon mode frequencies. The polar phonon modes had in general large real frequencies for the superlattices. Hence, these phonon modes were considered less important when looking at how superlattice periodicity can affect the structure in the different film layers. Figure 5.2 shows only the imaginary and lowest real phonon mode frequencies showed in figure 5.1, excluding the large real frequency polar phonon modes, for clarity.

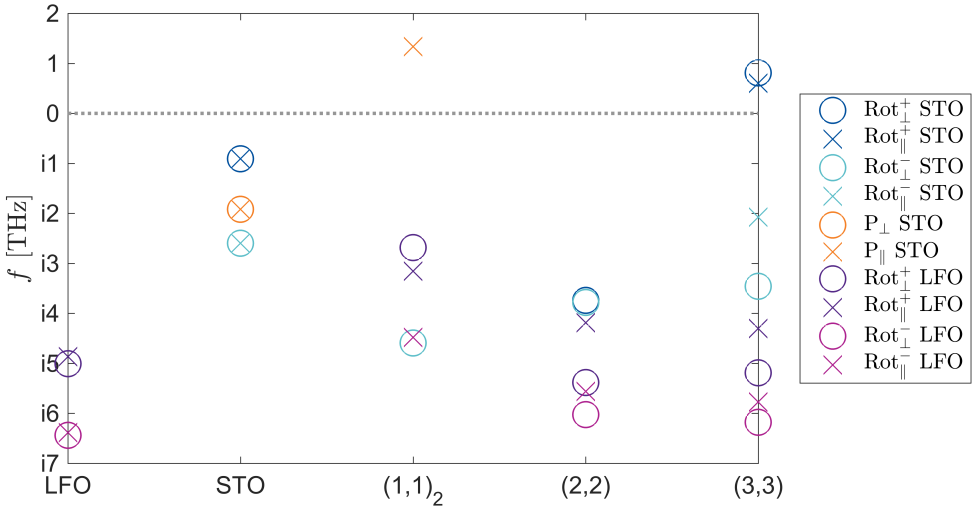

Figure 5.2: Phonon mode frequencies, f (for $f < 2$ THz), for LFO, STO, and the $(1,1)_2$-, (2,2)-, and (3,3)-superlattices.

The Rot$^-_\perp$ phonon modes

In figure 5.2 one can see that the largest imaginary phonon mode frequencies for all [001] oriented superlattices corresponded to out-of-phase rotations about the out-of-plane axis (pink and cyan circles). This indicate that these kind of distortions are favorable in superlattices of LFO and STO.

In the $(1,1)_2$ superlattice, only one Rot$^-_\perp$ phonon mode was found. The majority of the displacements corresponding to this phonon mode was in the STO film layers (figure 5.3a and table 5.1), where the displacement vector magnitude almost reached that found for the corresponding rotation mode in the STO supercell (bulk). The frequency of this phonon mode had a larger imaginary value than that found for the STO supercell, indicating that such displacements were more favorable in STO film layers in a (1,1) superlattice with LFO than it was for bulk STO.

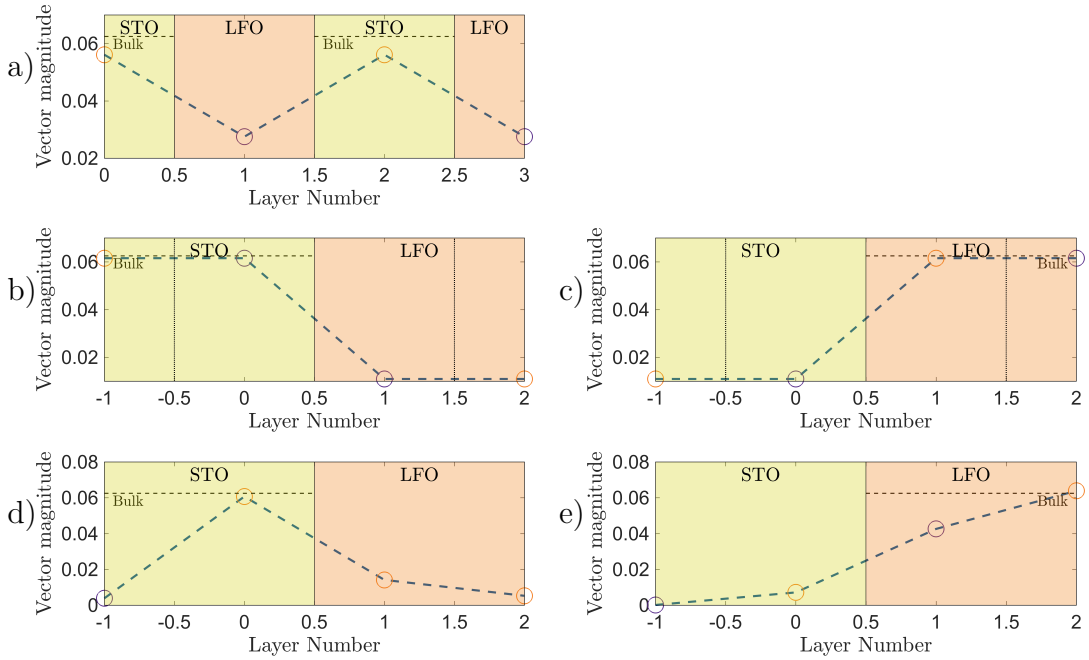

Figure 5.3: Out-of-phase rotation modes about the out-of-plane direction ($Rot^{-}_{\perp}$) in STO (left column) and LFO (right column). a) illustrate the displacement distribution in the $(1,1)_2$ superlattice, while b) and c) illustrate that for the (2,2) superlattice. d) and e) shows the distribution in the (3,3) superlattice. Different colors on the circular plot makers indicate different rotation directions (clockwise or counterclockwise).

Table 5.1: Displacement distributions for out-of-phase rotations about the out-of-plane direction ($Rot^{-}_{\perp}$) for the [001] oriented superlattices.

	STO modes		LFO modes	
Superlattice	STO	LFO	LFO	STO
$(1,1)_2$	67.1%	32.9%	-	-
(2,2)	84.9%	15.1%	84.9%	15.1%
(3,3)	77.0%	23.0%	93.7%	6.3%

For the (2,2) and (3,3) superlattices it was found two phonon modes corresponding to out-of-phase rotations about the out-of-plane axis, one where the majority of the displacements were within the STO film layers, and one where the majority of displacements were in the LFO layers. The latter phonon mode was the phonon mode corresponding to the largest imaginary frequency value, for both superlattices (pink circle in figure 5.2). As for the $(1,1)_2$ superlattice, the $Rot^{-}_{\perp}$ STO

phonon mode in the (2,2) and (3,3) superlattices had still larger imaginary frequency values than that found for the bulk STO supercell. Hence, in superlattices with larger periodicity than one ($m > 1$), it seems like displacements favorable for bulk LFO are the most probable displacements in the superlattices. Nevertheless, $\mathrm{Rot}^{-}{}_{\perp}$ phonon modes are still more favorable in the STO film layers than what they are for bulk STO.

When comparing the distribution of displacements in the different film layers for these rotation modes (figure 5.3 and table 5.1), one can see that as the periodicity, m, increases the displacements corresponding to these phonon modes are more defined within one of the two film materials. By looking at the average displacement vector magnitude for each layer in the superlattices in figure 5.3 one can also see the the displacement vector magnitude found in the STO (LFO) film layers in the $\mathrm{Rot}^{-}{}_{\perp}$ STO (LFO) phonon modes reach that of the bulk supercell for superlattices with $m > 1$. Even though the vector magnitude for the $\mathrm{Rot}^{-}{}_{\perp}$ STO phonon mode reach that of bulk STO in the STO film layers in the (2,2) superlattice (figure 5.3b), the displacements in the LFO film layers do not reach zero. The same is observed for the $\mathrm{Rot}^{-}{}_{\perp}$ LFO phonon mode (figure 5.3c), where the vector magnitude reach that of bulk LFO in the LFO film layers, but the vector magnitude in the STO film layers does not reach zero. This implies that the octahedral proximity effect is too strong at the interface between LFO and STO for the displacements in the fist interface layers to become zero.

Figures 5.3d and 5.3e shows that a periodicity of three is sufficient for the displacements to reach that of the bulk material for one film material, while the layers away from the interface in the other material can possess no displacements. This indicated that the penetration length of rotations corresponding to the $\mathrm{Rot}^{-}{}_{\perp}$ phonon mode was about one and a half layer for the [001] oriented superlattices.

Note that there is a rotational phase mismatch at the interface in the (2,2) superlattice for the $\mathrm{Rot}^{-}{}_{\perp}$ STO phonon mode (figure 5.3b). This can be seen by looking at the colors of the circular plot markers in in this figure, where the colors are different – illustrating out-of-phase rotations – within each film layer, but the rotation directions are the same in the two layers on both sides of the interfaces (same circular marker color), indicating in-phase rotations for these layers. Hence, the out-of-plane rotations are ordered as ↺ ↻ ↻ ↺, where the two first layers are STO layers, and the latter two layers are LFO layers, as illustrated in figure 5.4.

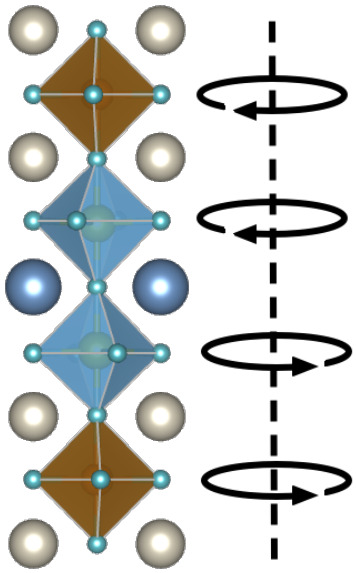

Figure 5.4: The rotations about the out-of-plane axis corresponding to the $Rot^-_\perp$ STO phonon mode in the (2,2) superlattice. Figure made in VESTA [14].

The $Rot^-_\parallel$ phonon modes

Now over to the second largest imaginary phonon mode frequencies found in the [001] oriented superlattices – those corresponding to out-of-phase rotations about the in-plane axes (pink and cyan crosses). Figure 5.5 shows the distribution of displacement in each layer in the superlattices, and table 5.2 gives the displacement distribution for all $Rot^-_\parallel$ phonon modes found in the superlattices.

In figure 5.5a one can see that the displacements corresponding to the $Rot^-_\parallel$ phonon mode were almost evenly distributed between the STO and LFO film layers in the $(1,1)_2$ superlattice, with 51.1% of the total displacements withing the LFO film layers and 48.9% within the STO film layers (table 5.2). This implies that the $Rot^-_\parallel$ phonon mode coupled strongly over the interface. This was as expected as in-plane rotations correspond to displacements of oxygen anions that are shared between the two film materials at the interface. Hence, displacements corresponding to the $Rot^-_\parallel$ phonon mode in one layer must induce displacements in the neighbouring layer for the octahedral network to stay corner connected. Nevertheless, the presence of STO film layers seemed to damp the displacements in the LFO film layers, as the displacement vector magnitudes did not reach that found in the bulk LFO supercell in the middle LFO layers.

This damping was also apparent in the superlattices with higher periodicity, as none of the $Rot^-_\parallel$ phonon modes in any of the superlattices showed to have displacement vectors with the same magnitude as that found in the STO and LFO supercells (figure 5.5). From the displacement distributions given in table 5.2 one can see that, for the $Rot^-_\parallel$ LFO phonon modes, as the periodicity increases more

of the displacements are within the LFO layers. This indicate that the damping from the STO layers had a smaller effect when the film layer thicknesses increased. As the displacement vector magnitudes almost reach that of the bulk material in the LFO film layers in the (2,2) and (3,3) superlattices, one can assume that a slightly thicker LFO film layer of four LFO unit cells would be sufficient to reach the displacement magnitude found in the LFO supercell.

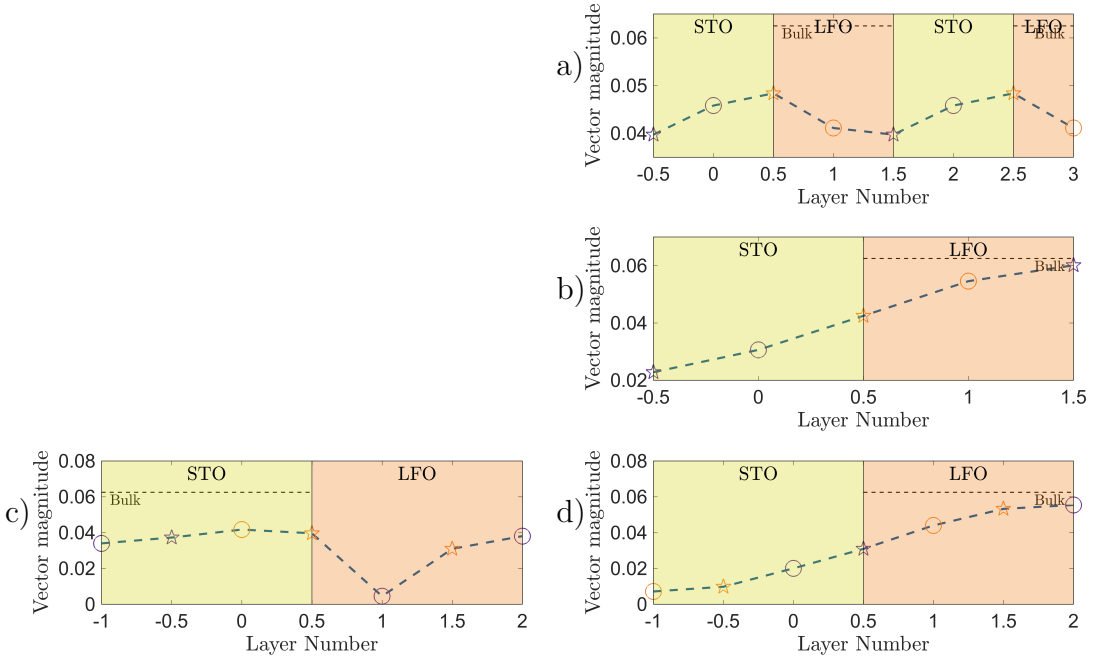

Figure 5.5: Out-of-phase rotation modes about the in-plane directions ($\text{Rot}^-_{\parallel}$) in STO (left column) and LFO (right column). a) illustrate the displacement distribution in the $(1,1)_2$ superlattice, while b) illustrate that for the (2,2) superlattice. c) and d) shows the distribution in the (3,3) superlattice. Different colors on the circular plot makers indicate different rotation directions (clockwise or counterclockwise).

Table 5.2: Displacement distributions for out-of-phase rotations about the in-plane directions ($\text{Rot}^-_{\parallel}$) for the [001] oriented superlattices.

	STO modes		LFO modes	
Superlattice	STO	LFO	LFO	STO
$(1,1)_2$	-	-	51.1%	48.9%
(2,2)	-	-	68.2%	31.8%
(3,3)	60.6%	39.4%	80.5%	19.5%

In figure 5.5 one can also see that the displacements did not reach zero in any layer for none of the $Rot^{-}_{\parallel}$ phonon modes found for the superlattices. This implies that the octahedral proximity effect regarding displacements corresponding to the $Rot^{-}_{\parallel}$ phonon mode had a penetration length larger than one and a half layer in the [001] oriented superlattices. In the STO layer away form the interface in the (3,3) superlattice, the displacements corresponding to the $Rot^{-}_{\parallel}$ LFO phonon mode (figure 5.5d) almost reached zero. Therefore, one can assume that in a superlattice with film layer thicknesses of one extra unit cell, the middle STO layers would have zero displacements.

Looking at the average displacement vector magnitudes, corresponding to the $Rot^{-}_{\parallel}$ STO phonon mode, for each layer in the (3,3) superlattice (figure 5.5c), one can see a sudden decrease in the displacement vector magnitude in the first interface layer of LFO. In the LFO layer away from the interface, however, the displacements increased. This is assumed to be caused by a rotation phase mismatch at the interface. In the STO film layer the displacements corresponded to that of the $Rot^{-}_{\parallel}$ phonon mode (alternating colors on the circular plot makers), but in the LFO film layer the phase of the rotations changed. This rotational phase mismatch is illustrated in figure 5.6.

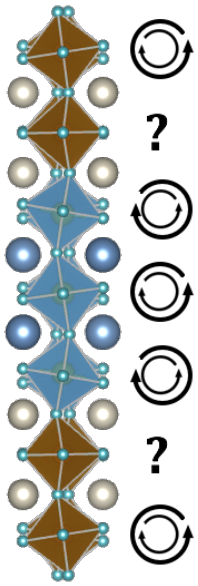

Figure 5.6: The rotations about an in-plane axis corresponding to the $Rot^{-}_{\parallel}$ STO phonon mode in the (3,3) superlattice. The big circular arrows indicate the rotation direction for the foremost octahedra, while the small circular arrow indicate the rotation direction for the rearmost octahedra. Note that the top and bottom octahedra correspond to the same octahedra. Figure made in VESTA [14].

For such a change of rotational phase about an in-plane axis to be possible, the layer between the two different rotational phases must have close-to-zero displace-

ments for the octahedral network to stay corner connected. As the phonon mode frequency for this $\mathrm{Rot}^{-}{}_{\parallel}$ STO phonon mode was far away from the largest imaginary frequency for this superlattice (figure 5.2), the structure corresponding to such displacements – with a rotational phase mismatch over the interface – was not assumed to be probable in the ground state structure.

The $\mathrm{Rot}^{+}{}_{\perp}$ phonon modes

In the phonon modes corresponding to in-phase rotations about the out-of-plane axis ($\mathrm{Rot}^{+}{}_{\perp}$), a lot of similarities was found in the displacement distribution for the different layers in the superlattices (figure 5.7) with what was found for the $\mathrm{Rot}^{-}{}_{\perp}$ phonon modes (figure 5.3). As for the $\mathrm{Rot}^{-}{}_{\perp}$ phonon modes in the $(1,1)_2$ and (2,2) superlattices, no layer showed to have zero displacements for the $\mathrm{Rot}^{+}{}_{\perp}$ phonon modes. Also, by comparing the displacement distribution for the $\mathrm{Rot}^{-}{}_{\perp}$ and $\mathrm{Rot}^{+}{}_{\perp}$ phonon modes in the $(1,1)_2$ superlattice in table 5.1 and 5.3, respectively, one can see that the distribution in the different film layers are exactly the same, except that the majority of the displacements are within the LFO film layers for the $\mathrm{Rot}^{+}{}_{\perp}$ phonon mode, whereas the majority of the displacements were within the STO film layers for the $\mathrm{Rot}^{-}{}_{\perp}$ phonon mode. The reason why the displacements are larger in the LFO film layers for the $\mathrm{Rot}^{+}{}_{\perp}$ phonon mode might be because the bulk structure of LFO contains in-phase rotations about one pseudocubic rotation axis, whereas no in-phase rotations are present in any of the bulk phases of STO, implying that such displacements are more favorable in LFO than in STO.

As for the displacement vector magnitudes for the $\mathrm{Rot}^{-}{}_{\perp}$ STO (LFO) phonon modes in the LFO (STO) layers in the (3,3) superlattice (figure 5.3d-e), the displacement vector magnitudes also reached zero for the $\mathrm{Rot}^{+}{}_{\perp}$ STO (LFO) phonon modes in the middle LFO (STO) layer (figure 5.7d-e). This implies that the proximity effect for both types of rotational modes – both in-phase and out-of-phase, – about the out-of-plane axis, is equally strong. Another similarity between the $\mathrm{Rot}^{-}{}_{\perp}$ and $\mathrm{Rot}^{+}{}_{\perp}$ phonon modes is found for the $\mathrm{Rot}^{-}{}_{\perp}$ STO and $\mathrm{Rot}^{+}{}_{\perp}$ STO phonon mode in the (3,3) superlattice (figure 5.3d and 5.7d, respectively), where almost all displacements in the superlattice are within one single layer of STO.

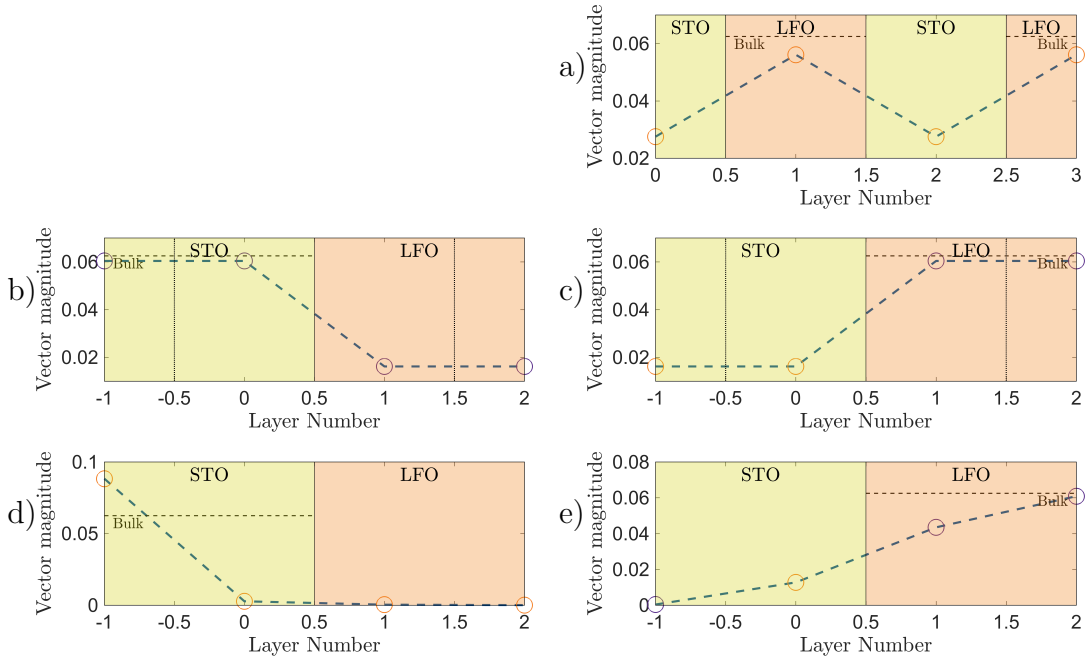

Figure 5.7: In-phase rotation modes about the out-of-plane direction ($Rot^{+}_{\perp}$) in STO (left column) and LFO (right column). a) illustrate the displacement distribution in the $(1,1)_2$ superlattice, while b) and c) illustarte that for the (2,2) superlattice. d) and e) shows the distribution in the (3,3) superlattice. Different colors on the circular plot makers indicate different rotation directions (clockwise or counterclockwise).

Table 5.3: Displacement distributions for in-phase rotations about the out-of-plane direction ($Rot^{+}_{\perp}$) for the [001] oriented superlattices.

	STO modes		LFO modes	
Superlattice	STO	LFO	LFO	STO
$(1,1)_2$	-	-	67.1%	32.9%
(2,2)	78.9%	21.1%	78.9%	21.1%
(3,3)	99.5%	0.5%	88.9%	11.1%

Looking at the $Rot^{+}_{\perp}$ LFO phonon mode in the (3,3) superlattice (figure 5.7e), one can see that the rotations in the LFO layer was in-phase (same color on the circular plot markers), whereas in the interface STO layer the rotations were in the opposite direction of those in the LFO film layer (different color on the circular plot marker). Hence, for this phonon mode there was a rotational phase mismatch at the interface. This did not affect the displacements in the interface layers in the

same way as what was found for the $\text{Rot}^{-}_{\parallel}$ STO phonon mode in figure 5.5. The reason for this is that displacements corresponding to rotations about the out-of-plane axis do not involve oxygen anions that are shared between octahedra in different layers along the out-of-plane axis. Hence, the reason why this rotational phase mismatch occurred in this phonon mode might be because out-of-phase rotations are more favorable than in-phase rotations in the STO film layers – consistent with the structure of the tetragonal phase of bulk STO ($a^0a^0c^-$ tilt pattern). Because the oxygen displacements corresponding to rotations about the out-of-plane axis do not affect the layer above and below directly, such a rotational phase mismatch in the $\text{Rot}^{+}_{\perp}$ phonon mode could be more energetically favorable than a phonon mode where all rotations in all film layers rotated in-phase.

The $\text{Rot}^{+}_{\parallel}$ phonon modes

Just as a lot of similarities were found for the displacement distributions between the in-phase and out-of-phase rotation modes about the out-of-plane axis, a lot of similarities could also be seen for the out-of-phase and in-phase rotations about the in-plane axes (figures 5.5 and 5.8, respectively). For the $\text{Rot}^{+}_{\parallel}$ LFO phonon modes (right column in figure 5.8) the displacements were almost evenly distributed between the STO and LFO film layers in the $(1,1)_2$ superlattice, with 50.2% of the displacements within the LFO layers, and the remaining 49.8% of the displacements in the STO layers (table 5.4). As the film layer thicknesses increased the displacement distribution changed such that more and more of the total displacements were within the LFO film layers. As for the $\text{Rot}^{-}_{\parallel}$ phonon modes, no layers in the superlattices had zero displacements for the $\text{Rot}^{+}_{\parallel}$ phonon modes. The reason for this is assumed to be the same as that for the $\text{Rot}^{-}_{\parallel}$ phonon modes – that is, rotations about the in-plane axes have a longer penetration length than one and a half layer in the [001] oriented superlattices.

The $\text{Rot}^{+}_{\parallel}$ STO phonon mode found in the (3,3) superlattice (figure 5.8c) also showed similar displacement distribution as that for the $\text{Rot}^{-}_{\parallel}$ STO phonon mode illustrated in figure 5.5c. Here, a rotational phase mismatch was also observed at the interface, leading to close-to-zero displacement vectors in the first LFO interface layer.

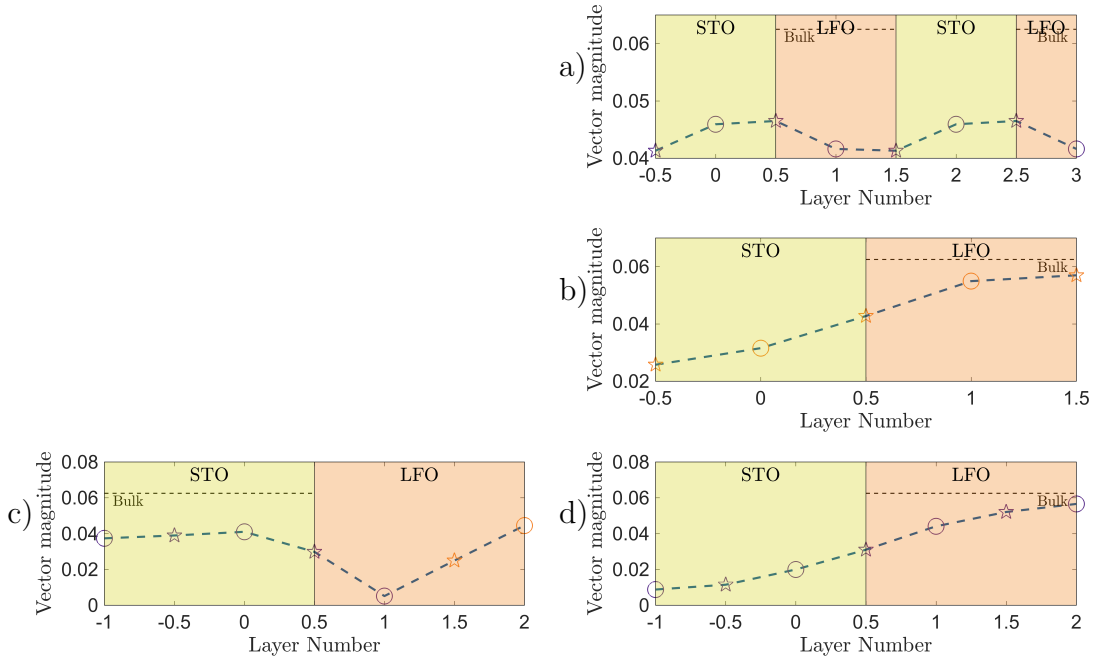

Figure 5.8: In-phase rotation modes about the in-plane directions ($Rot^{+}_{\parallel}$) in STO (left column) and LFO (right column). a) illustrate the displacement distribution in the $(1,1)_2$ superlattice, while b) illustrate that for the (2,2) superlattice. c) and d) shows the distribution in the (3,3) superlattice. Different colors on the circular plot makers indicate different rotation directions (clockwise or counterclockwise).

Table 5.4: Displacement distributions for in-phase rotations about the in-plane directions ($Rot^{+}_{\parallel}$) for the [001] oriented superlattices.

	STO modes		LFO modes	
Superlattice	STO	LFO	LFO	STO
$(1,1)_2$	-	-	50.2%	49.8%
(2,2)	-	-	66.1%	33.9%
(3,3)	61.2%	38.8%	79.2%	20.8%

The P phonon modes

The phonon mode frequencies corresponding to the polar phonon modes in the [001] oriented superlattices had real values and were in general large. Displacements corresponding to such phonon modes were therefore assumed to not be energetically favorable for the structures. That being said, the phonon mode

frequencies for these phonon modes still strengthened the assumption that structural displacements in the superlattices favored displacements favorable for the LFO film layers, and that this effect increased as the film layer thicknesses increased. This statement is based on the frequency value of the $P_{\parallel}$ STO phonon mode relative to that of the $P_{\parallel}$ LFO phonon mode for the different superlattices (figure 5.1). For all superlattices the frequency of the $P_{\parallel}$ LFO phonon mode were approximately equal to that for the LFO supercell, indicating that polar displacements along the in-plane axes in the LFO layers were unfavorable in the superlattices. The frequency for the $P_{\parallel}$ STO phonon mode was relatively low for the $(1,1)_2$ superlattice, but raised to values larger than that for the $P_{\parallel}$ LFO phonon mode in the (2,2) and (3,3) superlattices. The results from the rotation phonon modes, discussed above, showed that the dominance of the LFO phonon modes were smallest in the $(1,1)_2$ superlattice. Hence, the lower frequency value for the $P_{\parallel}$ STO phonon mode in this superlattice is consistent with these findings. As the film layer thicknesses increased in the (2,2) and (3,3) superlattices, this dominance became stronger and, as a consequence, displacements corresponding to the $P_{\parallel}$ STO phonon mode became even less favorable than for the $(1,1)_2$ superlattice.

The $P_{\perp}$ LFO phonon mode frequency also followed the trend described above. Note that, while the $P_{\parallel}$ LFO and $P_{\parallel}$ STO phonon modes had displacement distributions with the majority of the displacements within one of the film materials, the $P_{\perp}$ LFO phonon mode had a more even distribution of displacements in the different film layers (figure 5.9). As the $P_{\perp}$ LFO phonon mode also corresponded to polar displacements in the STO layers, the frequency of this phonon mode followed the same trend as that for the $P_{\parallel}$ STO phonon mode.

The main findings from the phonon mode calculations for the [001] oriented superlattices was that the LFO film layers dominated the STO film layers in that phonon modes corresponding to displacements favorable for the LFO film layers had the largest imaginary phonon mode frequencies. This effect got more evident for thicker film layers.

It was also found that the most favorable displacement for all superlattices corresponded to out-of-phase rotations about the out-of-plane axis. In the [001] oriented superlattices this meant out-of-phase rotations about the pseudocubic [001] rotation axis.

Another finding was that the octahedral coupling associated with the proximity effect had different penetration lengths for rotations about the in-plane axes and the out-of-plane axis. The penetration length was found to be shorter for rotations about the out-of-plane axis than for rotations about the in-plane axes.

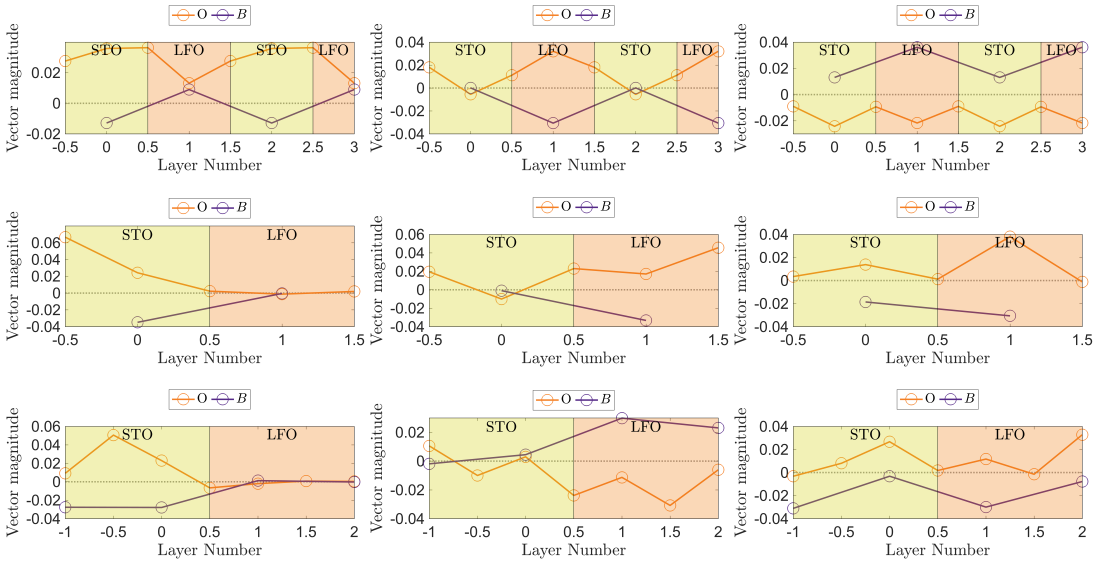

Figure 5.9: The average displacements of the oxygen anions (O) and B cations (B) for each layer in the superlattices in the polar phonon modes. From left to right the displacements corresponding to the $P_{\parallel}$ STO, $P_{\parallel}$ LFO, and $P_{\perp}$ LFO phonon modes are shown. The top figures correspond to the $(1,1)_2$ superlattice, the middle figures to the (2,2) superlattice, and the bottom figures to the (3,3) superlattice. Opposite sign of the vector magnitude means that the displacements are in opposite directions.

5.1.2 [111] oriented superlattices

Now the findings from the calculations of the [111] oriented supercell and superlattices will be given. Figure 5.10 shows the frequencies found for the Rot^{+}, $Rot^{-}{}_{\perp/\parallel}$, and $P_{\perp/\parallel}$ STO and LFO phonon modes. Note that, as in-phase rotations about the in-plane axes and out-of-plane axis in [111] oriented systems are symmetry equivalent. Therefore, it is not distinguished between the rotation axes for this phonon mode in these structures.

The frequencies for the STO supercell in figure 5.10 are those for the [001] oriented STO supercell discussed in the previous section. As this supercell is fully relaxed, the orientation does not matter.

For the [111] oriented LFO supercell the largest imaginary frequencies corresponded to those for the Rot^{-} phonon modes, where the rotation phonon modes corresponding to rotations about the in-plane axes had a slightly larger imaginary frequency that that for the out-of-plane rotations. This difference was at $\sim$ 42 GHz. Other imaginary phonon mode frequencies for the [111] oriented LFO supercell was that for in-phase rotations (Rot^{+}), while the phonon modes corresponding to polar displacements had high real frequencies.

Looking at the phonon mode frequencies found for the [111] oriented super-

lattices one can see that, for all superlattices the Rot$_-$ phonon modes were the phonon modes with the largest imaginary frequencies, just as what was seen for the LFO and STO supercells. For the $(1,1)_{3,\mathrm{FM}}$ and $(1,1)_{6,\mathrm{AF}}$ superlattices the $\mathrm{Rot}^-_\perp$ phonon mode had the majority of the displacements associated with this phonon mode within the LFO film layers (pink circle in figure 5.10), while the $\mathrm{Rot}^-_\parallel$ phonon mode had the majority of the displacements within the STO film layers (cyan cross). For the $(3,3)_2$ superlattice, however, both Rot^- phonon modes corresponding to the phonon modes with the largest imaginary frequency had the majority of displacements withing the LFO film layers (pink circle and cross). This implied that for superlattices with a short periodicity of one, the displacements favorable for the superlattices corresponded to favorable displacements in both bulk film materials. For superlattices with a longer periodicity of three, however, the most favorable displacements seemed to be those corresponding to favorable displacements in the LFO film layers. Hence, when the layer thickness increased (longer period, m), the displacements favorable for the LFO film layers seemed to be the prioritized displacements for the superlattice.

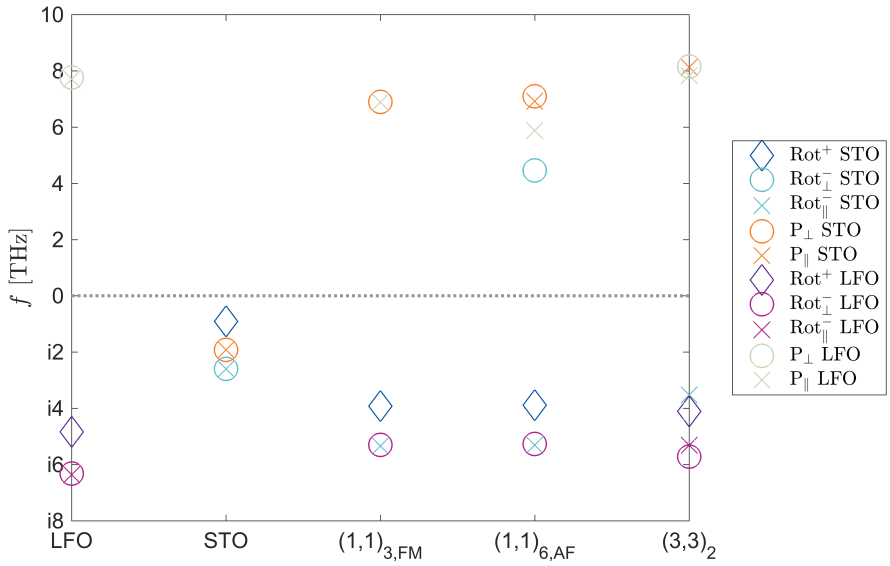

Figure 5.10: Phonon mode frequencies (f) for the LFO and STO supercells, and the $(1,1)_{3,\mathrm{FM}}$, $(1,1)_{6,\mathrm{AF}}$, and $(3,3)_2$ superlattices.

As the polar phonon modes had large real frequencies for all superlattices, these phonon modes were considered less important when looking at how the different film layer thicknesses and magnetic structure could affect the structure in the different layers. Hence, these phonon modes will not be discussed any further.

Figure 5.11 shows the imaginary phonon modes found for the [111] oriented supercell and superlattices, excluding the real value phonon mode frequencies

for clarity. The results for the rotation phonon modes will now be covered, one phonon mode at a time.

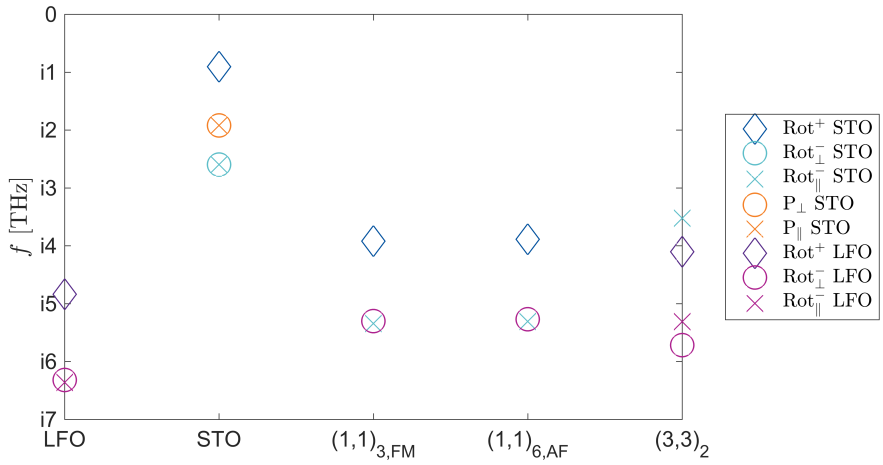

Figure 5.11: Imaginary phonon mode frequencies (f) for the LFO and STO supercells, and the $(1,1)_{3,FM}$, $(1,1)_{6,AF}$, and $(3,3)_2$ superlattices.

The $Rot^-_\perp$ phonon modes

The phonon modes corresponding to out-of-phase rotations about the out-of-plane axis ($Rot^-_\perp$) had large imaginary frequencies in all superlattices (pink circles in figure 5.11). The distribution of displacements corresponding to these phonon modes in the different layers in the superlattices are showed in figure 5.12, and the displacement distribution for each film material are given in table 5.5.

Looking at the displacement distribution for the $Rot^-_\perp$ LFO phonon modes in the (1,1) superlattices in table 5.5, one can see that there were no difference in the distribution of displacements between the $(1,1)_{3,FM}$ and $(1,1)_{6,AF}$ superlattices. However, when looking at the displacement vector magnitudes corresponding to these phonon modes in figures 5.12a and 5.12c, one can see that the displacements are larger in the $(1,1)_{3,FM}$ superlattice than in the $(1,1)_{6,AF}$ superlattice.

The $Rot^-_\perp$ STO phonon mode found for the $(1,1)_{6,AF}$ showed close-to-zero displacements in the LFO film layers and 96.6% of the total displacements within the STO film layers (figure 5.12b and table 5.5). As the frequency of this phonon mode had a relatively large real value, displacements corresponding to this phonon mode was assumed to not be favorable in a ground state structure.

As the layer thickness increased from one unit cell along the pseudocubic [111] direction to three unit cells in the $(3,3)_2$ superlattice, the $Rot^-_\perp$ LFO phonon modes showed a larger distribution of displacements in the LFO film layers (table 5.5). This indicated that thicker film layers favored displacements in the LFO film layers more, while suppressing displacements in the STO film layers. From figure 5.12d one can see that the displacement vector magnitudes in the LFO film

layers almost reach that of the LFO supercell. Hence, one can assume that a film layer thickness of three unit cells along the pseudocubic [111] direction is not sufficient for the structure in the LFO layers to obtain the same structure as that found in thicker LFO films away from the substrate/film interface. In addition, one can see that the displacement vector magnitude in the STO film layers for this phonon mode did not reach zero, indicating that the octahedral coupling associated with the proximity effect for this phonon mode had a longer penetration length in the [111] oriented superlattices than one and a half unit cells along the out-of-plane direction.

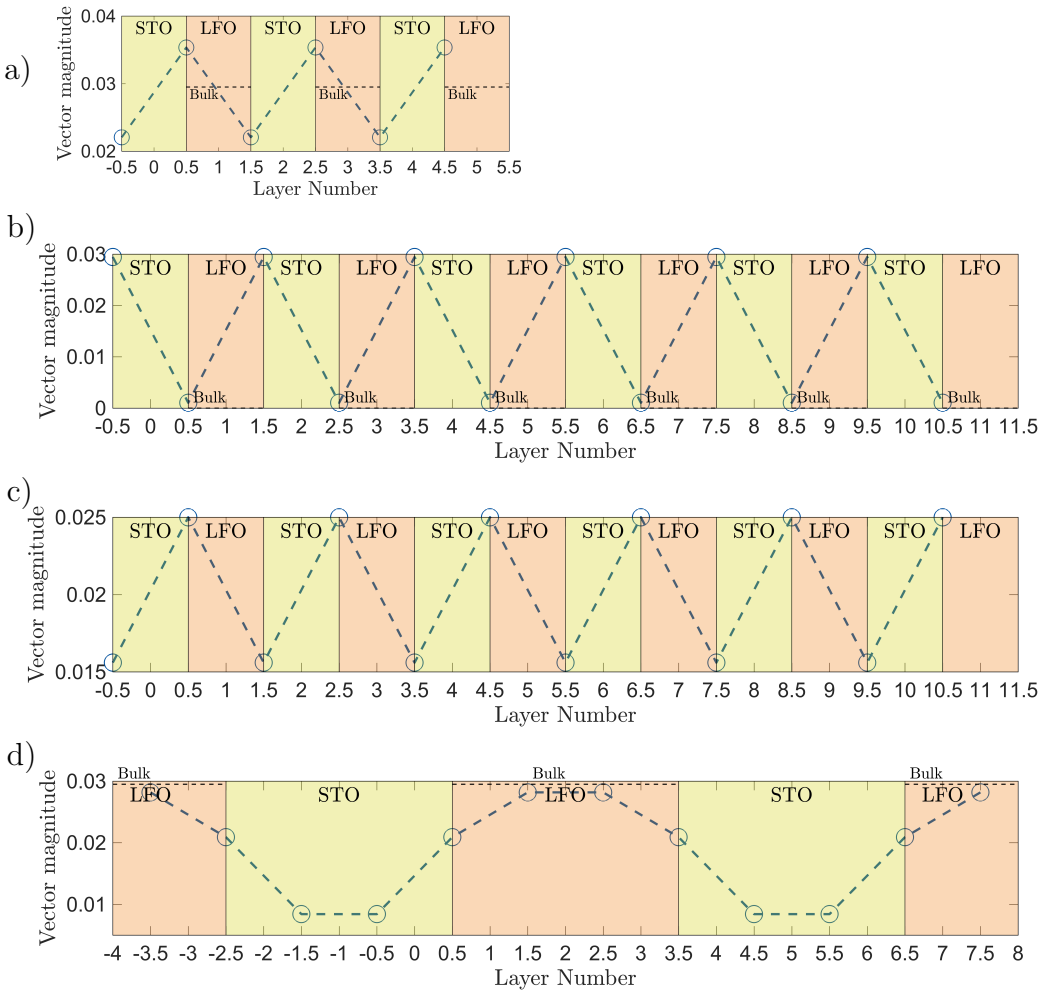

Figure 5.12: Out-of-phase rotation modes about the out-of-plane direction ($Rot^{-}_{\perp}$) in STO and LFO. a) illustrate the displacement distribution in the $(1,1)_{3,FM}$ superlattice for the LFO mode, while b) and c) illustrate that for the $(1,1)_{6,AF}$ for the STO and LFO mode,respectively. d) shows the distribution of the displacements in the LFO mode in the $(3,3)_2$ superlattice.

Table 5.5: Displacement distributions for out-of-phase rotations about the out-of-plane direction ($Rot^-_\perp$) for the [111] oriented superlattices.

	STO modes		LFO modes	
Superlattice	STO	LFO	LFO	STO
$(1,1)_{3,FM}$	-	-	61.6%	38.4%
$(1,1)_{6,AF}$	96.6%	3.4%	61.6%	38.4%
$(3,3)_2$	-	-	74.5%	25.5%

The $Rot^-_\parallel$ phonon modes

The largest imaginary phonon mode frequency found for the (1,1) superlattices and the next largest imaginary frequency for the $(3,3)_2$ superlattice corresponded to out-of-phase rotations about the in-plane axes ($Rot^-_\parallel$). For the (1,1) superlattices it was found one $Rot^-_\parallel$ phonon mode, with the majority of the displacements within the STO layers (figure 5.13a and b). As for the $Rot^-_\perp$ LFO phonon modes, there was almost no difference between the displacement distribution between the STO and LFO film layers for the $Rot^-_\parallel$ STO phonon modes (table 5.6), with about 54.5% of the displacements within the STO film layers, and 45.5% displacements within the LFO film layers. The difference for this phonon mode, in the different (1,1) superlattices, was again the displacement vector magnitudes, where the magnitudes were larger in the $(1,1)_{3,FM}$ superlattice than in the $(1,1)_{6,AF}$ superlattice (figures 5.13a and b, respectively).

For the $(3,3)_2$ superlattice it was found two $Rot^-_\parallel$ phonon modes, one with the majority of the displacements in the STO film layers (figure 5.13c), and one with the majority of the displacements within the LFO film layers (figure 5.13d). The latter phonon mode corresponded to the phonon mode with the largest imaginary phonon mode frequency of these two phonon modes (figure 5.11). This was as expected, as this phonon mode corresponded to out-of-phase rotations about two pseudocubic rotation axes. As the bulk LFO structure has out-of-phase rotations about two pseudocubic rotation axes, while the structure in the tetragonal phase of bulk STO only has out-of-phase rotations about one pseudocubic axis, displacements corresponding to the $Rot^-_\parallel$ phonon mode in [111] oriented systems was assumed to be more favorable in the LFO film layers than in the STO film layers.

When comparing the displacement distribution in the different film layers for $Rot^-_\parallel$ LFO phonon mode with that found for the (1,1) superlattices in table 5.6, one can see that the thicker film layers in the $(3,3)_2$ superlattice increased the distribution of displacements in the LFO film layers. Hence, the assumption that thicker film layers caused the LFO phonon modes to dominate more, strengthened.

Looking at the displacement vector magnitudes for each layer in the $(3,3)_2$

superlattice for the $\text{Rot}^{-}_{\parallel}$ STO and LFO phonon modes in figures 5.13c and d, respectively, one can see that the vector magnitude did not reach zero in any of the film layers. Hence, the penetration length for these kind of distortions was assumed to be longer than one and a half unit cell along the pseudocubic [111] direction.

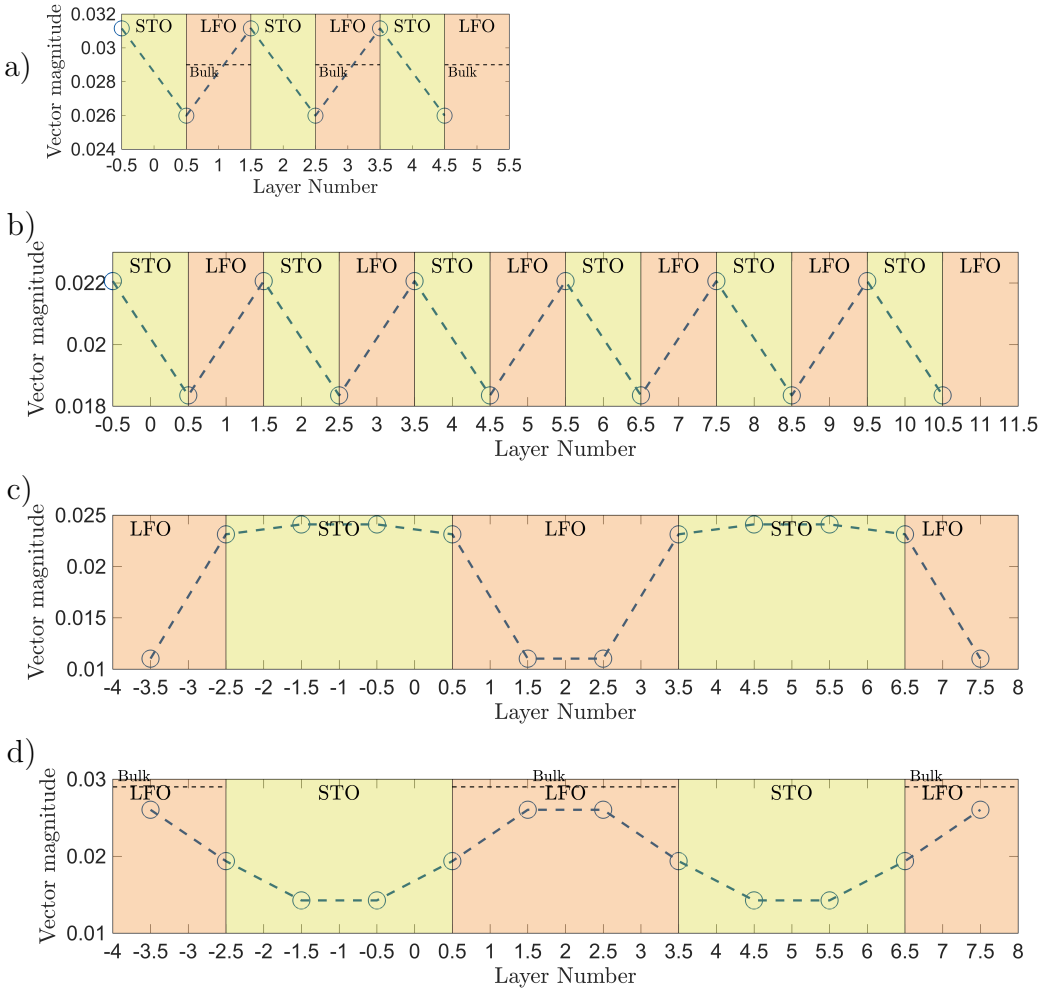

Figure 5.13: Out-of-phase rotation modes about the in-plane directions ($\text{Rot}^{-}_{\parallel}$) in STO and LFO. a) illustrate the displacement distribution in the $(1,1)_{3,\text{FM}}$ superlattice for the STO mode, while b) illustrate that for the $(1,1)_{6,\text{AF}}$ for the STO mode. c) and d) shows the distribution of the displacements in the STO and LFO mode, respectively, in the $(3,3)_2$ superlattice.

Table 5.6: Displacement distributions for out-of-phase rotations about the in-plane directions ($Rot^-_{\parallel}$) for the [111] oriented superlattices.

	STO modes		LFO modes	
Superlattice	STO	LFO	LFO	STO
$(1,1)_{3,FM}$	54.5%	45.5%	-	-
$(1,1)_{6,AF}$	54.6%	45.4%	-	-
$(3,3)_2$	58.5%	41.5%	61.4%	38.6%

The Rot^+ phonon modes

The last phonon mode that will be covered for the [111] oriented superlattices is the one corresponding to in-phase rotations about one of the pseudocubic rotation axes (Rot^+). It was found one Rot^+ phonon mode for each superlattice. In the (1,1) superlattices the majority of the displacements in this phonon mode were within the STO film layers, whereas the majority of the displacements were within the LFO film layers for the $(3,3)_2$ superlattice (figure 5.14 and table 5.7).

Yet again, the displacement distributions for the Rot^+ phonon mode in the (1,1) superlattices were equal (table 5.7), while the displacement vector magnitudes were larger for in the $(1,1)_{3,FM}$ superlattice than for the $(1,1)_{6,AF}$ superlattice (figure 5.14a and b, respectively). Also, the distribution of displacements within the LFO film layers increased as the film layer thicknesses increased.

In figure 5.14c one can see that the displacement vector magnitude reach the value found for the LFO supercell, indicating that a layer thickness of three unit cells along the [111] direction was sufficient for the middle LFO layers to reach the same in-phase rotation magnitude as that found for bulk LFO. Yet, the displacement vector magnitude in the STO film layers did not reach zero. Hence, the penetration length for rotations associated with the Rot^+ phonon mode was also assumed to be longer than one and a half unit cells along the pseudocubic [111] direction.

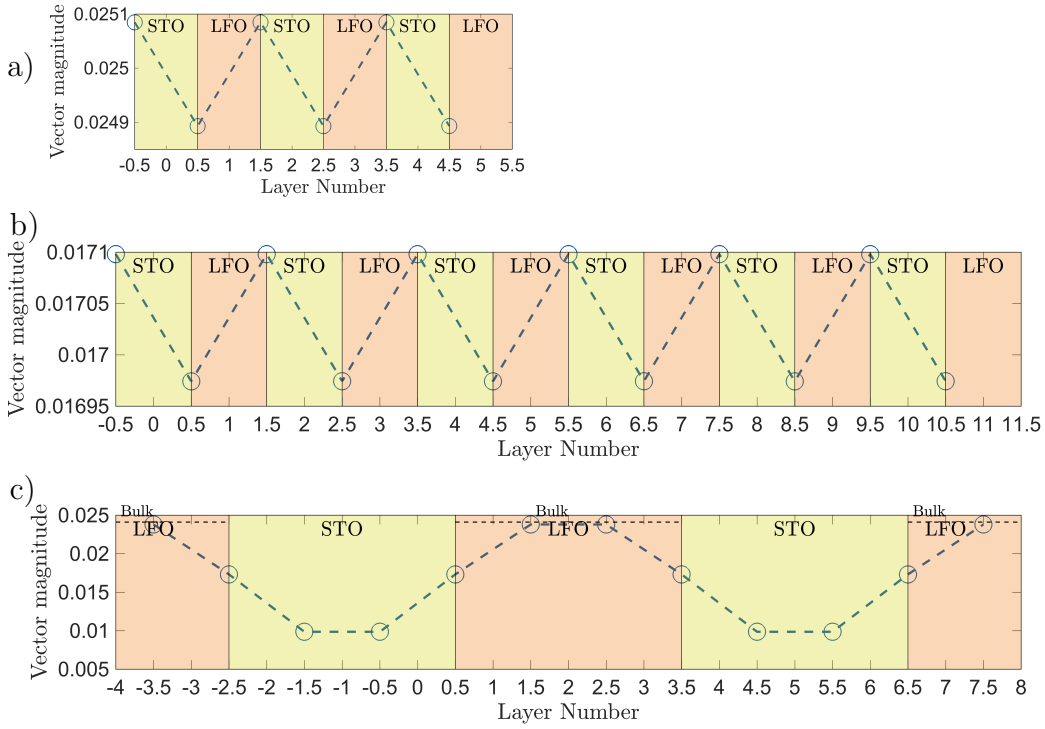

Figure 5.14: In-phase rotation modes (Rot^+) in STO and LFO. a) illustrate the displacement distribution in the $(1,1)_{3,FM}$ superlattice for the STO mode, while b) illustrate that for the $(1,1)_{6,AF}$ for the STO mode. c) shows the distribution of the displacements in the LFO mode in the $(3,3)_2$ superlattice.

Table 5.7: Displacement distributions for in-phase rotations (Rot^+) for the [111] oriented superlattices.

	STO modes		LFO modes	
Superlattice	STO	LFO	LFO	STO
$(1,1)_{3,FM}$	50.2%	49.8%	-	-
$(1,1)_{6,AF}$	50.2%	49.8%	-	-
$(3,3)_2$	-	-	67.6%	32.4%

From the results obtained from the phonon mode calculations for the [111] oriented superlattices one could see that the magnetic structure in (1,1) superlattices did not affect the distribution of displacements between the different film layers, but a ferromagnetic (FM) ordering of the Fe layers seemed to cause larger displacements in the overall structure than an antiferromagnetic (AF) ordering.

When comparing the displacement distribution for the Rot^- phonon modes with the largest imaginary frequencies in tables 5.5 and 5.6, one can see that the displacements were more evenly distributed over the different film layers for the phonon modes corresponding to rotations about the in-plane axes ($Rot^-_{\parallel}$), than those corresponding to rotations about the out-of-plane axis ($Rot^-_{\perp}$). This indicated that the octahedral coupling associated with the proximity effect was stronger for rotations about the in-plane axes than for rotations about the out-of-plane axis.

5.1.3 Comparison of the results obtained for the [001] and [111] oriented systems

The main similarities between the results obtained from the [001] and [111] oriented systems are listed below.

- Rotations about the in-plane axes seemed to couple more strongly than rotations about the out-of-plane axis.
- The phonon modes corresponding to displacements in the LFO film layers had in general larger imaginary frequencies than phonon modes corresponding to displacements in the STO film layers. This effect increased as the film layer thicknesses increased.
- The superlattices with both orientations favored out-of-phase rotations about each pseudocubic rotation axis over in-phase rotations.

The main differences between the results found for the [001] and [111] oriented systems were as follows:

- For the [001] oriented superlattices, film layer thicknesses of two unit cells along the out-of-plane direction was sufficient for the displacement vector magnitudes in the out-of-plane rotation modes to reach that of the bulk supercell (figures 5.3 and 5.7). For the [111] oriented superlattices, however, film layer thicknesses of three unit cells along the out-of-plane axis were just to small for the out-of-phase rotations about the out-of-plane axis to reach that for the LFO supercell (figure 5.12).
- For the [001] oriented superlattices it was found that the penetration length for rotations about the out-of-plane axis was about one and a half unit cells. For the [111] oriented superlattices the penetration length was found to be longer for the same kind of rotations.
- In the $(1,1)_2$ [001] oriented superlattice it was found one polar phonon mode with a low real frequency (figure 5.1). The same phonon mode was found

to have high real frequencies in the (1,1) [111] oriented superlattices (figure 5.10). This indicated that polar displacements were even less probable in (1,1) [111] oriented superlattices than in (1,1) [001] oriented superlattices.

Looking at the penetration lengths found for the rotation modes in the superlattices with different orientations, it seems like the penetration length is determined based on distance rather than number of unit cells along the out-of-plane axis, implying a steric effect. Three unit cells along the [111] direction corresponded to about 6.75 Å for these systems. This is a shorter distance than that corresponding to two unit cells along the [001] direction, which is about 7.79 Å. This explains the differences between the results obtained for the [001] and [111] oriented systems discussed to the first two points above.

5.2 Frozen-in phonon mode calculations

In this section the results obtained from the frozen-in phonon mode calculations will be presented. Section 5.2.1 covers the results from the various frozen-in phonon modes in the LFO_3/STO_3 [001] oriented superlattice, while the result from the calculations of the LFO_3/STO_3 [111] oriented superlattice are presented in section 5.2.2. In section 5.2.3 the main findings from all of these calculations are summarized.

5.2.1 The LFO_3/STO_3 [001] oriented superlattice

Four different sets of frozen-in phonon modes were tried out as initial trial structures for the frozen-in phonon mode calculations for the LFO_3/STO_3 [001] oriented superlattice. These four sets corresponded to:

1. Different distributions of in-plane and out-of-plane rotation magnitudes for structures with an $a^-a^-c^+$ tilt pattern in the LFO film layers.

2. Different distributions of in-plane and out-of-plane rotation magnitudes for structures with an $a^+a^-c^-$ tilt pattern in the LFO film layers.

3. Different total rotation magnitudes for structures with an $a^+a^-c^-$ tilt pattern in the LFO film layers.

4. Structures with various tilt patterns in the LFO film layers, not found in bulk LFO. These tilt pattern were $a^+b^-c^-$, $a^0a^0c^-$, and $a^-a^-c^-$.

The results obtained from the different frozen-in phonon mode sets will now be presented in the order given above. After these results are presented the energy corresponding to the relaxed structures will be compared.

Structures with an $a^-a^-c^+$ tilt pattern in LFO film layers

The rotation and tilt magnitudes in the initial trial structures with different distributions of in-plane and out-of-plane rotation magnitudes in the $a^-a^-c^+$ tilt pattern are showed in figure 5.15. The (3,3) superlattice were build up of three layers of FeO_6 octahedra and three layers of TiO_6 octahedra along the out-of-plane direction. In some of these layers there were octahedra with different rotation and tilt magnitudes. For example, in the first interface LFO layer (layer number 1 in figure 5.15), half of the octahedra could have one rotation magnitude about the out-of-plane axis (γ), while the other half of the octahedra in this layer had a different γ rotation magnitude. In figure 5.15 the average magnitudes for each layer are plotted. For exact values with uncertainties corresponding to these differences in magnitude, see appendix A.1.

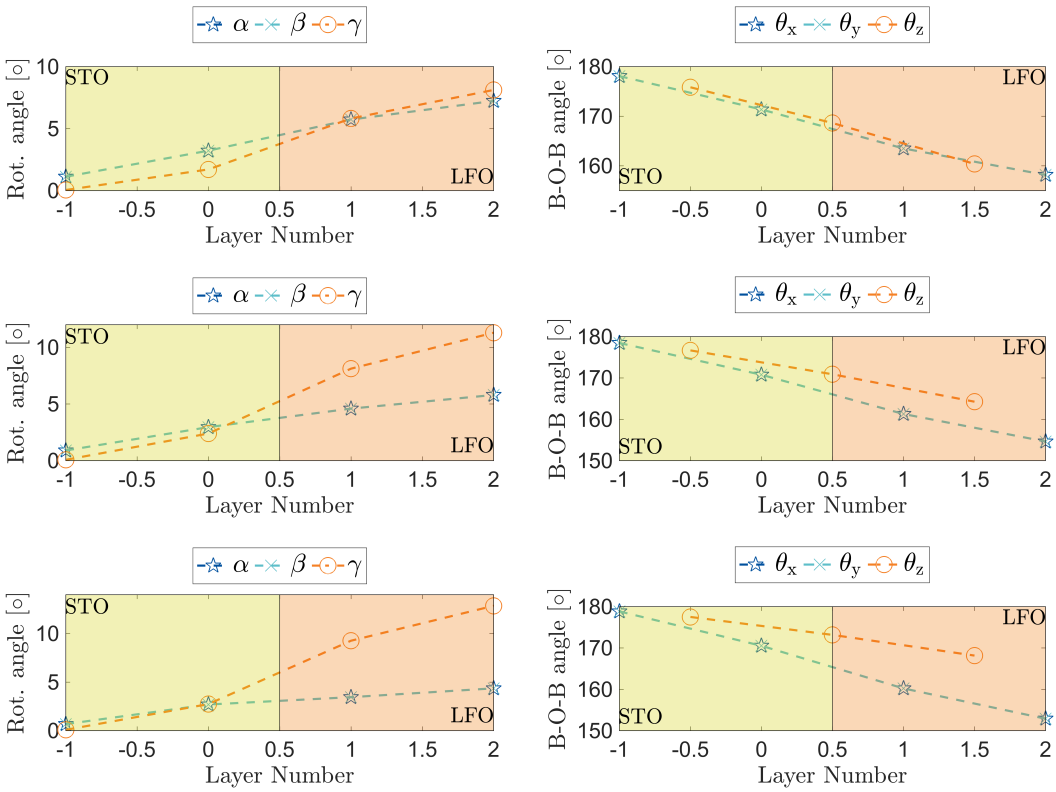

Figure 5.15: Rotation angles (left column) and B-O-B tilt angles (right column) in the three initial trial structures for the (3,3) [001] oriented superlattice with LFO layers with an $a^-a^-c^+$ tilt pattern. From the top figures to the bottom figures the distribution of in-plane and out-of-plane rotations become more unevenly distributed. See tables A.11, A.12, and A.13, respectively, in appendix A.1 for exact values.

None of the three initial structures showed in figure 5.15 converged in the strained

relaxation calculations. This implied that in-phase rotations about the out-of-plane direction in the LFO film layers were unfavorable. It might still have been an energy minimum corresponding to an $a^-a^-c^+$ tilt pattern in the LFO film layers for this superlattice. If that was the case, none of the initial trial structures with this tilt pattern, tried out in this master thesis, were close enough to the structure corresponding to that energy minimum. As a result, the initial trial structures could not "find" that stable structure in the strained relaxation calculations. However, the assumption that these results showed that in-phase rotations about the out-of-plane direction in the LFO film layers were unfavorable, coincide with experimental findings for LFO films grown on STO substrates [30].

Structures with an $a^+a^-c^-$ tilt pattern in the LFO film layers

Two different sets of initial trial structures were utilized for structures with the $a^+a^-c^-$ tilt pattern in the LFO film layers:

1. Different distributions of in-plane and out-of-plane rotation magnitudes – the same kind of testing as was performed for the structures with the $a^-a^-c^+$ tilt pattern in the LFO film layers, discussed above. Three initial trial structures were tested for this set, and the rotation and tilt magnitudes for these structures are shown in figure 5.16.

2. Different total rotation magnitudes. Two initial trial structures were tested for this set. For both structures, the total rotation magnitude in the structures were close to evenly distributed between rotations about the in-plane and out-of-plane axes, that is $\alpha \approx \beta \approx \gamma$ (figure 5.18). The result from this set is covered after the result from the first set.

For both sets, there were some differences in the tilt and rotation magnitudes for octahedra in the same layer in the superlattices (as discussed above for the structures with the $a^-a^-c^+$ tilt pattern). For exact magnitude values with uncertainties corresponding to these differences, see appendix A.1.

All initial trial structures in the first set (figure 5.16) converged to a relaxed structure in the strained relaxation calculations. The resulting structures were approximately the same for all initial trial structures, with differences in angles of about 0.2°, and differences in the **c** lattice parameters of about 8×10^{-4} Å. The rotation and tilt magnitudes of the resulting structure for these initial trial structures are shown in figure 5.17. Here, the result from the top initial trial structure in figure 5.16 is shown – representing the result for all three initial trial structures in figure 5.16. Table 5.8 shows the resulting rotation and tilt magnitude values for the structure shown in figure 5.17 with uncertainties corresponding to the differences in rotation and tilt magnitudes for octahedra in the same layer. The layer numbers in table 5.8 corresponds to the layer numbers in the plots in figure 5.17.

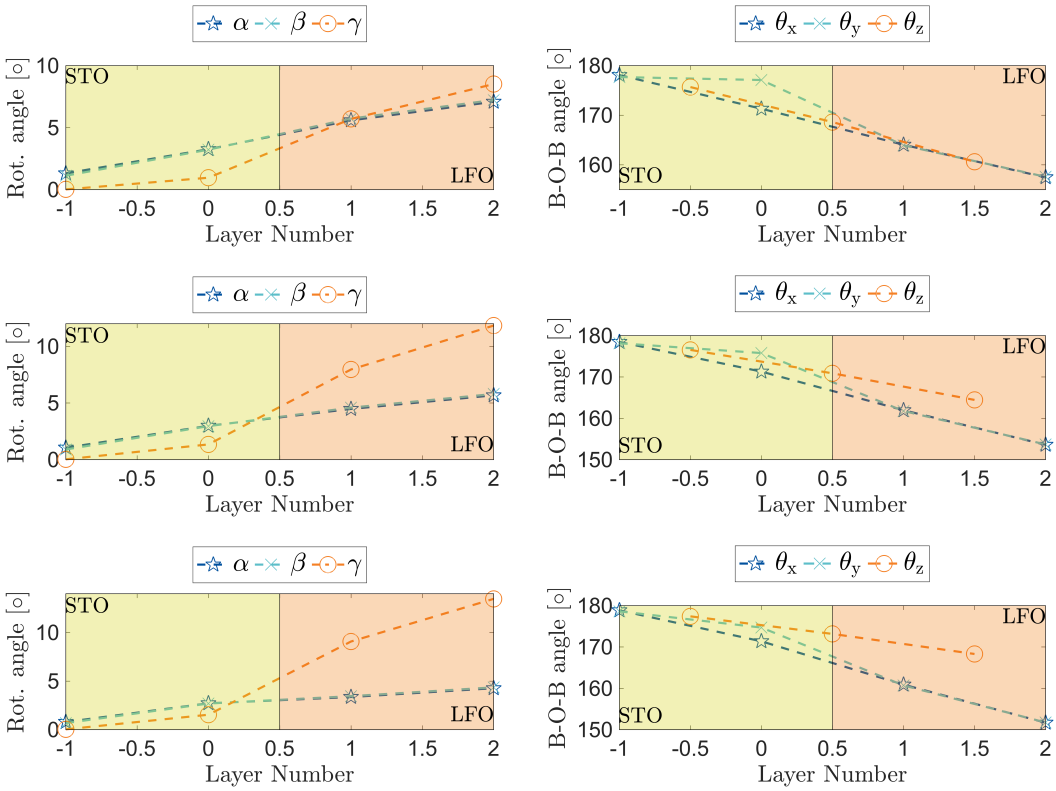

Figure 5.16: Rotation angles (left column) and B-O-B tilt angles (right column) in the three initial trial structures for the first set for the (3,3) [001] oriented superlattice with LFO layers with an $a^+a^-c^-$ tilt pattern. From the top figures to the bottom figures the distribution of in-plane and out-of-plane rotations become more unevenly distributed. See tables A.14, A.15, and A.16, respectively, in appendix A.1 for exact values.

Looking at the rotation magnitudes in the resulting structure (left figure in figure 5.17) one can see that the $a^+a^-c^-$ tilt pattern relaxed to an $a^+b^-c^-$ tilt pattern in the middle LFO layer (layer number 2), with $\alpha < \beta < \gamma$. In a strained relaxation calculation preformed on an LFO supercell with fixed **a** and **b** lattice parameters corresponding to that of STO, and an $a^-b^+a^-$ tilt pattern (part of the structure calculations), the rotation magnitudes were found to be $\alpha_\mathrm{b} = 8.1°$, $\beta_\mathrm{b} = 6.1°$, and $\gamma_\mathrm{b} = 8.8°$ (subscript "b" for "bulk"), corresponding to out-of-phase rotations about the in-plane [100] axis, in-phase rotations about the in-plane [010] axis, and out-of-phase rotations about the out-of-plane [001] axis, respectively. Comparing the magnitude of the in-phase rotation about the in-plane axis for this supercell (β_b) with that of the magnitude of the in-phase rotation about the in-plane axis in layer number 2 (LFO layer furthest away from the interface) in the superlattice ($\alpha(2)$), one can see that the LFO film layer did not quite reach the rotation magnitude for in-phase rotations about an in-plane axis correspond-

ing to an LFO structure far away from the interface. However, the out-of-phase rotations about both the in-plane and out-of-plane axis in this layer ($\beta(2)$ and $\gamma(2)$, respectively) had reach the values corresponding to the LFO supercell (α_b and γ_b, respectively). This implied that the STO film layers suppressed in-phase rotations about an in-plane axis in the LFO film layers more than it suppressed out-of-phase rotations about both in-plane and out-of-plane axes.

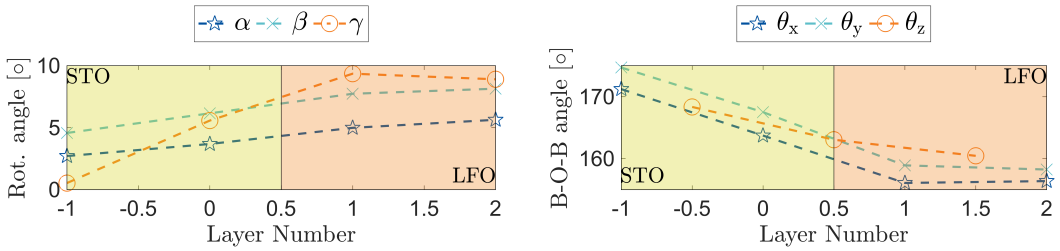

Figure 5.17: The resulting rotation angles (left) and B-O-B tilt angles (right) from the strained relaxation calculation of the initial trial structures for the first set for the (3,3) [001] oriented superlattice with LFO layers with an $a^+a^-c^-$ tilt pattern (figure 5.16).

Table 5.8: The resulting rotation angles (α, β, γ) and B-O-B tilt angles ($\theta_{x,y,z}$), in degrees, from the strained relaxation calculation of the initial trial structures for the first set for the (3,3) [001] oriented superlattice with LFO layers with an $a^+a^-c^-$ tilt pattern (figure 5.16).

Layer number	α	β	γ	θ_x	θ_y	θ_z
-1	2.7	4.6	0.5	171.2±0.1	174.7	-
-0.5	-	-	-	-	-	168.3±0.5
0	3.7	6.2 ± 0.2	5.6 ± 0.2	163.7±4.1	167.5	-
0.5	-	-	-	-	-	163.0±0.5
1	5.0	7.7 ± 0.6	9.4 ± 0.6	156.1±0.2	158.9	-
1.5	-	-	-	-	-	160.4±0.3
2	5.6	8.1 ± 0.8	8.9 ± 0.7	156.4±0.1	158.2	-

Looking at the propagation of the LFO tilt pattern into the STO film layer one can see that the rotations about the in-plane axes (α and β) coupled more strongly than the rotation about the out-of-plane axis (γ). This resulted in a tilt pattern

close to $a^+b^-c^0$ in the middle layer in the STO film, a tilt pattern not found in bulk STO. As in the LFO film layer, the rotation magnitude of the in-phase rotations about the in-plane axis was smaller than for the out-of-phase rotation about the in-plane axis. This might be because in-phase rotations are not present in any of the phases of bulk STO.

For the second set of initial trial structures with the $a^+a^-c^-$ tilt pattern in the LFO film layers, two initial trial structures were tested. The rotation and tilt magnitudes in these initial structures, where the total rotation magnitudes were close to evenly distributed between rotations about the in-plane and out-of-plane axes, are showed in figure 5.18.

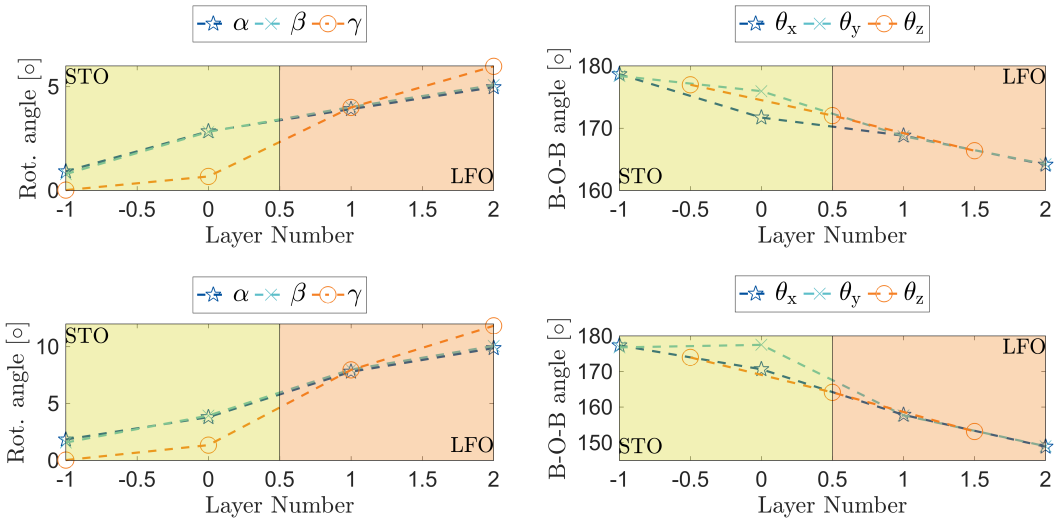

Figure 5.18: Rotation angles (left column) and B-O-B tilt angles (right column) in the two initial trial structures for the second set for the (3,3) [001] oriented superlattice with LFO layers with an $a^+a^-c^-$ tilt pattern. From the top figures to the bottom figures the total rotation magnitude has increased. See tables A.17 and A.18, respectively, in appendix A.1 for exact values.

The initial trial structure corresponding to the top figures in figure 5.18 converged in the strained relaxation calculation, and the rotation and tilt magnitudes in the resulting structure are shown in figure 5.19. The values of these rotation and tilt magnitudes – with uncertainties corresponding to different magnitudes for octahedra in the same layer – are given in table 5.9.

Comparing the resulting structures from the two different sets of initial trial structures in figures 5.17 and 5.19 and tables 5.8 and 5.9, one can see that these structures have approximately equal rotation and tilt magnitudes. As four different initial trial structures relaxed to the same structure, this structure was assumed to be stable for this system.

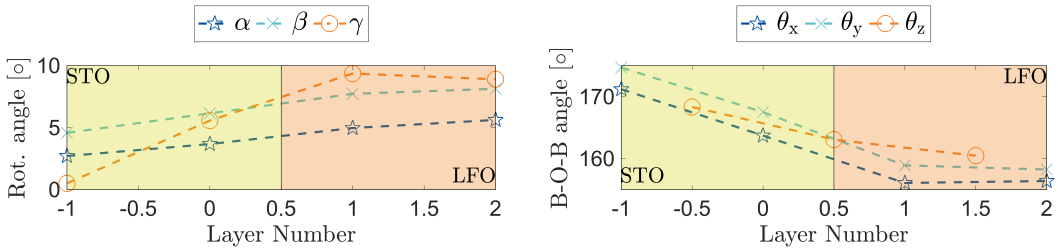

Figure 5.19: The resulting rotation angles (left) and B-O-B tilt angles (right) from the strained relaxation calculation of the initial trial structure corresponding to the top figures in figure 5.18.

Table 5.9: The resulting rotation angles (α, β, γ) and B-O-B tilt angles ($\theta_{x,y,z}$), in degrees, from the strained relaxation calculation of the initial trial structure corresponding to the top figures in figure 5.18.

Layer number	α	β	γ	θ_x	θ_y	θ_z
-1	2.7	4.6	0.5	171.2±0.1	174.7	-
-0.5	-	-	-	-	-	168.3±0.5
0	3.7	6.2 ± 0.2	5.6 ± 0.2	163.7±4.1	167.5	-
0.5	-	-	-	-	-	163.1±0.5
1	5.0	7.7 ± 0.6	9.4 ± 0.6	156.1±0.2	158.9	-
1.5	-	-	-	-	-	160.5±0.3
2	5.6	8.1 ± 0.7	8.9 ± 0.7	156.4±0.1	158.2	-

The second initial trial structure (bottom figures in figure 5.18) did not converge properly, indicating that such a structure, with large total rotation magnitude, was far away from a stable structure for the superlattice.

Structure with an $a^+b^-c^-$ tilt pattern in the LFO film layers

The tilt pattern found in the resulting structures from strained relaxation calculations of initial trial structures with an $a^+a^-c^-$ tilt pattern (discussed above), namely the $a^+b^-c^-$ tilt pattern, was also the tilt pattern of one initial trial structure. The rotation and tilt magnitudes for this initial structure are shown in figure 5.20. For exact values of these magnitudes see appendix A.1, table A.19.

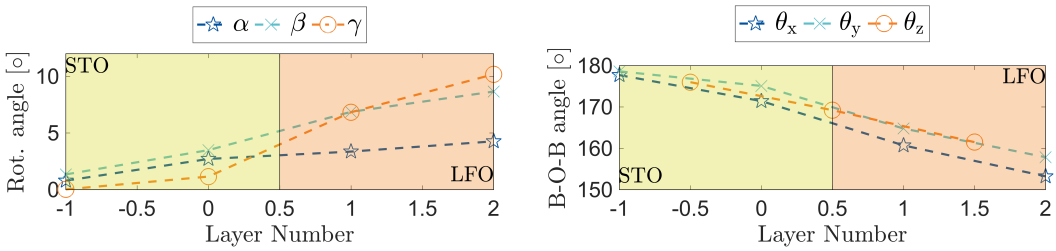

Figure 5.20: Rotation angles (left) and B-O-B tilt angles (right) in the initial trial structure for the (3,3) [001] oriented superlattice with LFO layers with an $a^+b^-c^-$ tilt pattern.

This initial trial structure, relaxed – in the strained relaxation calculations – to approximately the same structure as the results from the four initial trial structures with an $a^+a^-c^-$ tilt pattern, discussed above. The resulting rotation and tilt magnitudes are shown in figure 5.21 and the values are given in table 5.10.

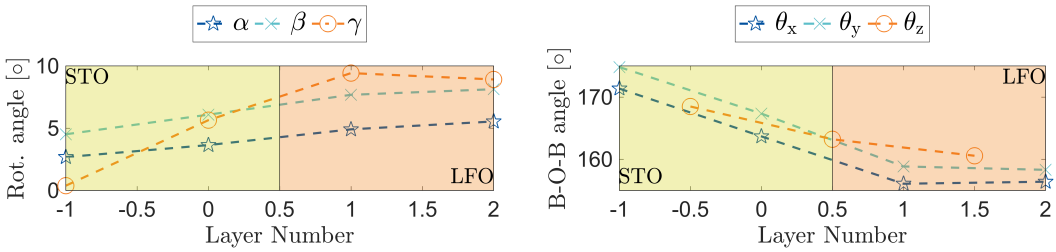

Figure 5.21: The resulting rotation angles (left) and B-O-B tilt angles (right) from the strained relaxation calculation of the initial trial structure for the (3,3) [001] oriented superlattice with LFO layers with an $a^+b^-c^-$ tilt pattern (figure 5.20).

Table 5.10: The resulting rotation angles (α, β, γ) and B-O-B tilt angles ($\theta_{x,y,z}$), in degrees, from the strained relaxation calculation of the initial trial structure for the (3,3) [001] oriented superlattice with LFO layers with an $a^+b^-c^-$ tilt pattern (figure 5.20).

Layer number	α	β	γ	θ_x	θ_y	θ_z
-1	2.7	4.5	0.4	171.4	174.8	-
-0.5	-	-	-	-	-	168.5±0.4
0	3.6	6.1 ± 0.2	5.6 ± 0.2	163.7±4.1	167.3	-
0.5	-	-	-	-	-	163.2±0.6
1	4.9	7.7 ± 0.6	9.4 ± 0.6	156.1±0.2	158.8	-
1.5	-	-	-	-	-	160.6±0.3
2	5.5	8.1 ± 0.7	8.9 ± 0.6	156.4±0.1	158.3	-

Structure with an $a^0a^0c^-$ tilt pattern in the LFO film layers

The second initial trial structure with a tilt pattern not found in bulk LFO was a structure with an $a^0a^0c^-$ tilt pattern in the LFO film layers. The rotation and tilt magnitudes in this initial trial structure are given in figure 5.22, and the exact values are given in in table A.110 in appendix A.1.

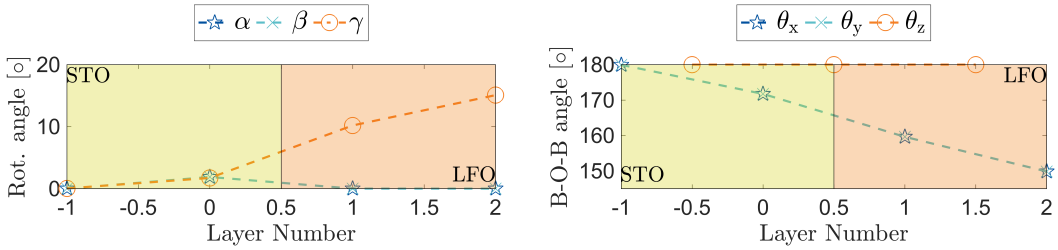

Figure 5.22: Rotation angles (left) and B-O-B tilt angles (right) in the initial trial structure for the (3,3) [001] oriented superlattice with LFO layers with an $a^0a^0c^-$ tilt pattern.

The initial trial structure in figure 5.22 converged in the strained relaxation calculations, and the rotation and tilt magnitudes in the resulting structure are given in figure 5.23. The exact values for the rotation and tilt magnitudes are given in table 5.11.

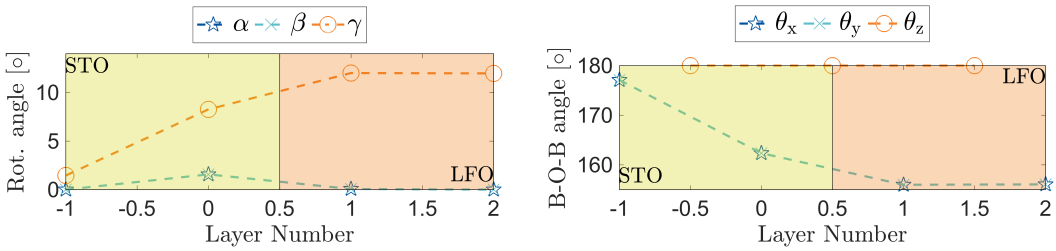

Figure 5.23: The resulting rotation angles (left) and B-O-B tilt angles (right) from the strained relaxation calculation of the initial trial structure for the (3,3) [001] oriented superlattice with LFO layers with an $a^0a^0c^-$ tilt pattern (figure 5.22).

Table 5.11: The resulting rotation angles (α, β, γ) and B-O-B tilt angles ($\theta_{x,y,z}$), in degrees, from the strained relaxation calculation of the initial trial structure for the (3,3) [001] oriented superlattice with LFO layers with an $a^0a^0c^-$ tilt pattern (figure 5.22).

Layer number	α	β	γ	θ_x	θ_y	θ_z
-1	0.0	0.0	1.5	177.1	177.1	-
-0.5	-	-	-	-	-	180.0
0	1.6	1.6	8.3	162.3	162.3	-
0.5	-	-	-	-	-	180.0
1	0.1	0.1	12.0	156.0	156.0	-
1.5	-	-	-	-	-	180.0
2	0.0	0.0	12.0	156.1	156.1	-

In figure 5.23 and table 5.11 one can see that the out-of-phase rotations about the out-of-plane axis (γ) reach a value of 12.0° in all layers in the LFO film. These rotations propagated into the STO film, and had a value of 1.5° in the middle layer in the STO film.

Structure with an $a^-a^-c^-$ tilt pattern in the LFO film layers

The last initial trial structure tested for the (3,3) [001] oriented superlattice was a structure with an $a^-a^-c^-$ tilt pattern in the LFO film layers. The rotation and tilt magnitudes in this initial trial structure is showed in figure 5.24, and the exact values are given in table A.111 in appendix A.1.

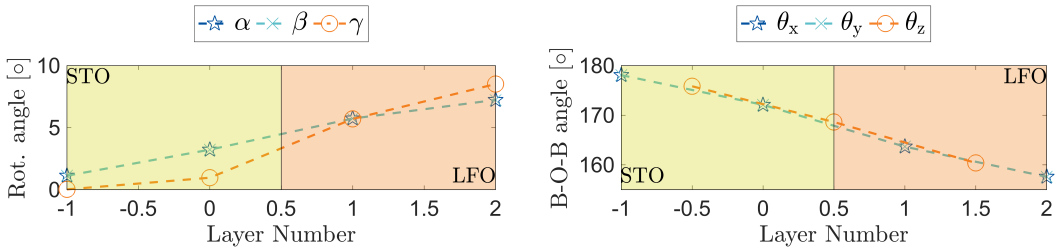

Figure 5.24: Rotation angles (left) and B-O-B tilt angles (right) in the initial trial structure for the (3,3) [001] oriented superlattice with LFO layers with an $a^-a^-c^-$ tilt pattern.

The initial trial structure with rotation and tilt magnitudes showed in figure 5.24 did not converge in the strained relaxation calculation. Hence, the $a^-a^-c^-$ tilt pattern in the (3,3) [001] oriented superlattice was assumed to not correspond to a stable state.

Possible stability of the relaxed structures

Two different relaxed structures for the (3,3) [001] oriented superlattice was found from the frozen-in phonon mode calculations. In the first structure, the LFO film layers had the $a^+b^-c^-$ tilt pattern, while the tilt pattern in the LFO film layers in the second found structure was $a^0a^0c^-$. The energies of these relaxed structures relative to the energy of the highly symmetric structure were **— 128 meV/f.u.** and **— 114 meV/f.u.**, respectively. Hence, of these two structures, the structure with LFO films with the $a^+b^-c^-$ tilt pattern was the most energetically favorable structure for the system, and might correspond to the ground state structure of the (3,3) [001] oriented superlattice.

Common for these two structures is that both structures had out-of-phase rotations about the out-of-plane axis. These rotations were the displacements corresponding to the phonon mode with the largest imaginary frequency for the (3,3) [001] oriented superlattice, that is, the $\text{Rot}^-_\perp$ phonon mode (figure 5.2). As the relaxed structure with the $a^+b^-c^-$ tilt pattern in the LFO film layers corresponded to the structure with lowest energy of these two structures, the numerous large imaginary phonon mode frequencies for the highly symmetric (3,3) [001] oriented superlattice seemed to imply that freezing in several of these imaginary frequency modes were favorable, rather than just the largest imaginary frequency mode (structure with the $a^0a^0c^-$ tilt pattern).

Assuming that the relaxed structure with the $a^+b^-c^-$ tilt pattern in the LFO film layers – obtained from five different initial trial structures – is the ground state structure of the system, this implies that the phonon mode calculations gave a strong indication of which kind of distortions that are present in the ground state structure.

5.2.2 The $(LFO_3/STO_3)_2$ [111] oriented superlattice

For the $(3,3)_2$ [111] oriented superlattice, four different initial trial structures were tested for the frozen-in phonon mode calculations. These four structures corresponded to LFO film layers with tilt patterns $a^-a^-a^-$, $a^-b^-c^0$, $a^0b^-a^0$, and $a^-b^-c^+$. The results obtained from these structures will now be presented, followed by a comparison of the energies of the relaxed structures.

Structure with an $a^-a^-a^-$ tilt pattern in the LFO film layers

The rotation and tilt magnitudes in the initial trial structure with LFO films with an $a^-a^-a^-$ tilt pattern are showed in figure 5.25. For exact rotation and tilt magnitudes in this structure, see table A.212 in appendix A.2.

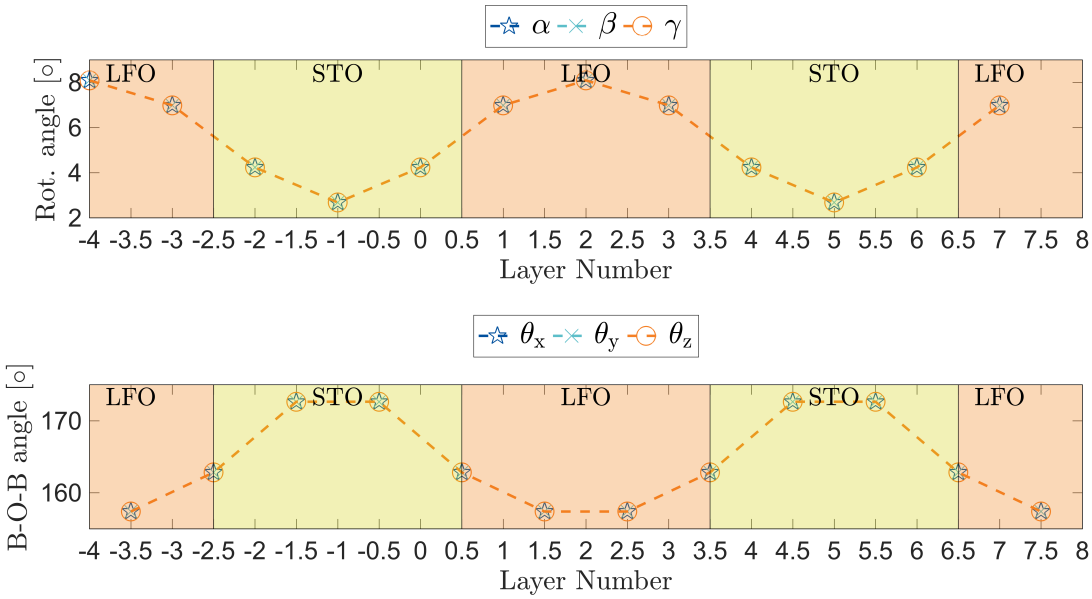

Figure 5.25: Rotation angles (top) and B-O-B tilt angles (bottom) in the initial trial structure for the $(3,3)_2$ [111] oriented superlattice with LFO layers with an $a^-a^-a^-$ tilt pattern.

The initial trial structure with rotations and tilts as showed in figure 5.25 relaxed to a structure with rotation and tilt magnitudes as shown in figure 5.26. The exact values of these rotation and tilt magnitudes are given in table 5.12. This structure also had an $a^-a^-a^-$ tilt pattern in the LFO film layers.

The relaxed structure also had an $a^-a^-a^-$ tilt pattern in the STO film layers, with a rotation magnitudes of 4.5° in the middle STO layer (table 5.12). As an $a^-a^-a^-$ tilt pattern is found in neither of the bulk structures of LFO nor STO, this result implied that by growing superlattices of LFO and STO with the [111]

orientation, one can obtain tilt patterns in the film layers not found in the bulk materials.

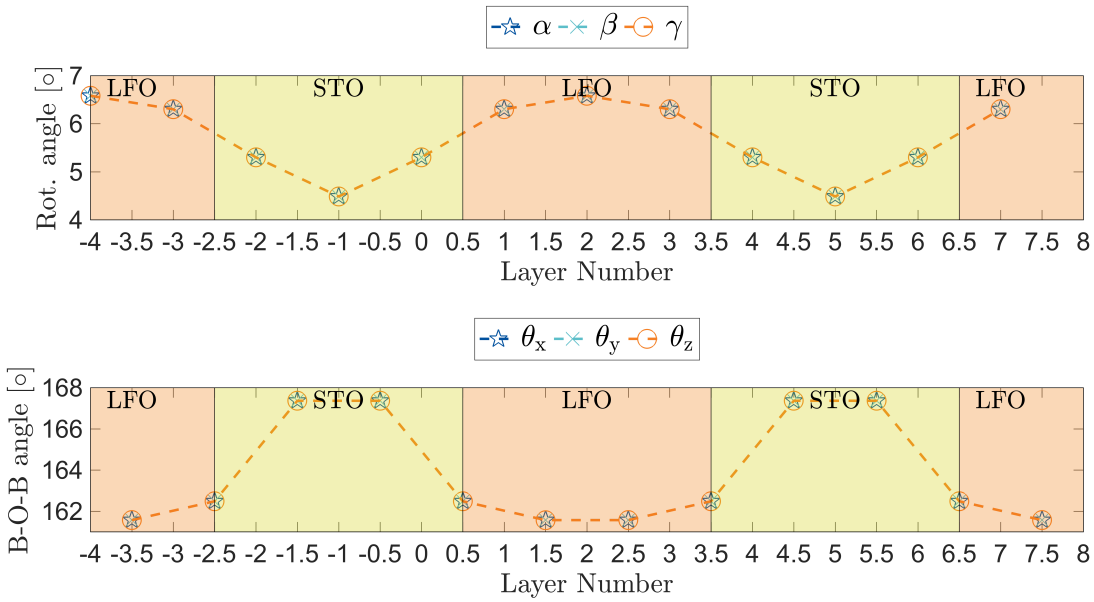

Figure 5.26: The resulting rotation angles (top) and B-O-B tilt angles (bottom) from the strained relaxation calculation of the initial trial structure for the $(3,3)_2$ [111] oriented superlattice with LFO layers with an $a^-a^-a^-$ tilt pattern (figure 5.25).

Table 5.12: The resulting rotation angles (α, β, γ) and B-O-B tilt angles ($\theta_{x,y,z}$), in degrees, from the strained relaxation calculation of the initial trial structure for the $(3,3)_2$ [111] oriented superlattice with LFO layers with an $a^-a^-a^-$ tilt pattern (figure 5.25).

Layer number	α	β	γ	θ_x	θ_y	θ_z
-4	6.6	6.6	6.6	-	-	-
-3.5	-	-	-	161.6	161.6	161.6
-3	6.3	6.3	6.3	-	-	-
-2.5	-	-	-	162.5	162.5	162.5
-2	5.3	5.3	5.3	-	-	-
-1.5	-	-	-	167.4	167.4	167.4
-1	4.5	4.5	4.5	-	-	-
-0.5	-	-	-	167.4	167.4	167.4
0	5.3	5.3	5.3	-	-	-
0.5	-	-	-	162.5	162.5	162.5
1	6.3	6.3	6.3	-	-	-
1.5	-	-	-	161.6	161.6	161.6
2	6.6	6.6	6.6	-	-	-
2.5	-	-	-	161.6	161.6	161.6
3	6.3	6.3	6.3	-	-	-
3.5	-	-	-	162.5	162.5	162.5
4	5.3	5.3	5.3	-	-	-
4.5	-	-	-	167.4	167.4	167.4
5	4.5	4.5	4.5	-	-	-
5.5	-	-	-	167.4	167.4	167.4
6	5.3	5.3	5.3	-	-	-
6.5	-	-	-	162.5	162.5	162.5
7	6.3	6.3	6.3	-	-	-
7.5	-	-	-	161.6	161.6	161.6

Structures with an $a^-b^-c^0$, $a^0b^-a^0$, and $a^-b^-c^+$ tilt pattern in the LFO film layers

None of the initial trial structures with LFO film layers with tilt patterns $a^-b^-c^0$, $a^0b^-a^0$, nor $a^-b^-c^+$ converged in the strained relaxation calculations. The rotation and tilt magnitudes for these initial trial structures are showed in figures 5.27-5.29, respectively. For exact values, see tables A.213-A.215, respectively, in appendix A.2.

That none of these initial trial structures converged implied that such structures were not energetically favorable in $(3,3)_2$ [111] oriented superlattices of LFO and STO. This result differed from the (3,3) [001] oriented structure, where a structure with an $a^+b^-c^-$ tilt pattern in the LFO film layers were found to be stable. As rotations about the different pseudocubic rotation axes were symmetry equivalent in the [111] oriented structures, the structure with the $a^-b^-c^+$ tilt pattern in the LFO layers should also have converged if the results were to coincide with the results for the [001] oriented (3,3) superlattice. A possible explanation for these results is that different orientations might affect the structure to be stable for different tilt patterns. This would also explain why the structure with an $a^-a^-a^-$ tilt pattern was found to be stable for the [111] oriented superlattice, while the initial structure with this tilt pattern in the [001] oriented superlattice did not converge. The reason why structures with different tilt patters are stable for different system orientations might be due to steric effects, as the stacking sequence differs for various system orientations.

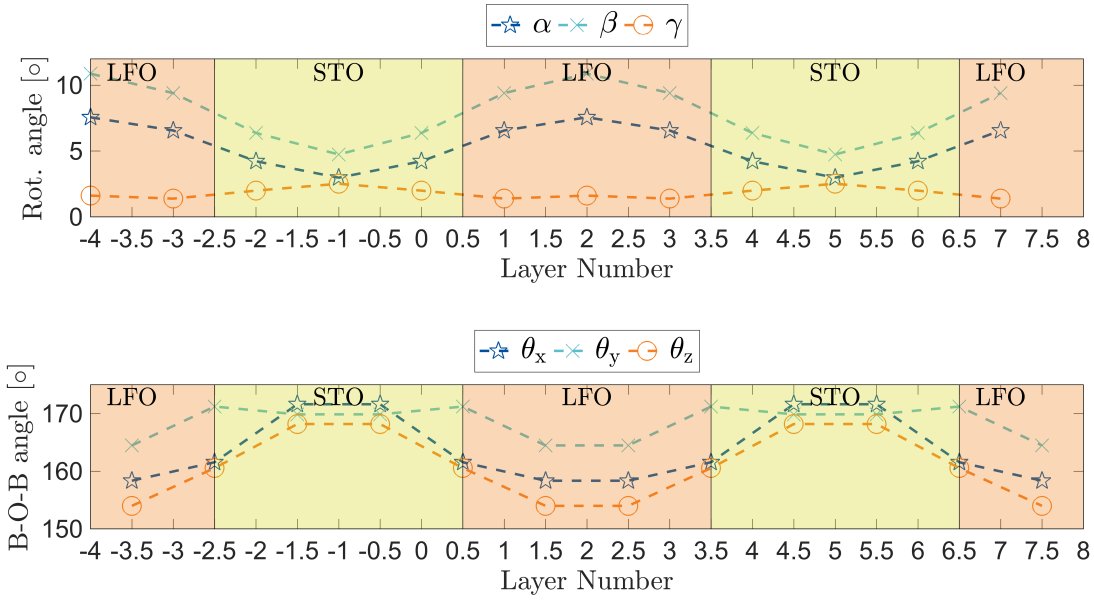

Figure 5.27: Rotation angles (top) and B-O-B tilt angles (bottom) in the initial trial structure for the $(3,3)_2$ [111] oriented superlattice with LFO layers with an $a^-b^-c^0$ tilt pattern.

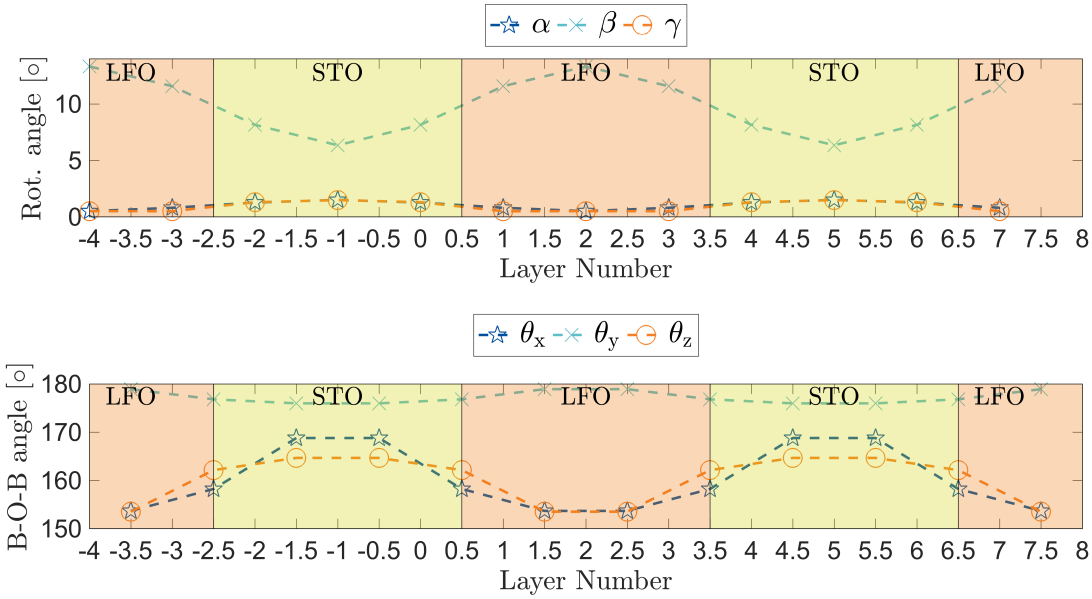

Figure 5.28: Rotation angles (top) and B-O-B tilt angles (bottom) in the initial trial structure for the $(3,3)_2$ [111] oriented superlattice with LFO layers with an $a^0b^-a^0$ tilt pattern.

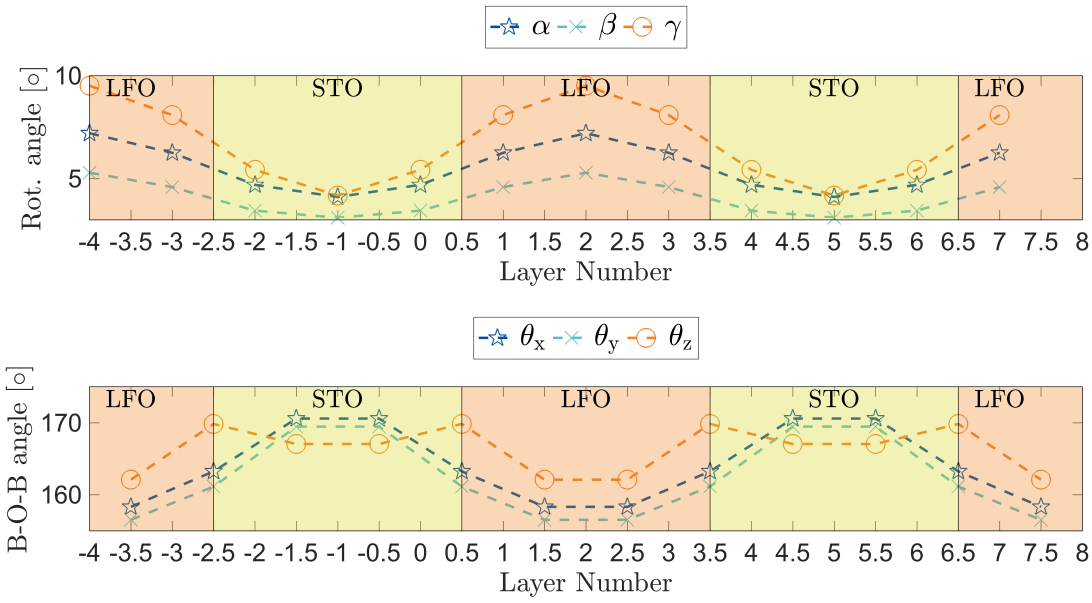

Figure 5.29: Rotation angles (top) and B-O-B tilt angles (bottom) in the initial trial structure for the $(3,3)_2$ [111] oriented superlattice with LFO layers with an $a^-b^-c^+$ tilt pattern.

Another explanation for that the the structure with the $a^-b^-c^+$ tilt pattern in the

LFO layers did not converge might be that the initial rotation magnitudes were too fare off from a possible stable structure with this tilt pattern. Looking at the rotation magnitudes in the relaxed [001] oriented structure, with the $a^+b^-c^-$ tilt pattern in the LFO film layers, in figure 5.19, one can see that the rotation magnitude for the in-phase rotations (α) were smaller than both out-of-phase rotation magnitudes in the LFO film layers. In the initial trial structure for the $(3,3)_2$ [111] oriented superlattice with an $a^-b^-c^+$ tilt pattern in the LFO layers, however, the rotation magnitudes for the in-phase rotations (γ) were larger than both out-of-phase rotation magnitudes in the LFO film layers. An initial trial structure with the $a^-b^-c^+$ tilt pattern in the LFO layers could therefore possibly converge if the rotation magnitudes for the in-phase and out-of-phase rotations were to be distributed more equal to the result from the (3,3) [001] oriented superlattice (figure 5.19).

Possible stability of the relaxed structure

As only one initial trial structure tested for the $(3,3)_2$ [111] oriented superlattice in this master thesis converged to a stable structure, only one candidate for the ground state structure was found. This was the structure with the $a^-a^-a^-$ tilt pattern in both the LFO and STO film layers. The energy of this relaxed structure, relative to that of the highly symmetric structure, was **— 114 meV/f.u.**.

5.2.3 Main findings from the frozen-in phonon mode calculations

For both the (3,3) [001] oriented and the $(3,3)_2$ [111] oriented superlattices, all initial trial structures that were able to converge to stable structures were structures where the phonon mode corresponding to the largest imaginary frequency mode, for the highly symmetric superlattices, had been frozen in. This result implies that the phonon mode calculations gives a strong indication of what kinds of displacements that are favorable for the structures.

Different for the two superlattices was that the ground state candidate structures found for the [001] and [111] oriented superlattices had different tilt patterns in the LFO film layers. The [001] oriented relaxed structure had an $a^+b^-c^-$ tilt pattern in the LFO film layers, while a structure with an $a^-a^-a^-$ tilt pattern was found to be stable for the [111] oriented relaxed structure. Hence, these findings indicate that the tilt pattern in the film layers can be controlled with system orientation.

5.3 Rotations and tilts in LFO/STO superlattices from structure calculations

In order to validate the the results obtain from the phonon mode calculations, structure calculations were also performed in this master thesis.

This section is divided into two parts. In the first part (section 5.3.1) the rotation and tilt magnitudes in the resulting relaxed [001] oriented structures are presented. The second part (section 5.3.2) covers the results obtained from the [111] oriented superlattices.

For each relaxed superlattice, the rotation and tilt magnitudes will be illustrated in rotation and tilt plots, respectively. In addition, the exact values of these rotation and tilt magnitudes will be presented in tables. For some superlattices there were octahedra in the same layers with different rotation and tilt magnitudes. In the plots, the average value in each layer is given, while in the tables these differences in magnitudes are given by uncertainties together with the average value.

5.3.1 LFO_n/STO_3 [001] oriented superlattices

For the [001] oriented superlattices, calculations were performed on two different sets of superlattices. The superlattices in the first set corresponded to superlattices where the in-phase rotations in the LFO film layers lay about the out-of-plane rotation axis. Hence, the tilt pattern in the LFO film layers in these superlattices were $a^-a^-c^+$. In the second set, the in-phase rotations lay about the pseudocubic [010] in-plane rotations axis, and the tilt pattern in the LFO film layers were therefore $a^-b^+a^-$. The results from the first set of superlattices will be presented first, followed by the results obtained from the second set.

Structures with an $a^-a^-c^+$ tilt pattern in the LFO film layers

The rotation and tilt magnitudes in the relaxed (2,3) and (6,3) [001] oriented superlattices, with an $a^-a^-c^+$ tilt pattern in the LFO film layers, are given in the top and bottom plots in figure 5.30, and in tables 5.13 and 5.14, respectively. In figure 5.30 the rotation and tilt magnitudes found for the strained relaxed LFO supercell with an $a^-a^-c^+$ tilt pattern, are marked as α_b, β_b, and γ_b, for the rotation angles, and $\theta_{(\mathrm{x,y,z}),\mathrm{b}}$ for the tilt angles. The exact values for these rotation and tilt magnitudes are given in table 5.15.

From figure 5.30 one can see that in the LFO film layer in the (2,3) superlattice, neither of the rotation magnitudes relaxed to that found in the LFO supercell. The in-plane rotation magnitudes (α and β) increased with the same rate from the middle bulk layer in the STO film (layer number -1) till the interface LFO layer (layer number 1). This was as expected, as these in-plane rotations were both out-of-phase rotations. Even though the rotation magnitude for these rotations

increased for every layer away from the bulk STO layer, the rotation magnitude did not reach that found in the LFO supercell, indicating that thick STO film layers suppress such in-plane rotations in the first interface layer of the LFO film layer. The out-of-plane rotations (γ) also increased in magnitude for every layer away from the bulk STO layer. However, the out-of-plane rotation magnitudes were larger than the in-plane rotation magnitudes in all layers (apart from the bulk STO layer). This is the opposite of what was seen in the LFO supercell, where the magnitudes for the in-plane rotations were larger than that for the out-of-plane rotation. As a matter of fact, the out-of-plane rotation magnitude reach a value well above the value for the LFO supercell, indicating that such rotations are favorable in both the STO and LFO layers at the interface.

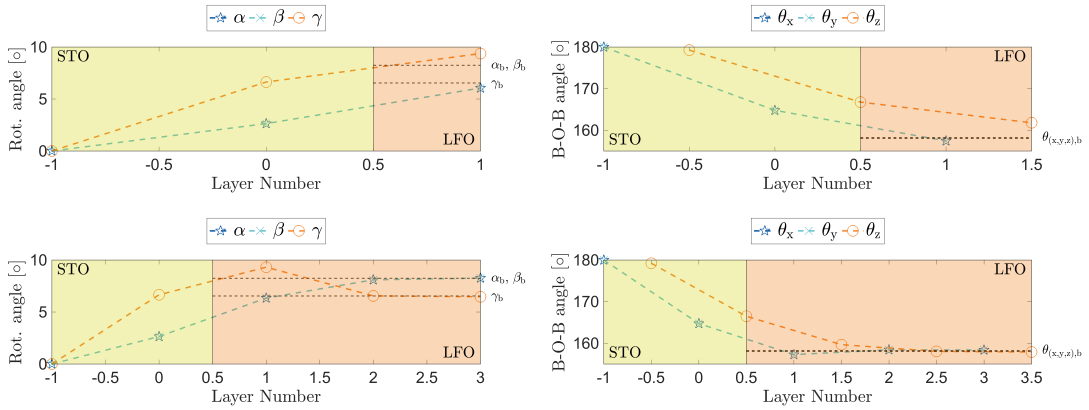

Figure 5.30: Rotation angles (left column) and B-O-B tilt angles (right column) for the superlattices with in-phase rotations about the out-of-plane direction in the LFO film layer. The top figures correspond to the (2,3) superlattice, while the bottom figures correspond to the (6,3) superlattice.

In the (6,3) superlattice the rotation magnitudes in the STO layers and the first LFO interface layer is approximately the same as that found in the (2,3) superlattice. In LFO layers further away from the interface, the in-plane rotation magnitudes continued to increase until they reach that of the LFO supercell approximately in layer number 2, while the out-of-plane rotation magnitudes started to decrease, and almost reached that of the LFO supercell in layer number 2 (table 5.14).

Table 5.13: The resulting rotation angles (α, β, γ) and B-O-B tilt angles ($\theta_{x,y,z}$), in degrees, from the ionic relaxation calculation of the (2,3) superlattice with an $a^-a^-c^+$ tilt pattern in the LFO film layer.

Layer number	α	β	γ	θ_x	θ_y	θ_z
-1	0.0	0.0	0.0	180.0	180.0	-
-0.5	-	-	-	-	-	179.3
0	2.6 ± 0.3	2.6 ± 0.3	6.6	164.8±1.0	164.8±1.0	-
0.5	-	-	-	-	-	166.8
1	6.1 ± 0.2	6.1 ± 0.2	9.4	157.4±1.1	157.4±1.1	-
1.5	-	-	-	-	-	161.8

Table 5.14: The resulting rotation angles (α, β, γ) and B-O-B tilt angles ($\theta_{x,y,z}$), in degrees, from the ionic relaxation calculation of the (6,3) superlattice with an $a^-a^-c^+$ tilt pattern in the LFO film layer.

Layer number	α	β	γ	θ_x	θ_y	θ_z
-1	0.0	0.0	0.0	180.0	180.0	-
-0.5	-	-	-	-	-	179.2
0	2.6 ± 0.3	2.6 ± 0.3	6.7	164.7±1.0	164.7±1.0	-
0.5	-	-	-	-	-	166.5
1	6.3 ± 0.3	6.3 ± 0.3	9.3	157.3±1.3	157.3±1.3	-
1.5	-	-	-	-	-	159.7
2	8.1 ± 0.6	8.1 ± 0.6	6.6	158.4±0.3	158.4±0.3	-
2.5	-	-	-	-	-	158.0
3	8.3 ± 0.6	8.3 ± 0.6	6.5	158.4	158.4	-
3.5	-	-	-	-	-	157.9

Table 5.15: The resulting rotation angles (α_{b}, β_{b}, γ_{b}) and B-O-B tilt angles ($\theta_{(\mathrm{x,y,z}),\mathrm{b}}$), in degrees, in the strained relaxed LFO supercell with an $a^-a^-c^+$ tilt pattern.

	Angle [°]
α_{b}	8.2
β_{b}	8.2
γ_{b}	6.5
$\theta_{\mathrm{x,b}}$	158.3
$\theta_{\mathrm{y,b}}$	158.3
$\theta_{\mathrm{z,b}}$	158.0

In table 5.16 the total energies (per functional unit) found for the (2,3) and (6,3) superlattices are given. As the energy found for the (2,3) superlattice was smaller than that found for the (6,3) superlattice, this suggests that such superlattices, with LFO film layers with the $a^-a^-c^+$ tilt pattern, are more stable for superlattices with thinner LFO film layers.

Table 5.16: The energies of the relaxed superlattices with an $a^-a^-c^+$ tilt pattern in the LFO film layer.

Superlattice	Energy [eV/f.u.]
(2,3)	-41.8806
(6,3)	-40.9988

Structures with an $\mathbf{a^-b^+a^-}$ tilt pattern in the LFO film layers

The rotation and tilt magnitudes in the relaxed (2,3) and (6,3) [001] oriented superlattices, with an $a^-b + c^-$ tilt pattern in the LFO film layer, are given in the top and bottom plots in figure 5.31 and in tables 5.17 and 5.18, respectively. In figure 5.31 the rotation and tilt magnitudes found for the strained relaxed LFO supercell with an $a^-b^+a^-$ tilt pattern, are marked as α_{b}, β_{b}, and γ_{b}, for the rotation angles, and $\theta_{(\mathrm{x,y,z}),\mathrm{b}}$ for the tilt angles. The exact values for these rotation and tilt magnitudes are given in table 5.19.

As for the [001] oriented superlattices with an $a^-a^-c^+$ tilt pattern in the LFO film layers (figure 5.30), in figure 5.31 one can see that all rotation magnitudes also increased from the bulk STO layer to the first LFO interface layer (layer number -1 and 1, respectively) in the superlattices with an $a^-b^+a^-$ tilt pattern in the LFO film layers. Another similarity in these layers between the superlattices with different rotational ordering in the LFO layers, was that the out-of-plane rotation magnitudes were the largest magnitudes in these layers. In the superlattices with

the $a^-b^+a^-$ tilt pattern in the LFO film layers this was as expected, however, as the out-of-plane rotation magnitude was the largest magnitude found in the LFO supercell (γ_b). Yet, this rotation magnitude also exceeded that of the LFO supercell in the first LFO interface layer.

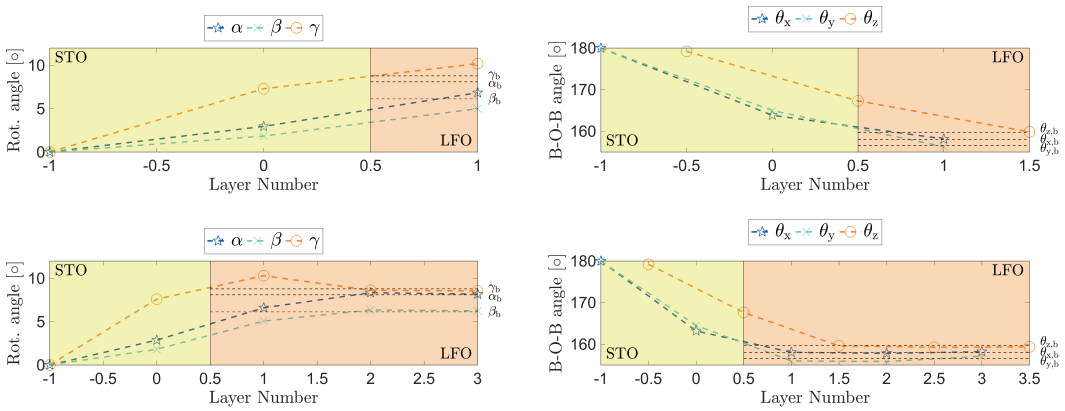

Figure 5.31: Rotation angles (left column) and B-O-B tilt angles (right column) for the superlattices with in-phase rotations about the pseudocubic [010] in-plane direction in the LFO film layer. The top figures correspond to the (2,3) superlattice, while the bottom figures correspond to the (6,3) superlattice.

Table 5.17: The resulting rotation angles (α, β, γ) and B-O-B tilt angles ($\theta_{x,y,z}$), in degrees, from the ionic relaxation calculation of the (2,3) superlattice with an $a^-b^+a^-$ tilt pattern in the LFO film layer.

Layer number	α	β	γ	θ_x	θ_y	θ_z
-1	0.0	0.0	0.0	180.0	180.0	-
-0.5	-	-	-	-	-	179.2±0.5
0	3.0	1.8 ± 0.1	7.3 ± 0.1	163.8	165.0±1.0	-
0.5	-	-	-	-	-	167.3±0.9
1	6.8 ± 0.6	5.0	10.2 ± 0.4	158.1	156.3±0.7	-
1.5	-	-	-	-	-	159.8

Table 5.18: The resulting rotation angles (α, β, γ) and B-O-B tilt angles ($\theta_{x,y,z}$), in degrees, from the ionic relaxation calculation of the (6,3) superlattice with an $a^-b^+a^-$ tilt pattern in the LFO film layer.

Layer number	α	β	γ	θ_x	θ_y	θ_z
-1	0.0	0.0	0.0	180.0	180.0	-
-0.5	-	-	-	-	-	179.2±0.5
0	2.9 ± 0.1	1.8 ± 0.1	7.6 ± 0.1	163.2	164.5±0.9	-
0.5	-	-	-	-	-	167.6±0.9
1	6.6 ± 0.5	5.1 ± 0.2	10.3 ± 0.5	158.1	156.0±0.9	-
1.5	-	-	-	-	-	159.6±0.9
2	8.3 ± 0.8	6.4 ± 0.1	8.6 ± 0.6	157.8	155.8±0.8	-
2.5	-	-	-	-	-	159.3±0.1
3	8.2 ± 0.7	6.3 ± 0.1	8.6 ± 0.7	158.2	157.1±0.2	-
3.5	-	-	-	-	-	159.4

Table 5.19: The resulting rotation angles (α_b, β_b, γ_b) and B-O-B tilt angles ($\theta_{(x,y,z),b}$), in degrees, in the strained relaxed LFO supercell with an $a^-b^+a^-$ tilt pattern.

	Angle [°]
α_b	8.1
β_b	6.1
γ_b	8.8
$\theta_{x,b}$	158.0
$\theta_{y,b}$	156.6
$\theta_{z,b}$	159.7

As the in-plane rotations were out-of-phase about the pseudocubic [100] axis and in-phase about the pseudocubic [010] axis, these rotation magnitudes evolved differently and converged to different rotation magnitudes in the superlattices with the $a^-b^+a^-$ tilt pattern in the LFO film layers. The in-phase rotation magnitude (β) was the smallest rotation magnitude in all layers in both the (2,3) and (6,3) superlattice, indicating that in-phase rotations about an in-plane axis is

less favorable than out-of-phase rotations in such superlattices. Also, the out-of-phase rotation magnitudes converged to almost identical values in the middle LFO layers in the (6,3) superlattice, implying that equal rotation magnitudes for the out-of-phase rotations in the LFO film layers were favorable.

Table 5.20 shows the total energies, per functional unit, found for the (2,3) and (6,3) superlattices. Again, the energy for the smaller superlattice had a more negative energy than the larger superlattice. Hence, structures corresponding to the $a^-b^+a^-$ tilt pattern in the LFO film layers, were assumed to be more stable for superlattices with thinner LFO film layers.

Table 5.20: The energies of the relaxed superlattices with an $a^-b^+a^-$ tilt pattern in the LFO film layer.

Superlattice	Energy [eV/f.u.]
(2,3)	-41.8875
(6,3)	-41.0044

Comparing the energies given in table 5.16 with those given in table 5.20 one can see that there were energy differences of ~ 7 meV/f.u. for the (2,3) superlattices and ~ 6 meV/f.u. for the (6,3) superlattices, where the total energies were smaller for the superlattices with the $a^-b^+a^-$ tilt pattern in the LFO film layers, indicating that this rotational orientation was slightly more energetically favorable than the $a^-a^-c^+$ orientation.

5.3.2 LFO_n/STO_5 [111] oriented superlattices

For the [111] oriented superlattices only one rotational ordering of the octahedra in the LFO film layers were tested, as rotations about all three pseudocubic rotation axes were symmetry equivalent in the [111] oriented systems. This was the $a^-a^-c^+$ tilt pattern. Both (4,5) and (10,5) superlattices were used in ionic relaxation calculations, but only the (4,5) superlattice converged. That the (10,5) superlattice did not converge properly might indicate that this tilt pattern in the LFO film layers was not favorable for this superlattice. Another explanation is that the initial trial structure might have been to fare from a potentially structure corresponding to an energy minimum.

The rotation and tilt magnitudes in the relaxed (4,5) [111] oriented superlattice are shown in figure 5.32 and the values are given in table 5.21. In figure 5.32 the rotation and tilt magnitudes found for the strained relaxed [111] oriented LFO supercell with an $a^-a^-c^+$ tilt pattern, are marked as α_b, β_b, and γ_b, for the rotation angles, and $\theta_{(\mathrm{x,y,z}),\mathrm{b}}$ for the tilt angles. The exact values for these rotation and tilt magnitudes are given in table 5.22.

In figure 5.32 one can see that the rotation magnitudes increased for each layer away from the bulk STO layers (layer numbers -2 and -1). The magnitude

of the in-phase rotation magnitude (γ) were smallest in all layers, indicating that in-phase rotations are less favorable the out-of-phase rotations in such systems. The out-of-phase rotation magnitudes (α and β) increased with slightly different rates. This was not as expected, as these rotations should be symmetry equivalent. This difference might have been caused by the correct lattice symmetry not being recognized in the calculation procedure. In that case, this was due to inaccuracy in the ionic positions in the structure.

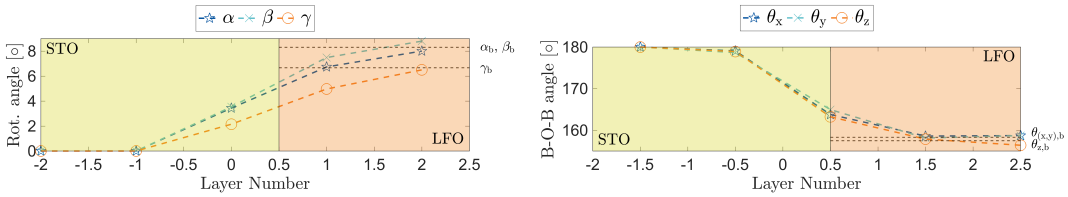

Figure 5.32: Rotation angles (left) and B-O-B tilt angles (right) for the (4,5) [111] oriented superlattice.

Table 5.21: The resulting rotation angles (α, β, γ) and B-O-B tilt angles ($\theta_{x,y,z}$), in degrees, from the ionic relaxation calculation of the (4,5) [111] oriented superlattice.

Layer number	α	β	γ	θ_x	θ_y	θ_z
-2	0.0	0.0	0.0	-	-	-
-1.5	-	-	-	180.0	180.0	180.0
-1	0.0	0.0	0.0	-	-	-
-0.5	-	-	-	179.1±0.5	178.7±0.3	178.9±0.1
0	3.4 ± 0.3	3.5 ± 0.3	2.1 ± 1.5	-	-	-
0.5	-	-	-	163.8±0.4	164.9±4.6	163.2±1.3
1	6.7 ± 0.3	7.5 ± 0.9	5.0 ± 2.2	-	-	-
1.5	-	-	-	158.6±2.7	158.1±0.4	157.9±0.6
2	8.0 ± 0.8	8.8 ± 0.6	6.5 ± 1.7	-	-	-
2.5	-	-	-	158.7±1.8	158.7±1.8	156.4

Comparing the rotation magnitudes in layer number 2 in figure 5.32 with those found for the LFO supercell (α_b, β_b, and γ_b), one can see that the rotation magnitudes almost reached the values corresponding to those far away from the interface

for this tilt pattern. This implies that thick STO film layers only suppress the rotation magnitudes in about two LFO interface layers.

Table 5.22: The resulting rotation angles (α_{b}, β_{b}, γ_{b}) and B-O-B tilt angles ($\theta_{(\mathrm{x,y,z}),\mathrm{b}}$), in degrees, in the strained relaxed [111] oriented LFO supercell with an $a^-a^-c^+$ tilt pattern.

	Angle [°]
α_{b}	8.3
β_{b}	8.3
γ_{b}	6.7
$\theta_{\mathrm{x,b}}$	158.3
$\theta_{\mathrm{y,b}}$	158.3
$\theta_{\mathrm{z,b}}$	157.5

In the [001] oriented superlattices the out-of-plane rotation magnitude (γ) exceeded that found for the LFO supercell in the first LFO interface layer, and were much larger in the first STO interface layer than that of the magnitudes of the in-plane rotations (α and β). This was observed for both rotational orientations in the LFO film layers (figures 5.30 and 5.31). In the [111] oriented superlattice, however, no such trend was observed. This result suggest that large out-of-plane rotation magnitudes – no matter if they are in-phase or out-of-phase, – are favored in the first interface layers on both sides of the interface in such [001] oriented systems. As out-of-plane rotations in [111] oriented systems correspond to rotations about all three pseudocubic rotation axes, no such favoring were observed for the [111] oriented superlattice in figure 5.32.

5.4 Correlation between results

By comparing the results obtained from the phonon mode calculations (section 5.1), frozen-in phonon mode calculations (section 5.2), and the structure calculations (section 5.3), it is possible to identify several similarities that strengthens the assumptions made from the individual results from these calculations.

Table 5.23 shows the penetration lengths (in number of functional units along the out-of-plane direction), found from the results from the different systems and calculation methods. The penetration lengths in the superlattices from the structure calculations were decided based on how many LFO interface layers containing rotation magnitudes that differed from that of the bulk LFO supercell (α_{b}, β_{b}, and γ_{b}). As the superlattices in the phonon mode and frozen-in phonon mode calculations modelled symmetric superlattices – where all film layers had a small

periodicity, m, – while the superlattices in the structure calculations modelled superlattices with thick STO film layers (as the ions in the middle STO layers were fixed to their bulk positions), the penetration length of the STO tilt pattern into the LFO film layer in these superlattices were expected to be shorter or equal to that of the symmetric superlattices. This was expected as the thicker film layers tend to be the most dominant in terms of deciding the overall structure in superlattices. In table 5.23 one can see that this was observed for the in-plane rotations in the [001] oriented superlattices. For these rotations, the penetration length was found to be more than 1.5 layers for the symmetric superlattices in the phonon mode and frozen-in phonon mode calculations, while for the superlattice with thick STO layers in the structure calculations, the penetration length was found to be approximately 1.5 layers.

Table 5.23: The penetration lengths (in number of functional units along the out-of-plane direction), found for in-plane and out-of-plane rotations (rot.) in the [001] and [111] oriented systems. The penetration length found from the results of the phonon mode calculations (PM calc.), frozen-in phonon mode calculations (FIPM calc.), and structure calculations (Struc. calc.) are shown.

	[001]			[111]		
	PM calc.	FIPM calc.	Struc. calc.	PM calc.	FIPM calc.	Struc. calc.
In-plane rot.	> 1.5	> 1.5	~ 1.5	> 1.5	> 1.5	> 1.5
Out-of-plane rot.	~ 1.5	~ 1.5	~ 1.5	> 1.5	> 1.5	> 1.5

For the [111] oriented systems, none of the superlattices had sufficiently thick film layers for the rotation magnitudes to reach values corresponding to rotations in a film far away from the interface. The predicted penetration lengths in the [111] oriented systems were longer (in number of functional units along the out-of-plane direction) than that of the [001] oriented systems, implying that the octahedral coupling effect is a steric effect.

Even though the penetration length of the out-of-plane rotations was found to be shorter than that for the in-plane rotations, both frozen-in phonon mode calculations and structure calculations for [001] oriented superlattices showed that the rotation magnitude for the out-of-plane rotation reached a maximum value in the first LFO interface layer (layer number 1), before it decreased in the second interface layer (layer number 2) (figures 5.17, 5.30, and 5.31). As this result was obtained from two independent calculation methods, the assumption that out-of-plane rotations in the first interface layer in LFO were highly favorable, was

strengthened.

Looking at the exact values for the rotation magnitudes in the first LFO interface layer (layer number 1) in the [001] oriented superlattices, from both the frozen-in phonon mode calculations – for structures with LFO film layers with an $a^+b^-c^-$ tilt pattern (table 5.8) – and the structure calculations – for structures with LFO film layers with an $a^-b^+a^-$ tilt pattern (tables 5.17 and 5.18), – one can see that the values only differ by about 1° for the resulting magnitudes from the different calculation methods. The rotation magnitudes for the in-plane and out-of-plane rotations in these layers are given in table 5.24.

Table 5.24: The in-plane and out-of-plane rotation magnitudes (in degrees) in the fist LFO interface layer (layer number 1) in the [001] oriented (3,3) superlattice with an $a^+b^-c^-$ tilt pattern in the LFO film layers (structure from frozen-in phonon mode calculation (FIPM calc.)) and the [001] oriented (2,3) superlattice with an $a^-b^+a^-$ tilt pattern in the LFO film layers (structure from structure calculation (struc. calc.)).

Calculation method	In-plane rotations		Out-of-plane rotations
	In-phase	Out-of-phase	Out-of-phase
(3,3) FIPM calc.	5.0	7.7 ± 0.6	9.4 ± 0.6
(2,3) struc. calc.	5.0	6.8 ± 0.6	10.2 ± 0.4

In table 5.24 one can see that the rotation magnitudes for the in-phase rotation was found to be exactly the same (5.0°) in the results from the frozen-in phonon mode calculation for the (3,3) superlattice (table 5.8) and the structure calculation for the (2,3) superlattice (tables 5.17). The magnitude for the out-of-phase rotations about the in-plane axis in this layer was found to be 0.9° higher in the structure obtained from the frozen-in phonon mode calculation than the structure obtained from the structure calculation. The magnitude of the out-of-phase rotations about the out-of-plane axis, however, was 0.8° higher in the structure obtained from the structure calculation than the structure obtained from the frozen-in phonon mode calculation. As the rotation magnitudes in the first LFO interface layer were found to be this similar for the structures obtained from the different calculation methods, the possibility that the structure in this interface layer corresponds to a stable interface structure was increased. In addition, these similar results in rotation magnitudes also implied that phonon mode calculations of highly symmetric superlattices can be used to investigate superlattice structures, at the same level as structure calculations.

Now over to the [001] oriented superlattices with in-phase rotations about the out-of-plane axis. In the structure calculations, superlattices with LFO film layers

with an $a^-a^-c^+$ tilt pattern converged (figure 5.30), while none of the initial trial structures having LFO film layers with an $a^-a^-c^+$ tilt pattern converged in the frozen-in phonon mode calculations. Comparing the exact values obtained for the rotation magnitudes in the (6,3) superlattice (with this LFO tilt pattern) in the structure calculations (table 5.14), with those of the initial trial structures (with this LFO tilt pattern) in the frozen-in phonon mode calculations (tables A.11-A.13 in appendix A.1), one can see a possible reason for why these initial trial structures did not converge. In all LFO layers – except for the first interface layer – in the (6,3) superlattice from the structure calculations, the out-of-plane rotation magnitudes were lower than the in-plane rotation magnitudes. At the STO interface layer, however, the out-of-plane rotation magnitude was larger than the in-plane rotation magnitudes. In all initial trial structures for systems with LFO film layers with the $a^-a^-c^+$ tilt pattern in the frozen-in phonon mode calculations, the opposite trend for the in-plane and out-of-plane rotation magnitudes were set. In the STO film layers, the out-of-plane rotation magnitude was lower than the in-plane rotation magnitudes, while in the LFO film layers, the out-of-plane rotation magnitude was higher than the in-plane rotation magnitudes. Hence, all three initial trial structures could have corresponded to structures too different from a stable structure, and thereby the calculations for these structures did not converge.

Finally, the correlation between the results for the [111] oriented systems will be covered. As seen in table 5.23, for the phonon mode calculations for the [111] oriented superlattices it was found that the penetration length for all kinds of rotation modes was longer than one and a half layers of [111] oriented BO_6 octahedra (figures 5.12-5.14). This finding was supported by the frozen-in-phonon mode calculations, where the relaxed (3,3) superlattice, with LFO film layers with the $a^-a^-a^-$ tilt pattern, showed to have rotation magnitudes of 4.5°in the middle STO film layer (table 5.12). These rotation magnitudes were considerably larger than the expected zero rotation magnitude in STO layers further away from the interface than the penetration length.

Looking at the suppression of rotation and tilt magnitudes in the first LFO interface layers in the resulting (4,5) [111] oriented superlattice structure for the structure calculations (figure 5.32), one can see that this suppression does not go much further into the LFO film layer than about one and a half layers. This implies that the penetration length of the STO tilt pattern into the LFO tilt pattern, in [111] oriented superlattices, is about one and a half layers.

In summery, the numerous similarities in the results obtained from the different calculation methods strengthened the validity of the results. In addition, these similarities insinuate that phonon mode calculations of highly symmetric superlattices can be utilized to study the structure in different superlattices.

Chapter 6

Conclusion

The results from this work show that phonon mode calculations of highly symmetric transition metal oxide perovskite superlattices are a promising rout for predicting the penetration length of the octahedral coupling associated with the proximity effect. For the [001] oriented superlattices, it was found that rotations about the out-of-plane axis had a shorter penetration length than rotations about the in-plane axes. This result was consistent with what was found for heterointerfaces of $La_{2/3}Sr_{1/3}MnO_3$ films and $SrTiO_3$ substrates in reference [38], as discussed in chapter 2. Precise predictions of the penetration length are important, as it is at this length scale the octahedral structure can be controlled by symmetry mismatch at this interface.

The phonon mode calculations also seemed to give good indications of what kind of distortions that were favorable for the superlattices. In the frozen-in phonon mode calculations, for both the (3,3) [001] oriented superlattice and the $(3,3)_2$ [111] oriented superlattice, the only initial trial structures that were able to converge to a relaxed stable structure, were those structures where the phonon mode corresponding to the largest imaginary frequency value had been frozen in. Hence, by performing phonon mode calculations, one can get an idea of what kind of distortions that are most probable for superlattices. In superlattices, these favorable distortions might be different from distortions found in the bulk film materials, as was seen for the $(3,3)_2$ [111] oriented superlattice, where distortions corresponding to the $a^-a^-a^-$ tilt pattern were found to generate a stable structure. When doing structure calculations, where the structure in both film materials must be set prior to the relaxation calculation, such novel structures might be hard to predict.

When it comes to control of the octahedral distortions by varying the film layer thicknesses and superlattice orientation, it was found that as the film layer thicknesses for the different film materials increased symmetrically ($m = n$), octahedral distortions corresponding to favorable rotations in the LFO film layers became more probable distortions for the superlattices. For the ultrathin (1,1) superlattices, however, the dominance of octahedral distortions favorable for the

LFO layers, was smaller. Hence, these results indicate that by varying the film layer thicknesses one can tune the rotation magnitudes in the different layers in the superlattices.

The results obtained from the frozen-in phonon mode calculations, performed for the (3,3) [001] oriented and $(3,3)_2$ [111] oriented superlattices, showed that the relaxed stable structures had different tilt patterns for the different superlattice orientations. For the (3,3) [001] oriented superlattice it was found that a structure with an $a^+b^-c^-$ tilt pattern in the LFO film layers was stable. For the $(3,3)_2$ [111] oriented superlattice, however, the relaxed stable structure was found to be a structure with an $a^-a^-a^-$ tilt pattern. This implied that the orientation could affect what kind of rotations most favorable in the film layers. Hence, it was found that the film layer thicknesses can tune the rotation magnitudes, while the orientation can affect the overall tilt pattern.

All in all, the results obtained from the calculations performed in this master thesis showed good agreement between the results obtained from the different calculation methods implemented – phonon mode calculations and structure calculations. Also, the results from the phonon mode calculations implied that the rotation magnitudes could be tuned with film layer thicknesses, while the frozen-in phonon mode calculations showed that a tilt pattern not present in neither of the bulk film materials might be stable for [111] oriented LFO_m/STO_n superlattices. With this one can conclude that it might be possible to control the octahedral structure in LFO_m/STO_n superlattices, by the means of film layer thicknesses and system orientation. As the Néel vector in LFO lies about the orthorhombic **a** axis, it might be possible to manipulate the direction of this axis – and hence tune the magnetic properties for the LFO film layers – by utilizing this control.

References

[1] Nobelprize.org. Nobel Media AB 2014. *The History of the Integrated Circuit*. 2003. URL: http://www.nobelprize.org/educational/physics/integrated_circuit/history/ (visited on 01/05/2018).

[2] C Chappert, A Fert, and Fn Van Dau. "The emergence of spin electronics in data storage". In: *Nature Materials* 6.11 (Nov. 2007), pp. 813–823.

[3] P. Wadley et al. "Electrical switching of an antiferromagnet". In: *Science* (2016).

[4] C Leighton et al. "Coupled structural/magnetocrystalline anisotropy transitions in the doped perovskite cobaltite Pr1-xSrxCoO3". In: 79 (June 2009).

[5] Chunhui Du et al. "Control of Magnetocrystalline Anisotropy by Epitaxial Strain in Double Perovskite Sr_2FeMoO_6 Films". In: *Phys. Rev. Lett.* 110 (14 Apr. 2013), p. 147204.

[6] X. Ke et al. "Structural control of magnetic anisotropy in a strain-driven multiferroic $EuTiO_3$ thin film". In: *Phys. Rev. B* 88 (9 Sept. 2013), p. 094434.

[7] Z Liao et al. "Controlled lateral anisotropy in correlated manganite heterostructures by interface-engineered oxygen octahedral coupling". In: *Nature Materials* 15.4 (Apr. 2016), pp. 425–+.

[8] D Kan et al. "Tuning magnetic anisotropy by interfacially engineering the oxygen coordination environment in a transition metal oxide". In: *Nature Materials* 15.4 (Apr. 2016), pp. 432–+.

[9] Eric Bousquet et al. "Improper ferroelectricity in perovskite oxide artificial superlattices". In: *Nature* 452.7188 (Apr. 2008), pp. 732–6.

[10] D. Treves. "Studies on Orthoferrites at the Weizmann Institute of Science". In: *Journal of Applied Physics* 36.3 (1965), pp. 1033–1039.

[11] *LaFeO3 Crystal Structure: Datasheet from "PAULING FILE Multinaries Edition – 2012" in SpringerMaterials*. Springer-Verlag Berlin Heidelberg Material Phases Data System (MPDS), Switzerland National Institute for Materials Science (NIMS), Japan. URL: http://materials.springer.com/isp/crystallographic/docs/sd_1214671.

[12] R. J. D. Tilley. *Perovskites : structure-property relationships*. eng. 2016.

[13] J. M. Rondinelli, S. J. May, and J. W. Freeland. "Control of octahedral connectivity in perovskite oxide heterostructures: An emerging route to multifunctional materials discovery". In: *MRS Bulletin* 37.3 (2012), pp. 261–270.

[14] K. Momma and F. Izumi. "VESTA 3 for three-dimensional visualization of crystal, volumetric and morphology data". In: *Journal of Applied Crystallography* 44 (2011), pp. 1272–1276.

[15] J. M. Rondinelli and N. A. Spaldin. "Structure and Properties of Functional Oxide Thin Films: Insights From Electronic-Structure Calculations". In: *Advanced Materials* 23.30 (2011), pp. 3363–3381.

[16] A. M. Glazer. "The classification of tilted octahedra in perovskites". In: *Acta Crystallographica Section B* 28.11 (Nov. 1972), pp. 3384–3392.

[17] A. M. Glazer. "Simple ways of determining perovskite structures". In: *Acta Crystallographica Section A* 31.6 (Nov. 1975), pp. 756–762.

[18] P. M. Woodward. "Octahedral Tilting in Perovskites. II. Structure Stabilizing Forces". In: *Acta Crystallographica Section B* 53.1 (Feb. 1997), pp. 44–66.

[19] I. I. Mazin et al. "Charge Ordering as Alternative to Jahn-Teller Distortion". In: *Phys. Rev. Lett.* 98 (17 Apr. 2007), p. 176406.

[20] "Origin of Ferroelectricity in Perovskite Oxides". In: *Nature* 358.6382 (July 1992), pp. 136–138.

[21] J B Goodenough. "Electronic and ionic transport properties and other physical aspects of perovskites". eng. In: 67.11 (Nov. 2004), pp. 1915–1993.

[22] Yoshinori Tokura. "Correlated-Electron Physics in Transition-Metal Oxides". In: *Physics Today* 56.7 (2003), pp. 50–55.

[23] Selma Erat et al. "Entanglement of charge transfer, hole doping, exchange interaction, and octahedron tilting angle and their influence on the conductivity of La1xSrxFe0.75Ni0.25O3: A combination of x-ray spectroscopy and diffraction". In: *Journal of Applied Physics* 108.12 (2010), p. 124906.

[24] A. T. Zayak et al. "Structural, electronic, and magnetic properties of $SrRuO_3$ under epitaxial strain". In: *Phys. Rev. B* 74 (9 Sept. 2006), p. 094104.

[25] A. T. Zayak et al. "Manipulating magnetic properties of $SrRuO_3$ and $CaRuO_3$ with epitaxial and uniaxial strains". In: *Phys. Rev. B* 77 (21 June 2008), p. 214410.

[26] S. J. May et al. "Quantifying octahedral rotations in strained perovskite oxide films". In: *Phys. Rev. B* 82 (1 July 2010), p. 014110.

[27] Alison J. Hatt and Nicola A. Spaldin. "Structural phases of strained $LaAlO_3$ driven by octahedral tilt instabilities". In: *Phys. Rev. B* 82 (19 Nov. 2010), p. 195402.

[28] K. J. Choi et al. “Enhancement of Ferroelectricity in Strained BaTiO3 Thin Films”. In: *Science* 306.5698 (2004), pp. 1005–1009.

[29] C.-J. Eklund, C. J. Fennie, and K. M. Rabe. “Strain-induced ferroelectricity in orthorhombic $CaTiO_3$ from first principles”. In: *Phys. Rev. B* 79 (22 June 2009), p. 220101.

[30] JW Seo et al. “Structural domains in antiferromagnetic LaFeO3 thin films”. In: *International Journal Of Materials Research* 97.7 (July 2006), pp. 943–947.

[31] Magnus Moreau et al. “First-principles study of the effect of (111) strain on octahedral rotations and structural phases of $LaAlO_3$”. In: *Phys. Rev. B* 95 (6 Feb. 2017), p. 064109.

[32] Magnus Moreau et al. “Strain-phonon coupling in (111)-oriented perovskite oxides”. In: *Phys. Rev. B* 96 (9 Sept. 2017), p. 094109.

[33] Jun He et al. “Control of Octahedral Tilts and Magnetic Properties of Perovskite Oxide Heterostructures by Substrate Symmetry”. In: *Phys. Rev. Lett.* 105 (22 Nov. 2010), p. 227203.

[34] James M. Rondinelli and Nicola A. Spaldin. “Substrate coherency driven octahedral rotations in perovskite oxide films”. In: *Phys. Rev. B* 82 (11 Sept. 2010), p. 113402.

[35] I. Hallsteinsen et al. “Concurrent magnetic and structural reconstructions at the interface of (111)-oriented $La_{0.7}Sr_{0.3}MnO_3/LaFeO_3$”. In: *Phys. Rev. B* 94 (20 Nov. 2016), p. 201115.

[36] A. Y. Borisevich et al. “Suppression of Octahedral Tilts and Associated Changes in Electronic Properties at Epitaxial Oxide Heterostructure Interfaces”. In: *Phys. Rev. Lett.* 105 (8 Aug. 2010), p. 087204.

[37] F.Y. Bruno et al. “Insight into spin transport in oxide heterostructures from interface-resolved magnetic mapping”. In: *Nature Communications* 6 (Feb. 2015).

[38] Magnus Moreau, Sverre M. Selbach, and Thomas Tybell. “Octahedral coupling in (111)- and (001)-oriented $La_{2/3}Sr_{1/3}MnO_3/SrTiO_3$ heterostructures”. In: (Oct. 2017).

[39] S. J. May et al. “Control of octahedral rotations in $(LaNiO_3)_n/(SrMnO_3)_m$ superlattices”. In: *Phys. Rev. B* 83 (15 Apr. 2011), p. 153411.

[40] G. Kresse, M. Marsman, and J. Furthmüller. *VASP the GUIDE*. 2016. URL: `https://cms.mpi.univie.ac.at/vasp/vasp/vasp.html` (visited on 06/11/2017).

[41] D. S. Sholl and J. A. Steckel. *Density functional theory : a practical introduction*. Hoboken, N.J: Wiley, 2009. ISBN: 9780470373170.

[42] A Togo and I Tanaka. "First principles phonon calculations in materials science". In: *Scr. Mater.* 108 (Nov. 2015), pp. 1–5.

[43] J. Luning et al. "Determination of the antiferromagnetic spin axis in epitaxial LaFeO-3 films by x-ray magnetic linear dichroism spectroscopy". In: *Phys. Rev.* B67 (2003), p. 214433.

[44] J.P. Perdew et al. "Restoring the Density-Gradient Expansion for Exchange in Solids and Surfaces". In: *Physical Review Letters* 100 (2008), p. 136406.

[45] P.E. Blöchl. "Projector augmented-wave method". In: *Physical Review B* 50 (1994), p. 17953.

[46] G. Kresse and J. Joubert. "From ultrasoft pseudopotentials to the projector augmented wave method". In: *Physical Review B* 59 (1999), p. 1758.

[47] S. L. Dudarev et al. "Electron-energy-loss spectra and the structural stability of nickel oxide: An LSDA+U study". In: *Phys. Rev. B* 57 (3 Jan. 1998), pp. 1505–1509.

[48] Harold T. Stokes and Dorian M. Hatch. "*FINDSYM*: program for identifying the space-group symmetry of a crystal". In: *Journal of Applied Crystallography* 38.1 (Feb. 2005), pp. 237–238.

[49] H. W. Jang et al. "Ferroelectricity in Strain-Free $SrTiO_3$ Thin Films". In: *Phys. Rev. Lett.* 104 (19 May 2010), p. 197601.

Appendix A

Exact values for the rotation and tilt magnitudes in the initial trial structures for the frozen-in phonon mode calculations

All rotation and tilt magnitudes found in the initial trial structures for the frozen-in phonon mode calculations are given in tables A.11-A.215, one table per structure. In several of the superlattice structures, there were octahedra in the same layer with different rotation and tilt magnitudes. The uncertainties in the rotation and tilt magnitudes given in these tables correspond to this difference in magnitude for octahedra in the same layer.

A.1 The LFO_3/STO_3 [001] oriented superlattice

Structures with the $a^-a^-c^+$ tilt pattern in the LFO film layers

Table A.11: The rotation and tilt magnitudes, in degrees, in the initial trial structure with the $a^-a^-c^+$ tilt pattern and close-to-evenly distribution of in-plane and out-of-plane rotations.

Layer number	α	β	γ	θ_x	θ_y	θ_z
-1	1.1	1.1	0.1	178.1	178.1	-
-0.5	-	-	-	-	-	175.8
0	3.2	3.2	1.7	171.4±4.6	171.4±4.6	-
0.5	-	-	-	-	-	168.6
1	5.7	5.7	5.8	163.5±0.1	163.5±0.1	-
1.5	-	-	-	-	-	160.4
2	7.2	7.2	8.1	158.2	158.2	-

Table A.12: The rotation and tilt magnitudes, in degrees, in the initial trial structure with the $a^-a^-c^+$ tilt pattern and smaller rotation magnitudes for in-plane rotations than for out-of-plane rotations.

Layer number	α	β	γ	θ_x	θ_y	θ_z
-1	0.9	0.9	0.1	178.5	178.5	-
-0.5	-	-	-	-	-	176.7
0	3.0	3.0	2.4	170.8±3.4	170.8±3.4	-
0.5	-	-	-	-	-	170.9
1	4.6	4.6	8.1	161.3	161.3	-
1.5	-	-	-	-	-	164.3
2	5.8	5.8	11.3	154.6	154.6	-

Table A.13: The rotation and tilt magnitudes, in degrees, in the initial trial structure with the $a^-a^-c^+$ tilt pattern and smaller rotation magnitudes for in-plane rotations than for out-of-plane rotations.

Layer number	α	β	γ	θ_x	θ_y	θ_z
-1	0.7	0.7	0.1	178.8	178.8	-
-0.5	-	-	-	-	-	177.5
0	2.7	2.7	2.7	170.5±2.5	170.5±2.5	-
0.5	-	-	-	-	-	173.2
1	3.4	3.4	9.3	160.2	160.2	-
1.5	-	-	-	-	-	168.2
2	4.4	4.4	12.9	152.9	152.9	-

Structures with the $a^+a^-c^-$ tilt pattern in the LFO film layers

Table A.14: The rotation and tilt magnitudes, in degrees, in the initial trial structure with the $a^+a^-c^-$ tilt pattern and close-to-evenly distribution of in-plane and out-of-plane rotations.

Layer number	α	β	γ	θ_x	θ_y	θ_z
-1	1.3	1.1 ± 0.3	0.0	178.1±0.5	177.7	-
-0.5	-	-	-	-	-	175.7±0.4
0	3.3	3.2 ± 0.3	1.0	171.3±5.2	177.1	-
0.5	-	-	-	-	-	168.6±1.2
1	5.6	5.7 ± 1.1	5.7	164.0±1.2	163.9	-
1.5	-	-	-	-	-	160.6±1.9
2	7.1	7.2 ± 1.4	8.5	157.5±1.9	157.6	-

Table A.15: The rotation and tilt magnitudes, in degrees, in the initial trial structure with the $a^+a^-c^-$ tilt pattern and smaller rotation magnitudes for in-plane rotations than for out-of-plane rotations.

Layer number	α	β	γ	θ_x	θ_y	θ_z
-1	1.0	0.9 ± 0.2	0.0	178.5±0.4	178.2	-
-0.5	-	-	-	-	-	176.5±0.4
0	3.0	3.0 ± 0.2	1.3	171.3±4.1	175.8	-
0.5	-	-	-	-	-	170.9±0.9
1	4.5	4.6 ± 0.9	8.0	162.0±1.0	161.8	-
1.5	-	-	-	-	-	164.4±1.6
2	5.7	5.8 ± 1.2	11.8	153.6±1.0	153.7	-

Table A.16: The rotation and tilt magnitudes, in degrees, in the initial trial structure with the $a^+a^-c^-$ tilt pattern and smaller rotation magnitudes for in-plane rotations than for out-of-plane rotations.

Layer number	α	β	γ	θ_x	θ_y	θ_z
-1	0.8	0.7 ± 0.2	0.0	178.9±0.3	178.6	-
-0.5	-	-	-	-	-	177.4±0.3
0	2.7	2.7 ± 0.2	1.5	171.4±3.0	174.7	-
0.5	-	-	-	-	-	173.2±0.7
1	3.4	3.4 ± 0.7	9.1	160.9±0.6	160.7	-
1.5	-	-	-	-	-	168.3±1.2
2	4.3	4.4 ± 0.9	13.5	151.7±0.5	151.7	-

Table A.17: The rotation and tilt magnitudes, in degrees, in the initial trial structure with the $a^+a^-c^-$ tilt pattern and close-to-evenly distribution of in-plane and out-of-plane rotations.

Layer number	α	β	γ	θ_x	θ_y	θ_z
-1	0.9	0.8 ± 0.2	0.0	178.7±0.3	178.4	-
-0.5	-	-	-	-	-	177.0±0.3
0	2.8	2.8 ± 0.2	0.7	171.7±3.7	175.9	-
0.5	-	-	-	-	-	172.0±0.8
1	3.9	4.0 ± 0.8	4.0	168.8±1.2	168.7	-
1.5	-	-	-	-	-	166.4±1.4
2	5.0	5.1 ± 1.0	6.0	164.1±1.4	164.2	-

Table A.18: The rotation and tilt magnitudes, in degrees, in the initial trial structure with the $a^+a^-c^-$ tilt pattern and close-to-evenly distribution of in-plane and out-of-plane rotations.

Layer number	α	β	γ	θ_x	θ_y	θ_z
-1	1.8	1.6 ± 0.4	0.0	177.3±0.7	176.8	-
-0.5	-	-	-	-	-	174.0±0.6
0	3.8	3.9 ± 0.6	1.3	170.6±7.0	177.5	-
0.5	-	-	-	-	-	164.1±1.6
1	7.8	8.0 ± 1.6	8.0	157.8±2.5	157.7	-
1.5	-	-	-	-	-	153.1±2.6
2	9.9	10.1 ± 2.0	11.8	148.9±2.6	149.0	-

Structures with the $a^+b^-c^-$ tilt pattern in the LFO film layers

Table A.19: The rotation and tilt magnitudes, in degrees, in the initial trial structure with the $a^+b^-c^-$ tilt pattern.

Layer number	α	β	γ	θ_x	θ_y	θ_z
-1	0.8	1.3 ± 0.2	0.0	177.7±0.3	178.6	-
-0.5	-	-	-	-	-	176.0±0.3
0	2.7	3.5 ± 0.2	1.2	171.4±6.0	175.1	-
0.5	-	-	-	-	-	169.2±0.9
1	3.4	6.9 ± 0.7	6.8	160.7±1.1	164.8	-
1.5	-	-	-	-	-	161.5±1.5
2	4.3	8.7 ± 0.9	10.2	153.2±1.1	157.8	-

Structures with the $a^0a^0c^-$ tilt pattern in the LFO film layers

Table A.110: The rotation and tilt magnitudes, in degrees, in the initial trial structure with the $a^0a^0c^-$ tilt pattern.

Layer number	α	β	γ	θ_x	θ_y	θ_z
-1	0.0	0.0	0.0	179.9	179.9	-
-0.5	-	-	-	-	-	180.0
0	1.9	1.9	1.7	171.7	171.7	-
0.5	-	-	-	-	-	180.0
1	0.0	0.0	10.2	159.6	159.6	-
1.5	-	-	-	-	-	180.0
2	0.0	0.0	15.1	149.8	149.8	-

Structures with the $a^-a^-c^-$ tilt pattern in the LFO film layers

Table A.111: The rotation and tilt magnitudes, in degrees, in the initial trial structure with the $a^-a^-c^-$ tilt pattern.

Layer number	α	β	γ	θ_x	θ_y	θ_z
-1	1.1	1.1	0.0	178.1	178.1	-
-0.5	-	-	-	-	-	175.8
0	3.2	3.2	1.0	172.1±5.0	172.1±5.0	-
0.5	-	-	-	-	-	168.6
1	5.7	5.7	5.7	163.7±0.1	163.7±0.1	-
1.5	-	-	-	-	-	160.4
2	7.2	7.2	8.5	157.6	157.6	-

A.2 The LFO_3/STO_3 [111] oriented superlattice

Structures with the $a^-a^-a^-$ tilt pattern in the LFO film layers

Table A.212: The rotation and tilt magnitudes, in degrees, in the initial trial structure with the $a^-a^-a^-$ tilt pattern.

Layer number	α	β	γ	θ_x	θ_y	θ_z
-4	8.1	8.1	8.1	-	-	-
-3.5	-	-	-	157.4	157.4	157.4
-3	7.0	7.0	7.0	-	-	-
-2.5	-	-	-	162.8	162.8	162.8
-2	4.2	4.2	4.2	-	-	-
-1.5	-	-	-	172.6	172.6	172.6
-1	2.7	2.7	2.7	-	-	-
-0.5	-	-	-	172.6	172.6	172.6
0	4.2	4.2	4.2	-	-	-
0.5	-	-	-	162.8	162.8	162.8
1	7.0	7.0	7.0	-	-	-
1.5	-	-	-	157.4	157.4	157.4
2	8.1	8.1	8.1	-	-	-
2.5	-	-	-	157.4	157.4	157.4
3	7.0	7.0	7.0	-	-	-
3.5	-	-	-	162.8	162.8	162.8
4	4.2	4.2	4.2	-	-	-
4.5	-	-	-	172.6	172.6	172.6
5	2.7	2.7	2.7	-	-	-
5.5	-	-	-	172.6	172.6	172.6
6	4.2	4.2	4.2	-	-	-
6.5	-	-	-	162.8	162.8	162.8
7	7.0	7.0	7.0	-	-	-
7.5	-	-	-	157.4	157.4	157.4

Structures with the $a^-b^-c^0$ tilt pattern in the LFO film layers

Table A.213: The rotation and tilt magnitudes, in degrees, in the initial trial structure with the $a^-b^-c^0$ tilt pattern.

Layer number	α	β	γ	θ_x	θ_y	θ_z
-4	7.6	10.9	1.6	-	-	-
-3.5	-	-	-	158.3	164.5	154.0
-3	6.6	9.4	1.4	-	-	-
-2.5	-	-	-	161.6	171.2	160.5
-2	4.2	6.4	2.0	-	-	-
-1.5	-	-	-	171.6	169.9	168.2
-1	3.0	4.7	2.5	-	-	-
-0.5	-	-	-	171.6	169.9	168.2
0	4.2	6.4	2.0	-	-	-
0.5	-	-	-	161.6	171.2	160.5
1	6.6	9.4	1.4	-	-	-
1.5	-	-	-	158.3	164.5	154.0
2	7.6	10.9	1.6	-	-	-
2.5	-	-	-	158.3	164.5	154.0
3	6.6	9.4	1.4	-	-	-
3.5	-	-	-	161.6	171.2	160.5
4	4.2	6.4	2.0	-	-	-
4.5	-	-	-	171.6	169.9	168.2
5	3.0	4.7	2.5	-	-	-
5.5	-	-	-	171.6	169.9	168.2
6	4.2	6.4	2.0	-	-	-
6.5	-	-	-	161.6	171.2	160.5
7	6.6	9.4	1.4	-	-	-
7.5	-	-	-	158.3	164.5	154.0

Structures with the $a^0b^-a^0$ tilt pattern in the LFO film layers

Table A.214: The rotation and tilt magnitudes, in degrees, in the initial trial structure with the $a^0b^-a^0$ tilt pattern.

Layer number	α	β	γ	θ_x	θ_y	θ_z
-4	0.5	13.3	0.5	-	-	-
-3.5	-	-	-	153.7	178.9	153.5
-3	0.8	11.6	0.5	-	-	-
-2.5	-	-	-	158.2	176.8	162.1
-2	1.3	8.2	1.3	-	-	-
-1.5	-	-	-	168.8	176.0	164.7
-1	1.5	6.3	1.5	-	-	-
-0.5	-	-	-	168.8	176.0	164.7
0	1.3	8.2	1.3	-	-	-
0.5	-	-	-	158.2	176.8	162.1
1	0.8	11.6	0.5	-	-	-
1.5	-	-	-	153.7	178.9	153.5
2	0.5	13.3	0.5	-	-	-
2.5	-	-	-	153.7	178.9	153.5
3	0.8	11.6	0.5	-	-	-
3.5	-	-	-	158.2	176.8	162.1
4	1.3	8.2	1.3	-	-	-
4.5	-	-	-	168.8	176.0	164.7
5	1.5	6.3	1.5	-	-	-
5.5	-	-	-	168.8	176.0	164.7
6	1.3	8.2	1.3	-	-	-
6.5	-	-	-	158.2	176.8	162.1
7	0.8	11.6	0.5	-	-	-
7.5	-	-	-	153.7	178.9	153.5

Structures with the $a^-b^-c^+$ tilt pattern in the LFO film layers

Table A.215: The rotation and tilt magnitudes, in degrees, in the initial trial structure with the $a^-b^-c^+$ tilt pattern.

Layer number	α	β	γ	θ_x	θ_y	θ_z
-4	7.2 ± 0.9	5.3 ± 1.3	9.5 ± 2.0	-	-	-
-3.5	-	-	-	158.3±3.5	156.5±4.2	162.1±1.8
-3	6.3 ± 0.3	4.6 ± 0.6	8.1 ± 1.7	-	-	-
-2.5	-	-	-	163.3±2.1	161.1±2.8	169.8±1.2
-2	4.7 ± 0.6	3.4 ± 0.8	5.4 ± 1.3	-	-	-
-1.5	-	-	-	170.6±4.0	169.5±0.5	167.1±0.6
-1	4.1 ± 0.2	3.1 ± 0.4	4.2 ± 1.0	-	-	-
-0.5	-	-	-	170.6±4.0	169.5±0.5	167.1±0.6
0	4.7 ± 0.6	3.4 ± 0.8	5.4 ± 1.3	-	-	-
0.5	-	-	-	163.3±2.1	161.1±2.8	169.8±1.2
1	6.3 ± 0.3	4.6 ± 0.6	8.1 ± 1.7	-	-	-
1.5	-	-	-	158.3±3.5	156.5±4.2	162.1±1.8
2	7.2 ± 0.9	5.3 ± 1.3	9.5 ± 2.0	-	-	-
2.5	-	-	-	158.3±3.5	156.5±4.2	162.1±1.8
3	6.3 ± 0.3	4.6 ± 0.6	8.1 ± 1.7	-	-	-
3.5	-	-	-	163.3±2.1	161.1±2.8	169.8±1.2
4	4.7 ± 0.6	3.4 ± 0.8	5.4 ± 1.3	-	-	-
4.5	-	-	-	170.6±4.0	169.5±0.5	167.1±0.6
5	4.1 ± 0.2	3.1 ± 0.4	4.2 ± 1.0	-	-	-
5.5	-	-	-	170.6±4.0	169.5±0.5	167.1±0.6
6	4.7 ± 0.6	3.4 ± 0.8	5.4 ± 1.3	-	-	-
6.5	-	-	-	163.3±2.1	161.1±2.8	169.8±1.2
7	6.3 ± 0.3	4.6 ± 0.6	8.1 ± 1.7	-	-	-
7.5	-	-	-	158.3±3.5	156.5±4.2	162.1±1.8